The Formation and Evolution of Neutron Stars: Astrometry, Timing, and Transients

Thesis by

P. Brian Cameron

In Partial Fulfillment of the Requirements

for the Degree of

Doctor of Philosophy

California Institute of Technology

Pasadena, California

2009

(Defended June 2, 2008)

Acknowledgements

I have been incredibly fortunate these last five years to work with and have the support of so many amazing people. Foremost, I would like to acknowledge my enormous debt to my advisor, Shri Kulkarni. His vision and tireless dedication to astronomy were inspiring, and led to the topics in this thesis being at the forefront of astrophysics. Our styles contrasted, but his energy, open advice, and support made for a very rewarding collaboration. In this same vein, I am grateful to Matthew Britton whose ideas and open door made the last 2 years incredibly enjoyable.

I have also had the privilege of working with a number talented people on a wide variety of topics. I am grateful to Bryan Jacoby, David Kaplan, Bob Rutledge, and Dale Frail for their insights and patience. I would also like to thank the NGAO crowd that got me thinking hard about astrometry: Rich Dekany, Claire Max, Jessica Lu, and Andrea Ghez. No observer could ever function with out people working tirelessly at the telescope and when you return from it. I am grateful for the patience and dedication of the Keck astronomers, especially Al Conrad, Randy Campbell and Jim Lyke, as well as those at Palomar: Jean Mueller, and Karl Dunscombe. I am indebted to the excellent staff here at Caltech for putting up with my endless questions and requests: Patrick Shopbell, Anu Mahabal, and Cheryl Southard.

My classmates and fellow graduate students have made Caltech the most intellectually stimulating time of my life, especially Larry Weintraub, Dan Stark, Stuartt Corder, Mansi Kasilwal, Francis O'Donovan, Cathy Slesnick, Milan Bogosavljevic and my officemates Alicia Soderberg, Joanna Brown, and Matthew Stevenson. In particular, I would like to thank my perpetual sounding board and officemate, Adam Kraus, who was always willing to hear my latest rant or (more often) solve my latest

technical problem.

Most importantly I would like to thank my family. My mother, for her endless love and support through this whole journey, and my father for his timely advice and insights. None of this would have been possible without my amazing wife, Danielle, whose caring, loving support knows no bounds — thank you for taking this journey with me.

Abstract

In order to address open questions regarding the death of massive stars and the evolution of the stellar fossils left behind, we use techniques spanning the electromagnetic spectrum to study the youngest and oldest neutron stars. We begin by exploring and developing a new technique — ground-based astrometry with adaptive optics. This technology is relatively new to astronomy, and has incredible potential for tracking the motions of stars. We enumerate experimental design consideration for mitigating systematic errors and present an optimal estimation algorithm capable of delivering unprecedented astrometric precision and accuracy from the ground. We verify the performance of our technique using experimental data, and discuss the astrometric potential of adaptive optics on large aperture telescopes. We then apply our knowledge to track the motions of magnetars. These objects harbor ultra-strong magnetic fields and give rise to the most intense high-energy transients in the sky. The proper motion survey presented here is the first of its kind, and is capable of directly addressing the open questions regarding their origin and evolution in a model independent fashion. We also present radio studies of the aftermath of the brightest magnetar flare ever recorded. Finally, we shift to probing the emission mechanism of the oldest neutron stars, millisecond pulsars in globular clusters, that are revived at the end of their by lives their binary companions.

Contents

List of Figures

List of Tables

Chapter 1

Precision Astrometry with Adaptive Optics

Abstract

We investigate the limits of ground-based astrometry with adaptive optics using the core of the Galactic globular cluster M5. Adaptive optics systems provide near diffraction-limit imaging with the world's largest telescopes. The substantial improvement in both resolution and signal-to-noise ratio enables high-precision astrometry from the ground. We describe the dominant systematic errors that typically limit ground-based differential astrometry, and enumerate observational considerations for mitigating their effects. After implementing these measures, we find that the dominant limitation on astrometric performance in this experiment is caused by tilt anisoplanatism. We then present an optimal estimation technique for measuring the position of one star relative to a grid of reference stars in the face of this correlated random noise source. Our methodology has the advantage of reducing the astrometric errors as $\sim 1/\sqrt{t}$ and faster than the square root of the number of reference stars – effectively eliminating noise caused by atmospheric tilt to the point that astrometric performance is limited by centering accuracy. Using 50 reference stars, we demonstrate single-epoch astrometric precision of ≈ 1 mas in 1 second, decreasing to $\lesssim 100\,\mu$as in 2 minutes of integration time at the Hale 200-inch telescope. We also show that our astrometry is accurate to $\lesssim 100\,\mu$as for observations

separated by 2 months. Finally, we discuss the limits and potential of differential astrometry with current and next generation large aperture telescopes. At this level of accuracy, numerous astrometric applications become accessible, including planet detection, astrometric microlensing signatures, and kinematics of distant Galactic stellar populations.

1.1 Introduction

The benefits of astrometry have long been clear to astronomers. Measurements of parallax and proper motion yield model independent determinations of fundamental quantities like distance and velocity. It is not surprising that astrometry has motivated a wide variety of observational programs using many different techniques to answer fundamental questions in astrophysics. Potential applications span a wide range of physical scales including: planet detection, reconstruction of the Milky Way's formation, and tests of ΛCDM cosmology (e.g., Unwin et al. 2007).

The most ubiquitous astrometric measurements have been carried out with ground-based telescopes in the seeing limit. Monet et al. (1992) conducted visible light measurements of 72 stars ($V = 15$–20) using the 1.55 m US Naval Observatory astrometric reflector. This program achieved single epoch measurement precision ≈ 4 milliarcseconds (mas), and parallax accuracies ranging from 0.5–3 mas over ~ 5 yr baselines. Pravdo & Shaklan (1996) performed visible light measurements of stars in the cluster NGC 2420 ($V = 13$–16) and achieved single epoch precision of $\approx 150\,\mu$as in one hour, which motivated an astrometric survey for low-mass companions to nearby stars (e.g., Pravdo et al. 2004). More recently, 200–300 μas astrometric precision has been demonstrated with VLT/FORS in the visible (Lazorenko 2006; Lazorenko et al. 2007). Each of the above programs employed relatively narrow-field visible imagers (a few square arcminutes) to perform differential astrometry; however, the increasing availability of wide-angle imagers has motivated studies over larger fields. Anderson et al. 2006 performed similar experiments using a 33' × 34' visible camera on the ESO 2.2 m telescope, which resulted in 7 mas single-epoch precision.

Ground-based interferometers provide an alternative method for performing high precision astrometry, typically over very narrow fields relative to a single reference star. The Palomar Testbed Interferometer has used phase-referencing to achieve astrometric accuracies $\approx 100\,\mu$as for a $30''$ binary (Lane et al. 2000), and $\approx 20\,\mu$as over years for binaries with separations $\lesssim 1''$ (Muterspaugh et al. 2006). Due to its 40 cm apertures, this instrument is limited to targets with $K_s < 6$. Large aperture, ground-based interferometers equipped with adaptive optics systems, such as those at Keck (Colavita & Wizinowich 2003) and the VLT (Glindemann et al. 2000), can perform at similar levels to fainter limiting magnitudes (e.g., Boden et al. 2007).

Differential astrometric accuracies achieved in both single aperture and interferometric ground-based programs are fundamentally limited by atmospheric effects. In the seeing limit, single aperture observations suffer from image quality degradation and interferometers lose visibility fringe coherence due to atmospheric turbulence. In addition, all ground-based programs suffer from systematic effects due to differential atmospheric refraction and optical distortions.

Space-based observatories are one possible method for avoiding the effects of atmospheric turbulence. *Hipparcos* was the first space-based mission with astrometric goals, and achieved $\lesssim 1\,$mas astrometry over the mission lifetime on bright targets ($V \lesssim 9$ mag; Perryman et al. 1997). Currently, the only space-based telescope that can perform high-precision astrometry is *Hubble*. Both the imagers and the Fine Guidance Sensor have been characterized and well-utilized for astrometry at the $\lesssim 1\,$mas level (e.g., Anderson & King 2000, 2003b; Benedict et al. 2003). Two complimentary future space missions are aimed at achieving levels of astrometric performance 2–3 orders of magnitude below the *Hubble* performance levels. GAIA will catalog roughly one billion stars to $V \approx 20\,$mag over the entire sky with parallax accuracies ranging from 10–300 μas depending on the magnitude (Perryman et al. 2001). The Space Interferometry Mission (SIM) will take a pointed approach and enable microarcsecond (μas) astrometry on Galactic and extragalactic targets (Unwin et al. 2007).

Ground-based adaptive optics (AO) offer an alternative, more easily accessible and cost effective method for overcoming atmospheric turbulence over small fields

($\lesssim$ arcminute). The current generation of astronomical adaptive optics systems provide diffraction limited image quality at near-infrared wavelengths. Achieving the telescope's diffraction limit and the resulting boost in signal-to-noise ratio prove to be a powerful combination for astrometry. These two effects reduce the errors in determining stellar centers, increase the number of possible reference stars at small separations, and allow techniques for mitigating systematics (e.g., use of narrow-band filters to eliminate chromatic refraction; see §1.2).

The marked improvements in wavefront sensor technology and the development of laser beacons have rapidly increased the usable sky coverage of these systems (e.g., Wizinowich et al. 2006a). The increase in sky coverage, operation in the near-infrared, gain in signal-to-noise ratio, and the diffraction-limited image quality make astrometry with adaptive optics amenable to numerous Galactic applications spanning a wide number of fields: detection of astrometric companions, the improved determination of the mass-luminosity relation of stars, and the formation and evolution of compact objects (Unwin et al. 2007).

Here we present an optimal estimation technique appropriate for mitigating the astrometric errors arising in AO observations and demonstrate its potential with multi-epoch imaging of the core of the globular cluster M5 using the Hale 200-inch Telescope. We were able to achieve $\lesssim 100\,\mu$as astrometric precision in two minutes, and have maintained this accuracy over two months. In §1.2 we discuss the dominant noise terms that arise in ground-based astrometry and the experimental techniques we have adopted to control them. We lay out the framework of our reduction model and illustrate its salient properties with a numerical simulation in §1.4. We describe the observations of M5 and the results of applying the optimal estimation technique to the data in §1.3 and §1.5. This is followed in §1.6 by a discussion of the role and potential of adaptive optics in ground-based astrometry with current and future large aperture telescopes.

1.2 Astrometric Error Terms in Ground Based Astrometry

Ground-based optical and infrared imaging observations suffer from a number of errors that limit the accuracy and precision of astrometric measurements. Relative to seeing-limited observations, the diffraction-limited image quality afforded by adaptive optics modifies the relative importance of these error terms. This section describes the four largest effects and indicates observational considerations utilized in this experiment aimed at mitigating them.

1.2.1 Differential Tilt Jitter

With AO, the image motion of the guide star is removed with a flat tip-tilt mirror. This stabilizes the image of the guide star with respect to the imager to high accuracy. Any residual tip-tilt error is removed in subsequent analysis by calculating only differential offsets between the target of astrometry (not necessarily the AO guide star) and the reference stars. However, the difference in the tilt component of turbulence along any two lines of sight in the field of view causes a correlated, stochastic change in their measured separation, known as differential atmospheric tilt jitter.

More specifically, in propagating through the atmosphere to reach the telescope aperture, light from the target star and light from a reference star at a finite angular offset traverse different columns of atmospheric turbulence that are sheared. Differential atmospheric tilt jitter arises from the decorrelation in the tilt component of the wavefront phase aberration arising from this shearing effect. This differential tilt leads to a random, achromatic, and anisotropic fluctuation in the relative displacement of the two objects. The three-term approximation to the parallel and perpendicular components of the variance arising from differential atmospheric tilt jitter, assuming

Kolmogorov turbulence, is given by (Sasiela 1994)

$$\begin{bmatrix}\sigma^2_{\parallel,\mathrm{TJ}}\\ \sigma^2_{\perp,\mathrm{TJ}}\end{bmatrix} = 2.67\frac{\mu_2}{D^{1/3}}\left(\frac{\theta}{D}\right)^2\begin{bmatrix}3\\1\end{bmatrix} - 3.68\frac{\mu_4}{D^{1/3}}\left(\frac{\theta}{D}\right)^4\begin{bmatrix}5\\1\end{bmatrix} + 2.35\frac{\mu_{14/3}}{D^{1/3}}\left(\frac{\theta}{D}\right)^{14/3}\begin{bmatrix}17/3\\1\end{bmatrix}. \tag{1.1}$$

In this equation D is the telescope diameter and θ is the angular separation of the stars. The turbulence moments μ_m are defined as

$$\mu_m = \sec^{m+1}\xi \int_0^\infty dh C_n^2(h) h^m, \tag{1.2}$$

where h is the altitude, ξ is the zenith angle, and $C_n^2(h)$ is the vertical strength of atmospheric turbulence. Typical $C_n^2(h)$ profiles yield $\sigma_{\parallel,\mathrm{TJ}} \approx$ 20–30 mas for a $20''$ binary when observed with a 5 m aperture. Note that the variance from differential tilt is a random error, and thus is also $\propto \tau_{\mathrm{TJ}}/t$, where τ_{TJ} is the tilt jitter timescale (of order the wind crossing time over the aperture; see §1.5) and t is the integration time.

1.2.2 Distortion

The largest instrumental systematic that limits the accuracy of astrometry in any optical system is geometric distortion. These distortions can be stable — resulting from unavoidable errors in the shape or placement of optics — or dynamic — resulting from the flexure or replacement of optics.

If geometric distortions are stable, then a number of strategies can be employed to mitigate their effect. One method is to model the distortion to high accuracy; the most notable example is the calibration of *HST* (e.g., Anderson & King 2003a). This is particularly important for data sets obtained with multiple instruments or those that use the technique of dithering, since knowledge of the distortion is necessary to place stellar positions in a globally correct reference frame. Alternatively, one could use a consistent optical prescription from epoch-to-epoch by using the same instrument and placing the field at the same location and orientation on the detector. Here we use both a distortion solution and a single, consistent dither position to

achieve accurate astrometry.

Any changes in the geometric distortion must be tracked through routine, consistent calibration. The question of stability is particularly important at the Hale 200-inch, since the AO system and the imaging camera (PHARO; see §1.3) are mounted at the Cassegrain focus, and PHARO undergoes a few warming/cooling cycles per month (see §1.3). The PHARO distortion solution[1] by Metchev (2006) accounts for changes in the orientation of the telescope (which are relatively small for our experimental design), but the overall stability of the system is best verified with on-sky data. One of the purposes of the data presented here is to track the system's stability. We find that the combination of the Hale Telescope, PALAO, and PHARO is capable of delivering $\lesssim 100\,\mu$as astrometry.

1.2.3 Atmospheric Refraction

Refraction by the Earth's atmosphere causes an angular deflection of light from a star, resulting in an apparent change in its position. The magnitude of this deflection depends on the wavelength and the atmospheric column depth encountered by an incoming ray. The former effect is chromatic, while the latter is achromatic. The error induced by differential chromatic refraction (DCR) has proven to be an important, and sometimes the dominant, astrometric limitation in ground-based efforts (e.g., Monet et al. 1992; Pravdo & Shaklan 1996; Anderson et al. 2006; Lazorenko 2006). These studies have shown DCR can contribute ≈ 0.1–1 mas of error depending on the wavelength and strategy of the observations.

The observations presented here were conducted using a Br-γ filter at $2.166\,\mu$m with a narrow bandpass of $0.02\,\mu$m to suppress differential chromatic refraction. The increased signal-to-noise ratio provided by adaptive optics allowed sufficient reference stars to be detected even through such a narrow filter in a short exposure time. We reach $K_s \approx 15$ magnitude in our 1.4 s exposures through this filter with the Hale 200-inch (see §1.3). In addition, observations were acquired over a relatively narrow

[1] see also http://www.astro.ucla.edu/∼metchev/ao.html

range of airmass (1.17–1.27) at each epoch to minimize the achromatic differential refraction.

In order to estimate the effect of atmospheric refraction on our data, we took the asterism in the core of M5 and refracted it to 37 and 32 degrees elevation with the parallactic angles appropriate for the observations on 2007 May 28 using the *slarefro* function distributed with the STARLINK library (Gubler & Tytler 1998). The root-mean-square (RMS) deviation in reference star positions between these two zenith angles was $\lesssim 250\,\mu$as and the shift in guide star position with respect to the grid (see §1.4) was $\approx 10\,\mu$as. Thus, our consistent zenith angle of observations, narrow-band filter and observations in the near-infrared (where the refraction is more benign) make the contribution of this effect negligible for our purposes, and we make no effort to correct for it.

Performing a similar experiment using a the broadband K filter with a field of $\approx 5000\,$K reference stars and a $\approx 3000\,$K target would lead to a systematic shift of $\approx 100\,\mu$as between zenith angles separated by 10°, which would be detectable by this experiment. Consequently, for observations where broadband filters are necessary, refraction effects must be considered and corrected.

1.2.4 Measurement Noise

In the case of a perfect optical system, a perfect detector and no atmosphere, the astrometric precision is limited by one's ability to calculate stellar centers. The centering precision is determined by measurement noise, and we will use the two terms interchangeably. For a monopupil telescope, the uncertainty is

$$\sigma_{\rm meas} = \frac{\lambda}{\pi D}\frac{1}{\rm SNR} = 284\,\mu{\rm as}\left(\frac{\lambda}{2.17\,\mu{\rm m}}\right)\left(\frac{5\,{\rm m}}{D}\right)\left(\frac{100}{\rm SNR}\right) \tag{1.3}$$

(Lindegren 1978). Adaptive optics allow us to achieve the diffraction limit even in the presence of the atmosphere and substantially boosts the SNR over the seeing-limited case — thereby decreasing measurement noise and improving astrometric precision.

In practice, the centering of a given stellar image is limited by spatial and temporal

Table 1.1. Palomar Observations of M5

Date	Time	Integration Time (sec)	Airmass	Seeing[a] (asecs)	θ_0[a] (asecs)	μ_2 ($m^{7/3}$)	μ_4 ($m^{13/3}$)	$\mu_{14/3}$ ($m^{15/3}$)
2007-05-28	05:18:29 - 06:19:29	890	1.26 - 1.18	1.22	2.34	1.01e-5	3.82e3	2.77e6
2007-05-29	05:58:26 - 06:48:30	570	1.19 - 1.17	1.39	2.16	1.14e-5	3.89e3	2.82e6
2007-07-22	03:57:12 - 04:40:36	630	1.20 - 1.27	1.05	1.66	1.74e-5	6.46e3	4.71e6

[a]Calculated at a wavelength of 0.5 μm. These quantities scale as $\lambda^{1/5}$ and $\lambda^{6/5}$, respectively.

variations in the AO point-spread function (PSF). A great deal of time and effort has been spent determining the AO PSF and producing software packages to perform PSF fitting (e.g., Diolaiti et al. 2000; Britton 2006). However, any PSF-fitting software package is capable of calculating image positions at $\lesssim 0.01$ pixel level in a single image. For the observations considered here this is $\lesssim 2$ mas, a factor of 5 – 10 larger than the measurement noise in Equation 1.3, but it is much smaller than the tilt jitter mentioned in §1.2.1. As such, we have chosen to use simple and widely available PSF centering software (DAOPHOT; Stetson 1987; see §1.3).

1.3 Observations and Data Reduction

We observed the globular cluster M5 on three dates spanning 2 months (see Table 1.1 for a summary of observations) using the Hale 200-inch telescope and the Palomar High Angular Resolution Observer (PHARO; Hayward et al. 2001) assisted by the Palomar Adaptive Optics System (PALAO; Troy et al. 2000). The globular cluster M5 was chosen for its relatively large distance of ≈ 7.5 kpc from the Sun, low velocity dispersion of $\approx 5\,\mathrm{km\,s^{-1}}$, and the availability of guide stars near the cluster core (Pryor & Meylan 1993; Harris 1996). This combination of distance and velocity yields an expected cluster dispersion of only $140\,\mu\mathrm{as\,yr^{-1}}$, or 20 μas over our 2 month observing span. We acquired 400–600 images per night. A typical image can be found in Figure 1.1. The guide star is a red giant branch member of the globular cluster with $V \approx 12.6$ magnitude (Sandquist & Bolte 2004). The cluster was imaged through the narrow-band Br-γ filter (central wavelength is 2.166 μm and bandpass is 0.02 μm)

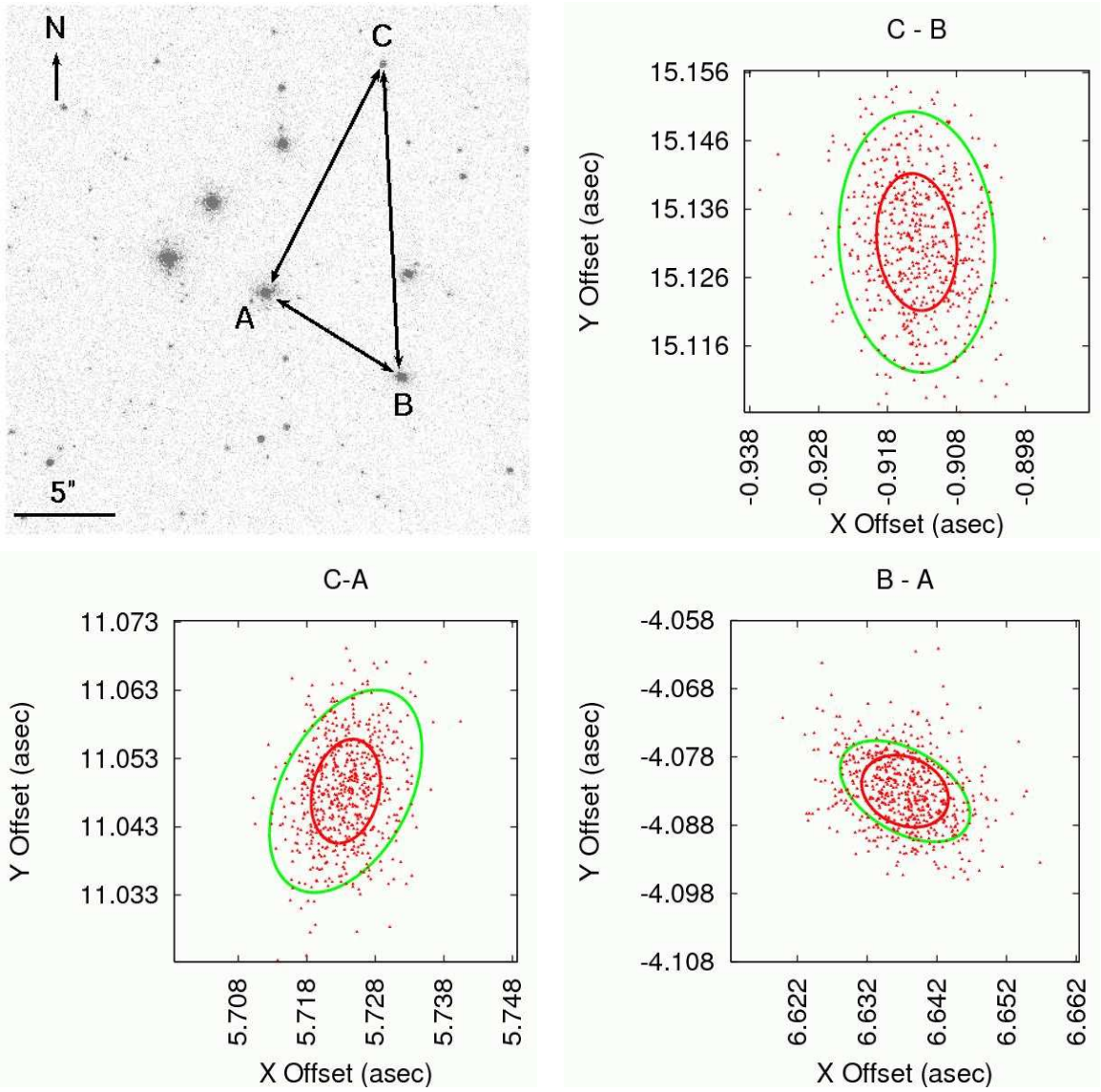

Figure 1.1 *Top left:* Image of the core of the globular cluster M5 in 1.4 seconds through the narrow-band Br-γ filter. The AO guide star is labeled as star 'A', and is one of 82 detected stars in the image. The additional plots show the measured x-y angular separation of each pair of stars denoted by the arrows in 600 images taken on 28 May 2007. These plots show the clear signature of anisotropic differential atmospheric tilt jitter as predicted from Equation 1.1. The measured (red) and predicted (green) $1\,\sigma$ error ellipses are over-plotted. We see that temporal averaging over the 1.4 second exposure time has reduced the measured variance with respect to that predicted from the DIMM/MASS measurements and Equation 1.1.

using the $25'' \times 25''$ narrow-field channel ($0.025''\,\mathrm{pixel}^{-1}$), which over samples the 87 mas diffraction-limited PSF. The brightest star filled the detector to 10% of the maximum well-depth in the 1.4 sec exposure time — well within the linear regime of the detector.

Contemporaneous measurements of the atmospheric turbulence profile were acquired with a differential image motion monitor (DIMM) and multi-aperture scintillation sensor (MASS), which have been deployed as a single unit in a dome at Palomar Observatory (Thomsen et al. 2007; Kornilov et al. 2007). These turbulence profile measurements permitted an independent estimate of the magnitude of differential tilt jitter (computed using Equation 1.1).

We processed the raw images by subtracting dark frames and removing bad pixels from the analysis. Flat-field calibration was performed using twilight sky flats. Sky subtraction was accomplished by forming the median of the dithered frames taken outside of the cluster and subtracting this median from each exposure. The photometry and astrometry of each star was extracted using PSF-fitting as implemented by the DAOPHOT package in PyRAF[2]. DAOPHOT is not optimized for astrometry (see e.g., Anderson & King 2000), and since our measurement model reduces the noise due to atmospheric turbulence, our single epoch precision could be improved with a more careful centering technique (see §1.4.4 and §1.5.2). However, our astrometric accuracy over 2 months is not limited by this choice (see §1.5.3). We used the four brightest stars in the field to derive a model PSF that is assumed to be constant over the field, and calibrated the image zeropoints using 2MASS and found that the guide star has $K_s \approx 9.1$ magnitude.

[2]PyRAF is a product of Space Telescope Science Institute, which is operated by AURA for NASA.

1.4 Grid Astrometry for Ground-based Adaptive Optics Observations

After controlling for distortion and atmospheric refraction, the dominant astrometric errors are caused by differential atmospheric tilt jitter and measurement noise. In this section we present a general framework for measuring the position of a star relative to a grid of reference stars in the face of these noise sources. This framework has two key ingredients. The first is the covariance matrix ($\mathbf{\Sigma_d}$), which encapsulates the relevant statistical uncertainties for astrometry with adaptive optics. The second is the weight matrix ($\mathbf{W}$), which determines how the differential measurements between the target star and the reference stars are combined to calculate the target's position relative to the grid.

1.4.1 Measurement Model

The fundamental quantity in differential astrometry is the measured angular offset between a pair of stars. We will denote the angular distance between two stars, i and j, as $\vec{d}_{ij}$. Since $\vec{d}_{ij}$ is measured from an image, we will denote its components in the Cartesian coordinate system of the detector, simply

$$\vec{d}_{ij} = \begin{bmatrix} x_j - x_i \\ y_j - y_i \end{bmatrix} \equiv \begin{bmatrix} x_{ij} \\ y_{ij} \end{bmatrix}, \tag{1.4}$$

where we have introduced the notation $x_{ij} \equiv x_j - x_i$ and likewise for y. The variance in the angular separation between two stars is given by

$$\begin{bmatrix} \sigma^2_{\parallel} \\ \sigma^2_{\perp} \end{bmatrix} = \begin{bmatrix} \sigma^2_{\parallel,\mathrm{meas}} \\ \sigma^2_{\perp,\mathrm{meas}} \end{bmatrix} + \frac{\tau_{\mathrm{TJ}}}{t} \begin{bmatrix} \sigma^2_{\parallel,\mathrm{TJ}} \\ \sigma^2_{\perp,\mathrm{TJ}} \end{bmatrix}, \tag{1.5}$$

where $\sigma^2_{\parallel,\mathrm{meas}}$ is the sum of the squares of the centering errors of each star parallel to the axis connecting the pair (and similarly for the perpendicular variance), and the remaining terms are as defined in §1.2.1.

Measurement of the offset between the target star (which we will denote with a

subscript $i = 0$) and each of the N reference stars results in a set of N vectors, $\vec{d}_{0i}$. For simplicity, we will write these measured offsets as a single column vector,

$$\mathbf{d} = [x_{01}, \cdots, x_{0N}, y_{01}, \cdots, y_{0N}]^{\mathrm{T}}. \tag{1.6}$$

The goal of differential astrometry is to use $\mathbf{d}$ to determine the position of the target star with respect to the reference grid of stars at each epoch.

There are many possible ways to construct the position of the astrometric target from a given $\mathbf{d}$. Here we use the most general linear combination of the angular offsets, namely

$$\vec{p} = \mathbf{W}\mathbf{d}, \tag{1.7}$$

where $\mathbf{W}$ is the $2 \times 2N$ weight matrix, given by

$$\mathbf{W} = \begin{bmatrix} w_{xx,01} & \cdots & w_{xx,0N} & w_{xy,01} & \cdots & w_{xy,0N} \\ w_{yx,01} & \cdots & w_{yx,0N} & w_{yy,01} & \cdots & w_{yy,0N} \end{bmatrix}. \tag{1.8}$$

We have used the notation $w_{xy,0i}$ to denote the weighting of the offset from the target star to star i in the y direction used to determine the x component of the target's position, $\vec{p}$. For example, for a standard average of the x and y measurements to calculate $\vec{p}$, we would assign all the $w_{xx,0i} = w_{yy,0i} = 1/N$ and $w_{xy,0i} = w_{yx,0i} = 0$.

In principle, we are free to assign weights in any manner we please. However, we find it convenient to choose the weights such that they satisfy

$$\sum_i w_{xx,0i} = 1 \quad , \quad \sum_i w_{yy,0i} = 1 \quad , \sum_i w_{xy,0i} = 0 \quad , \quad \sum_i w_{yx,0i} = 0. \tag{1.9}$$

These constraints ensure that the components of $\vec{p}$ have physical units (e.g., pixels or arcseconds) and that its components are measured in the same coordinate system as $\mathbf{d}$ (presumably the detector coordinates). As a consequence, $\vec{p}$ represents the position of the target star in the sense that a proper motion of the target, $\vec{\epsilon}$, with respect to the fixed grid between two epochs will cause a change, $\vec{p} \to \vec{p} + \vec{\epsilon}$.

In order to determine if any change in $\vec{p}$ over time is meaningful, we must under-

stand its statistical properties. Both differential tilt jitter and measurement errors are assumed to follow Gaussian statistics, so that each instance of target-reference grid offset measurements, $\mathbf{d}$, is drawn from a multivariate normal probability distribution:

$$P(\mathbf{d}) = \frac{1}{\sqrt{2\pi \det \mathbf{\Sigma_d}}} \exp\left(\frac{1}{2}[\mathbf{d}-\bar{\mathbf{d}}]^{\mathrm{T}} {\mathbf{\Sigma_d}}^{-1} [\mathbf{d}-\bar{\mathbf{d}}]\right), \tag{1.10}$$

where $\mathbf{\Sigma_d}$ is the covariance matrix, and the bars above the symbols denote using the average value of each matrix entry.

The statistics of $\vec{p}$ follow in a straightforward manner from Equation 1.10 given our choice in Equation 1.7. Since $\vec{p}$ is a linear function of $\mathbf{d}$, each $\vec{p}$ is also drawn from a multivariate normal probability distribution with covariance matrix

$$\mathbf{\Sigma}_p = \mathbf{W}^{\mathrm{T}} \mathbf{\Sigma_d} \mathbf{W}, \tag{1.11}$$

and the uncertainties of $\vec{p}$ are described by the eigenvectors and eigenvalues of $\mathbf{\Sigma}_p$. Thus, our goal of optimally determining the target's position requires calculating the covariance matrix, $\mathbf{\Sigma_d}$, from data or theory, and choosing, $\mathbf{W}$, to minimize the eigenvalues of $\mathbf{\Sigma}_p$.

1.4.2 The Covariance Matrix

We have chosen to measure positions and offsets in the Cartesian coordinates of the detector, so the form of the covariance matrix, given our definitions above, is

$$\mathbf{\Sigma_d} = \begin{pmatrix} \langle(\Delta x_{01})^2\rangle & \cdots & \langle(\Delta x_{01})(\Delta x_{0N})\rangle & \langle(\Delta x_{01})(\Delta y_{01})\rangle & \cdots & \langle(\Delta x_{01})(\Delta y_{0N})\rangle \\ & \ddots & \vdots & \vdots & \ddots & \vdots \\ & & \langle(\Delta x_{0N})^2\rangle & \langle(\Delta x_{0N})(\Delta y_{01})\rangle & \cdots & \langle(\Delta x_{0N})(\Delta y_{0N})\rangle \\ & & & \langle(\Delta y_{01})^2\rangle & \cdots & \langle(\Delta y_{01})(\Delta y_{0N})\rangle \\ & & & & \ddots & \vdots \\ \text{symmetric} & & & & & \langle(\Delta y_{0N})^2\rangle \end{pmatrix}, \tag{1.12}$$

where we have written $\Delta x_{ij} \equiv (x_{ij} - \bar{x}_{ij})$ to simplify the notation (likewise for y).

The total covariance matrix has contributions from centering errors and differential atmospheric tilt jitter. Since these contributions are independent, the total covariance matrix can be written $\mathbf{\Sigma_d} = \mathbf{\Sigma}_{\rm meas} + \mathbf{\Sigma}_{\rm TJ}$, and each term can be derived separately.

1.4.2.1 The Covariance Matrix for Measurement Noise

In the absence of differential tilt jitter, it is straightforward to construct the covariance matrix for measurement noise alone, $\mathbf{\Sigma}_{\rm meas}$. The diagonal terms can be written

$$\langle \Delta x_{0i}^2 \rangle \equiv \sigma_{x,0i}^2 = \sigma_{x,0}^2 + \sigma_{x,i}^2, \tag{1.13}$$

where $\sigma_{x,i}$ and $\sigma_{x,0}$ are the uncertainties in determining the x-position of star i and the target star, respectively. For the off-diagonal terms $\langle \Delta x_{0i} \Delta x_{0j} \rangle$, we can use the fact that

$$\begin{aligned}
\langle \Delta x_{0i} \Delta x_{0j} \rangle &= \frac{1}{2} \langle \{ \Delta x_{0i}^2 + \Delta x_{0j}^2 - [\Delta x_{0i} - \Delta x_{0j}]^2 \} \rangle \\
&= \frac{1}{2} \{ \langle \Delta x_{0i}^2 \rangle + \langle \Delta x_{0j}^2 \rangle - \langle [\Delta x_{0i} - \Delta x_{0j}]^2 \rangle \} \\
&= \frac{1}{2} \{ \langle \Delta x_{0i}^2 \rangle + \langle \Delta x_{0j}^2 \rangle - \langle \Delta x_{ij}^2 \rangle \} \\
&= \frac{1}{2} (\sigma_{x,0i}^2 + \sigma_{x,0j}^2 - \sigma_{x,ij}^2) \\
&= \sigma_{x,0}^2.
\end{aligned} \tag{1.14}$$

where we have used only algebra and the definitions above. Equation 1.14 is the obvious result of the fact that the measurements of the target star's coordinates are common to all differential measurements, and so its uncertainty appears in all the off-diagonal covariance terms, $\langle \Delta x_{0i} \Delta x_{0j} \rangle$ and $\langle \Delta y_{0i} \Delta y_{0j} \rangle$. However, the cross-terms involving both x and y (e.g., $\langle \Delta x_{0i} \Delta y_{0j} \rangle$) vanish because $\sigma_{x,0}$ and $\sigma_{y,0}$ are uncorrelated for measurement noise alone.

1.4.2.2 The Covariance Matrix for Differential Tilt Jitter

The covariance matrix for differential atmospheric tilt jitter between a pair of stars is diagonal when written in an orthogonal coordinate system, with one axis lying along the separation axis of the binary. We see from Equation 1.1 that it can be written as

$$\mathbf{\Sigma}_{\rm pair} = \begin{pmatrix} \langle (d_\parallel - \bar{d}_\parallel)^2 \rangle & \langle (d_\parallel - \bar{d}_\parallel)(d_\perp - \bar{d}_\perp) \rangle \\ \langle (d_\parallel - \bar{d}_\parallel)(d_\perp - \bar{d}_\perp) \rangle & \langle (d_\perp - \bar{d}_\perp)^2 \rangle \end{pmatrix} = \begin{pmatrix} \sigma^2_{\parallel,\rm TJ} & 0 \\ 0 & \sigma^2_{\perp,\rm TJ} \end{pmatrix}, \tag{1.15}$$

where $d_\parallel$ and $d_\perp$ are the angular offsets parallel and perpendicular to the axis connecting the pair of stars, respectively.

For a general field of N stars, no coordinate system exists that diagonalizes the full tilt jitter covariance matrix, $\mathbf{\Sigma}_{\rm TJ}$. But, we can begin computing the entries by rotating $\mathbf{\Sigma}_{\rm pair}$ into our x-y coordinates via $\mathbf{R}^{\rm T}\mathbf{\Sigma}_{\rm pair}\mathbf{R}$, where

$$\mathbf{R} = \begin{pmatrix} \cos\phi & \sin\phi \\ -\sin\phi & \cos\phi \end{pmatrix}. \tag{1.16}$$

The result is

$$\mathbf{R}^{\rm T}\mathbf{\Sigma}_{\rm pair}\mathbf{R} = \begin{pmatrix} \sigma^2_{\parallel,0i}\cos^2\phi_{0i} + \sigma^2_{\perp,0i}\sin^2\phi_{0i} & (\sigma^2_{\parallel,0i} - \sigma^2_{\perp,0i})\cos\phi_{0i}\sin\phi_{0i} \\ (\sigma^2_{\parallel,0i} - \sigma^2_{\perp,0i})\cos\phi_{0i}\sin\phi_{0i} & \sigma^2_{\parallel,0i}\sin^2\phi_{0i} + \sigma^2_{\perp,0i}\cos^2\phi_{0i} \end{pmatrix}, \tag{1.17}$$

where ϕ_{0i} is the angle between $\vec{d}_{0i}$ and our arbitrary Cartesian system measured counterclockwise from the x-axis, and we have introduced the notation that the uncertainty parallel to $\vec{d}_{ij}$ is $\sigma_{\parallel,ij}$ and the uncertainty orthogonal to $\vec{d}_{ij}$ is $\sigma_{\perp,ij}$ as calculated from Equation 1.1. Thus, we can identify the diagonal terms

$$\begin{aligned} \langle \Delta x^2_{0i} \rangle &= \sigma^2_{\parallel,0i}\cos^2\phi_{0i} + \sigma^2_{\perp,0i}\sin^2\phi_{0i}, \\ \langle \Delta y^2_{0i} \rangle &= \sigma^2_{\parallel,0i}\sin^2\phi_{0i} + \sigma^2_{\perp,0i}\cos^2\phi_{0i}, \end{aligned} \tag{1.18}$$

and

$$\langle \Delta x_{0i}\Delta y_{0i} \rangle = (\sigma^2_{\parallel,0i} - \sigma^2_{\perp,0i})\cos\phi_{0i}\sin\phi_{0i}. \tag{1.19}$$

For the off-diagonal terms $\langle \Delta x_{0i} \Delta x_{0j} \rangle$, we notice that (as used in Equation 1.14)

$$\begin{aligned}
\langle \Delta x_{0i} \Delta x_{0j} \rangle &= \frac{1}{2} \langle \{ \Delta x_{0i}^2 + \Delta x_{0j}^2 - [\Delta x_{0i} - \Delta x_{0j}]^2 \} \rangle \\
&= \frac{1}{2} \{ \langle \Delta x_{0i}^2 \rangle + \langle \Delta x_{0j}^2 \rangle - \langle [\Delta x_{0i} - \Delta x_{0j}]^2 \rangle \} \\
&= \frac{1}{2} (\sigma_{\parallel,0i}^2 \cos^2 \phi_{0i} + \sigma_{\perp,0i}^2 \sin^2 \phi_{0i} + \sigma_{\parallel,0j}^2 \cos^2 \phi_{0j} + \sigma_{\perp,0j}^2 \sin^2 \phi_{0j} \\
&\quad - \sigma_{\parallel,ij}^2 \cos^2 \phi_{ij} - \sigma_{\perp,ij}^2 \sin^2 \phi_{ij}), \qquad (1.20)
\end{aligned}$$

where in the last step we have used the fact that $x_{ij} = x_{0i} - x_{0j}$ and the relations in Equations 1.18 and 1.19. The quantities $\langle \Delta y_{0i} \Delta y_{0j} \rangle$ can be obtained by interchanging sine and cosine in Equation 1.20.

For the remaining off-diagonal terms $\langle \Delta x_{0i} \Delta y_{0j} \rangle$, we can use the fact that

$$\begin{aligned}
\langle \Delta x_{0i} \Delta y_{0j} \rangle &= \langle \Delta x_{0i} [\Delta y_{0i} + \Delta y_{ij}] \rangle \\
&= \langle \Delta x_{0i} \Delta y_{0i} \rangle + \langle \Delta x_{0i} \Delta y_{ij}] \rangle \\
&= \langle \Delta x_{0i} \Delta y_{0i} \rangle + \langle [\Delta x_{0j} - \Delta x_{ij}] \Delta y_{ij} \rangle \\
&= \langle \Delta x_{0i} \Delta y_{0i} \rangle + \langle \Delta x_{0j} \Delta y_{ij} \rangle - \langle \Delta x_{ij} \Delta y_{ij} \rangle \\
&= \langle \Delta x_{0i} \Delta y_{0i} \rangle + \langle \Delta x_{0j} [\Delta y_{0j} - \Delta y_{0i}] \rangle - \langle \Delta x_{ij} \Delta y_{ij} \rangle \\
&= \langle \Delta x_{0i} \Delta y_{0i} \rangle + \langle \Delta x_{0j} \Delta y_{0j} \rangle - \langle \Delta x_{ij} \Delta y_{ij} \rangle - \langle \Delta x_{0j} \Delta y_{0i} \rangle. \qquad (1.21)
\end{aligned}$$

Rearranging gives

$$\langle \Delta x_{0i} \Delta y_{0j} \rangle + \langle \Delta x_{0j} \Delta y_{0i} \rangle = \langle \Delta x_{0i} \Delta y_{0i} \rangle + \langle \Delta x_{0j} \Delta y_{0j} \rangle - \langle \Delta x_{ij} \Delta y_{ij} \rangle. \qquad (1.22)$$

All the terms in the right-hand side are known from Equation 1.19, and further investigation shows that the two terms on the left-hand side are equal. So, Equations 1.13, 1.14, 1.18, 1.19, 1.20, and 1.22 contain all the information required to construct the full covariance matrix, $\mathbf{\Sigma_d}$.

1.4.3 The Optimal Weight Matrix

The optimal choice of weights in Equation 1.3 are those which minimize the eigenvalues in Equation 1.11. For a 2×2 symmetric matrix the sum of the eigenvalues is the trace of the matrix, so our problem becomes one of minimizing the trace of $\mathbf{\Sigma_p}$ subject to the constraints in Equation 1.9. Specifically, we will use the method of Lagrange multipliers (Betts 1980) to find the optimal weights, $\mathbf{W'}$, that minimize the quadratic equation

$$\mathrm{Tr}(\mathbf{\Sigma_p}) = \frac{1}{2}\mathbf{W'}^{\mathrm{T}}\mathbf{S}\mathbf{W'}, \tag{1.23}$$

where

$$\mathbf{S} = \begin{bmatrix} \mathbf{\Sigma_d} & \mathbf{0} \\ \mathbf{0} & \mathbf{\Sigma_d} \end{bmatrix}, \tag{1.24}$$

is a $4N \times 4N$ matrix, and

$$\mathbf{W'} = [w_{xx,01}, \cdots, w_{xx,0N},\ w_{xy,01}, \cdots, w_{xy,0N},\ w_{yx,01}, \cdots, w_{yx,0N},\ w_{yy,01}, \cdots, w_{yy,0N}]^{\mathrm{T}} \tag{1.25}$$

is a vector of length $4N$. Note that $\mathbf{W'}$ has identical entries as $\mathbf{W}$ in Equation 1.8; it is just written as a single vector to cast the minimization problem into a single equation (1.23). We want to find the extrema of Equation 1.23 subject to the linear constraints in Equation 1.9, which can be written

$$\mathbf{C}\mathbf{W'} = \mathbf{V}, \tag{1.26}$$

where we define the $4 \times 4N$ symmetric matrix

$$\mathbf{C} = \begin{bmatrix} 1 & \cdots & 1 & 0 & \cdots & 0 & 0 & \cdots & 0 & 0 & \cdots & 0 \\ & & & 1 & \cdots & 1 & 0 & \cdots & 0 & 0 & \cdots & 0 \\ & & & & & & 1 & \cdots & 1 & 0 & \cdots & 0 \\ \mathrm{sym} & & & & & & & & & 1 & \cdots & 1 \end{bmatrix}, \tag{1.27}$$

and

$$\mathbf{V} = \begin{bmatrix} 1 \\ 0 \\ 0 \\ 1 \end{bmatrix}. \tag{1.28}$$

In this framework the optimal weights are those that solve the system of linear equations

$$\begin{bmatrix} \mathbf{S} & \mathbf{C}^{\mathrm{T}} \\ \mathbf{C} & \mathbf{0} \end{bmatrix} \begin{bmatrix} \mathbf{W}' \\ \lambda \end{bmatrix} = \begin{bmatrix} \mathbf{0} \\ \mathbf{V} \end{bmatrix}. \tag{1.29}$$

Here λ are the Lagrange multipliers, which will not be used further. Equation 1.29 can be solved via a matrix inversion.

Note that the general constraints on the weights we have written in Equation 1.9 and 1.26 have two somewhat unintuitive features. The first is that the y measurements are sometimes used to compute the x position and vice versa. The other property is that they allow for negative weights, meaning that in some cases certain measurements will be subtracted in calculating the position of the astrometric target, $\vec{p}$. These two facts conspire to exploit the natural correlations inherent in the data. The flexible and possibly negative weights essentially allow the reference grid to be symmetrized, thereby using the known correlations to cancel noise so as to minimize the variance in $\vec{p}$.

1.4.4 Numerical Simulations

As indicated in the above analysis, the single epoch uncertainty in the location, $\vec{p}$, of the target relative to the grid of reference stars is represented by the eigenvalues and eigenvectors of the 2×2 matrix $\mathbf{\Sigma}_p$ (Equation 1.11). This matrix itself depends on the distribution of reference stars, the precision of centering measurements, and the degree of noise correlation due to differential tilt through the matrix $\mathbf{\Sigma_d}$. In this way, the intrinsic precision of the measured value of $\vec{p}$ depends on these three factors.

To ascertain the behavior of $\mathbf{\Sigma}_p$ with the density of available reference stars, we

performed a series of numerical simulations. In each simulation, N ($2 \leq N \leq 100$) stars were randomly distributed throughout a $25'' \times 25''$ field of view. We assumed the target was a bright star in the middle of the field with centering error of 0.5 mas and the reference stars were fainter, drawn from a Gaussian distribution with mean centering error of 2 mas and a standard deviation of 1 mas (somewhat analogous to the situation for the guide star in M5; see §1.5). The full covariance matrix, $\mathbf{\Sigma_d}$, was computed for each stellar configuration assuming these centering errors, the typical turbulence profile above Palomar Observatory, and a 1.4 sec exposure time.

In the first simulation, $\mathbf{\Sigma_d}$ was contracted as in Equation 1.11 using standard averaging for $\mathbf{W}$ ($w_{xx,0i} = w_{yy,0i} = 1/N$; $w_{xy,0i} = w_{yx,0i} = 0$). For the second simulation, $\mathbf{\Sigma_d}$ was contracted using the optimal $\mathbf{W}$ as calculated using the prescription in §1.4.3. In each case, the geometric mean of the two eigenvalues of the resulting matrix, $\mathbf{\Sigma}_p$, were computed to form an estimate of the single epoch measurement precision of $\vec{p}$. To average away random effects arising from the particular geometry of the random distribution of stars, each numerical simulation was repeated for 100 random distributions of stars for each value of N, and these were averaged to generate a mean value for the single epoch measurement precision.

The resulting values for the single epoch measurement precision of $\vec{p}$ are shown in Figure 1.2 as a function of the number of reference stars, along with the contributions of measurement noise and differential tilt jitter. In both simulations, the error due to measurement noise decreases as $N^{-0.3}$. However, in the limit of an infinite number of reference stars, this error asymptotes to the target star's measurement error. The rate at which the measurement noise decreases to this value depends on the distribution of reference star measurement errors.

The important distinction between the two simulations is the contribution of tilt jitter to astrometric performance. In the simulation utilizing standard averaging, there is very little gain with increased stellar density ($N^{-0.15}$), and tilt jitter dominates the error budget. However, the optimal estimation algorithm rapidly ($N^{-0.7}$) eliminates the contribution of differential tilt by taking advantage of the correlations inherent in $\mathbf{\Sigma_d}$ and the flexibility to symmetrize the reference field through the choice

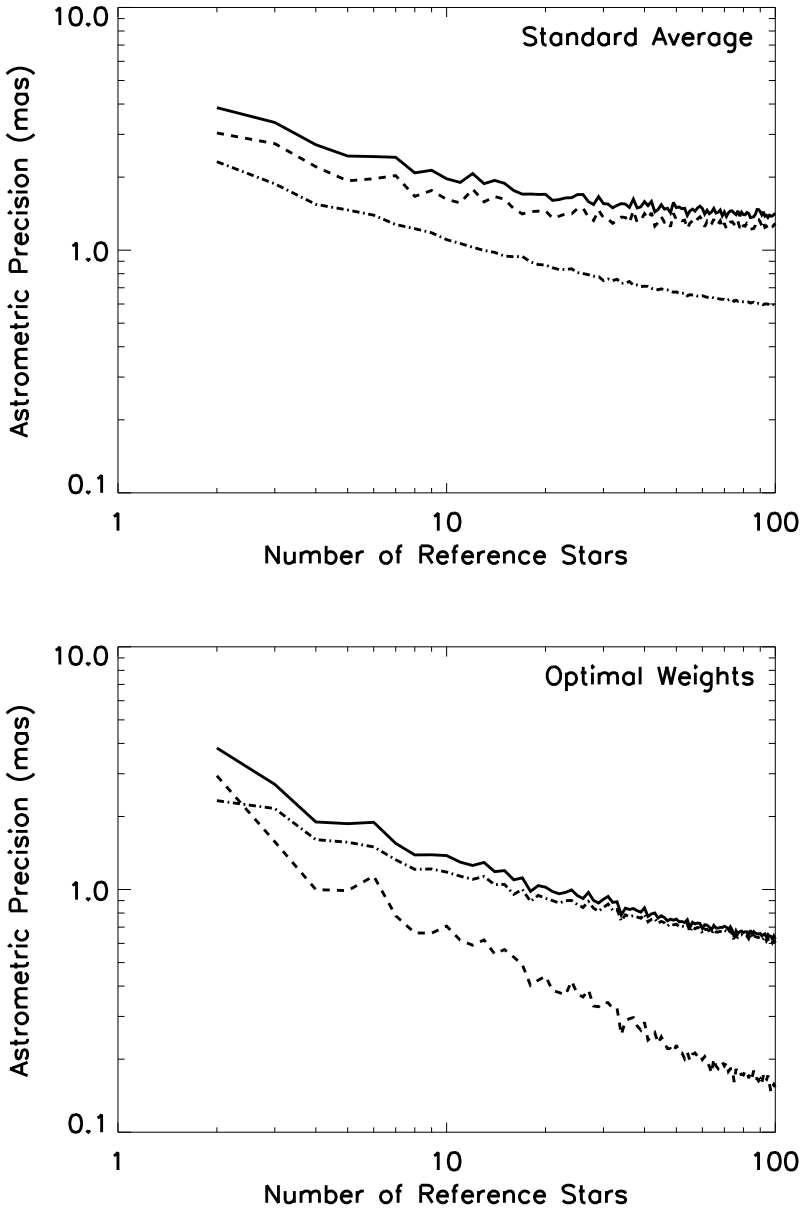

Figure 1.2 *Top:* Simulated astrometric precision as a function of the number of reference stars using standard averaging (solid line). The total astrometric precision has contributions from the measurement noise (dash-dotted) and the differential atmospheric tilt jitter (dashed line). Here the measurement noise was taken to be 0.5 mas for the AO guide star, and the reference stars were drawn from a normal distribution with a mean of 2 mas and standard deviation of 1 mas. The tilt jitter is that expected in a 1.4 sec exposure assuming the turbulence profile measured on the night of 2007 May 28 at Palomar Observatory (see Table 1.1). *Bottom:* Simulated astrometric precision as a function of the number of reference stars using optimal weighting (lines as above). By using optimal weighting, based on the covariance matrix, the effect of atmospheric noise is reduced to values less than measurement noise.

of weights.

1.5 Analysis and Results

In the analysis that follows, we will use the measurement model described in §1.4. For a given target star, we will calculate the differential offsets with respect to the grid stars to generate a value of $\mathbf{d}$ for each image at each epoch (Equation 1.6). We then use either these data or the theory in §1.4.2 to generate the full covariance matrix, $\mathbf{\Sigma_d}$. From $\mathbf{\Sigma_d}$, we use the prescription in §1.4.3 to calculate the optimal weights, $\mathbf{W}$. These weights are used to combine the differential offsets to generate the target star's position, $\vec{p}$, in each image via Equation 1.7. The statistics of the positional measurements are then described by the covariance matrix, $\mathbf{\Sigma}_p$, from Equation 1.11.

1.5.1 Differential Tilt Jitter

In order to test our expectation that tilt jitter dominates the astrometric error, we calculate the RMS of the angular offsets for pairs of stars in the field (Figures 1.1 and 1.3). These results clearly show the characteristic signature of differential tilt. Namely, the RMS separation along the axis connecting the two stars is larger than that of the perpendicular axis by a factor of $\approx \sqrt{3}$. However, the magnitude of the tilt jitter is smaller than the theoretical expectations, which suggests that some of the tilt jitter has been averaged away in the 1.4 sec exposure time.

We have no direct measurement of the wind speed profile over the telescope to calculate the expected tilt jitter timescale. Instead, we fit the observed σ_{ij}^2 and angular offsets using the model in Equation 1.5 with $t = 1.4$ seconds. The best fit values are $\sigma_{\rm meas,ij} \approx 2$ mas and $t/\tau_{\rm TJ} \approx 7$. This implies that the characteristic timescale for tilt jitter is ≈ 0.2 seconds, resulting in a wind crossing time of $25\,{\rm m\,sec^{-1}}$. Turbulence at higher altitudes contributes most to the differential atmospheric tilt jitter, and this velocity is typical of wind speeds in the upper atmosphere (Greenwood 1977). It is also clear from the figure that a number of stars have measurement noise that is much

less than 2 mas, thus this number should only be taken as characteristic of the faint stars.

1.5.2 Astrometric Precision

The astrometric precision achieved in a single epoch is an important diagnostic of the measurement model. On a given night for a given star, we investigate the use of both the ≈ 500 images and the theory in §1.4.2 to calculate $\mathbf{\Sigma_d}$, leading to the optimal weights. We then apply this weight matrix to the measured offsets to compute the target's position in each image — resulting in a timeseries in each component of $\vec{p}$ for each epoch. The properties of each timeseries are best explored by computing its Allan deviation (also known as the square root of the two-sample variance). The Allan deviation is calculated by dividing a timeseries into chunks, averaging each segment, and computing the RMS of the resulting, shorter timeseries. If the timeseries is dominated by random errors, its Allan deviation will decrease as $1/\sqrt{t_{\rm avg}}$, where $t_{\rm avg}$ is the length of each chunk. It is also necessary to have sufficiently many segments so that an RMS calculation is meaningful. Here the longest timescale probed is $\approx$ 2–3 minutes for each 10–15 minute timeseries.

We compute the geometric mean of the Allan deviation in each dimension as a function of the averaging time for the AO guide star in Figure 1.4 after computing the covariance matrix from data. After 1.4 seconds, the guide star's positional precision is $\approx 600\,\mu$as. The precision subsequently improves as $t^{-0.51\pm0.08}$ to $\approx 70\,\mu$as after 2 minutes, and has yet to hit a systematic floor. This suggests a precision of $\approx 30\,\mu$as for the full 10–15 minutes data set, assuming that no systematic limit is reached in the interim.

This level of precision is not limited to the AO guide star; similar performance is obtained on other stars in the core of M5. In Figure 1.5, we show the astrometric precision obtained on 2007 May 29 after 2 minutes for all detected stars as a function of their K_s magnitude. Precision below $100\,\mu$as is achieved on targets as faint as $K_s \approx 13$ magnitude using a narrow-band filter and 1.4 sec individual exposures. This

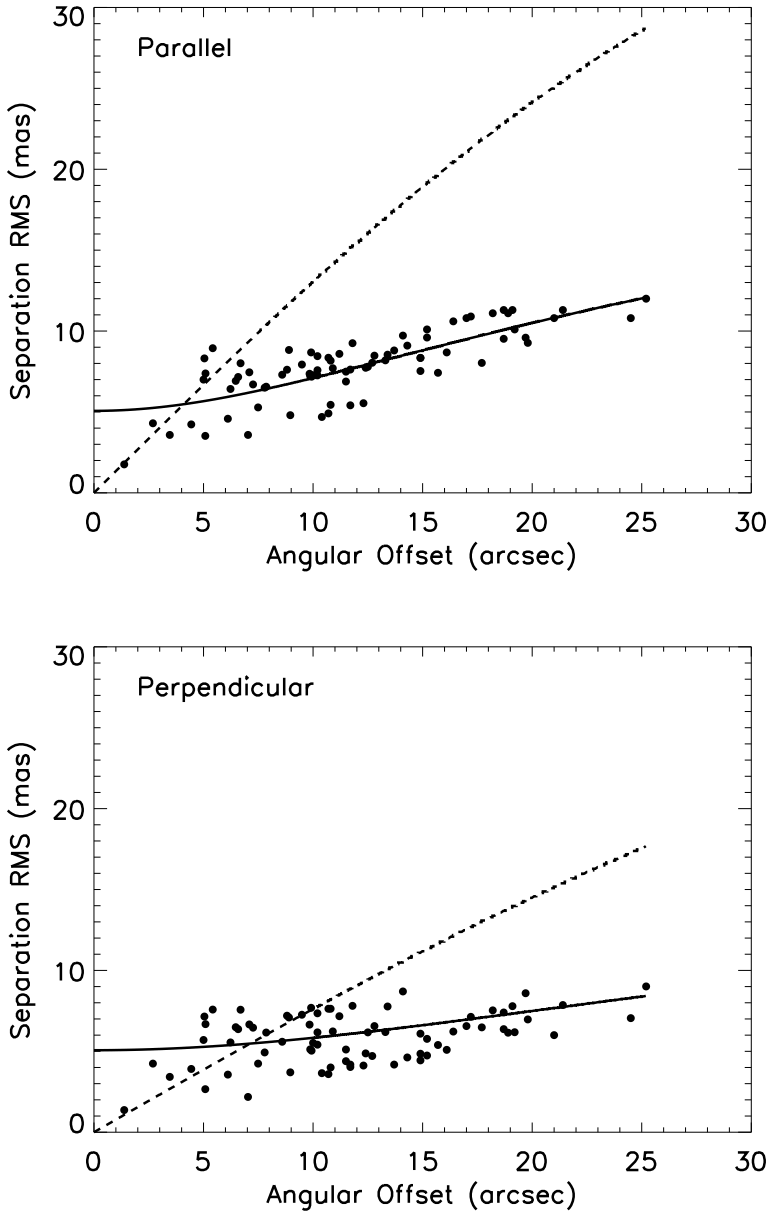

Figure 1.3 *Top:* RMS deviation in the distance between pairs of stars in the direction parallel to their separation axis on 2007 May 28 (filled circles). The jitter predicted (assuming no measurement noise) from the measured turbulence profiles and Equation 1.1 (dashed-line) is far larger than the measured jitter, indicating that some tilt jitter has been averaged away in 1.4 sec. The best-fit model (Equation 1.5), including averaged tilt jitter and measurement noise, indicates that the tilt timescale is ≈ 0.2 sec (solid line). *Bottom:* As above, but in this case the separations and predictions are for the direction perpendicular to the separation axis. The expected RMS for the perpendicular direction is lower by the expected factor as seen in Equation 1.1. Note that not all pairs include the AO guide star.

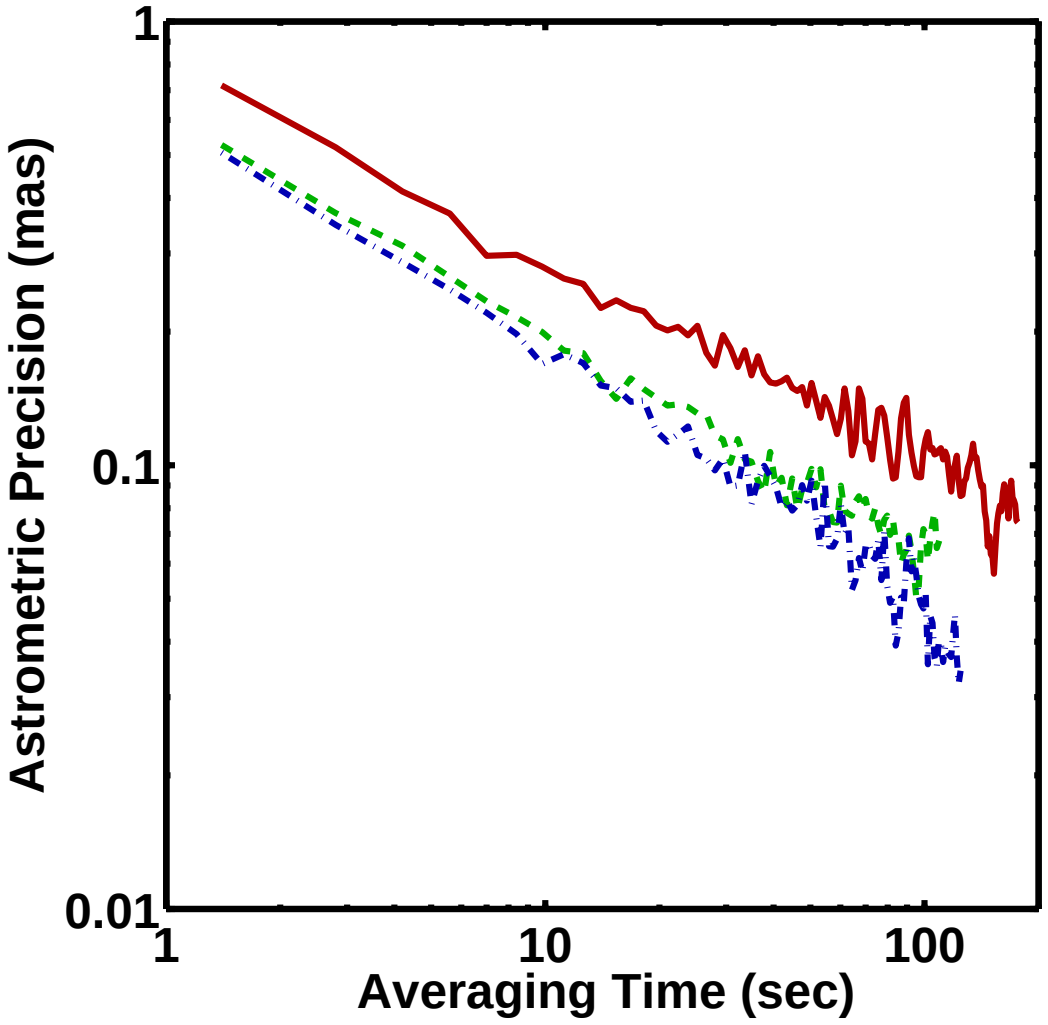

Figure 1.4 Allan deviation in the guide star position as a function of integration time for 2007 May 28 (solid curve), May 29 (dash-dotted) and July 22 (dashed). The astrometric precision scales as $t^{-0.51\pm0.08}$, and the covariance matrix and optimal weights were derived from data.

demonstrates the substantial signal-to-noise ratio benefit afforded by adaptive optics.

The astrometric precision shown in Figure 1.5, resulting from the theoretically determined covariance matrix and optimal weights, is $\approx 300\,\mu$as after 2 minutes for stars with $K_s \lesssim 13$ magnitude. This level of precision is substantially better than the performance of simpler weighting schemes, but it is a factor of 2–4 worse than using the data to calculate the covariance matrix and weighting. There are several possible reasons for this reduction in precision. The first is that we have only used estimates of the measurement noise for each star used to calculate $\mathbf{\Sigma}_{\rm meas}$. Secondly, the turbulence profile used to construct $\mathbf{\Sigma}_{\rm TJ}$ is estimated from the average $C_n^2(h)$ seen by the DIMM/MASS. This unit is located 300 m from the Hale telescope and uses Polaris to estimate the turbulence profile. As a consequence, there could be important differences between the measured atmospheric turbulence and that encountered by the light from M5. Finally, we have not attempted to capture the time variability of the turbulence, having used only the average values.

In Figure 1.6 we investigate the improvement of the AO guide star astrometry with the number of reference stars. We drew random subsets of the available grid stars, computed $\mathbf{\Sigma_d}$ from the data, calculated the optimal weights, and showed the geometric mean of the eigenvalues of $\mathbf{\Sigma_p}$. To average over the geometry of a particular draw, we repeated this process 10 times for each value of N and averaged the results. We see that the precision rapidly decreases as $N^{-0.60\pm0.03}$. This is slightly faster than our simulations predicted for 1.4 sec of integration time. However, as noted above, our simulations are meant to approximate M5, but do not capture the true distribution of stellar measurement errors (which are difficult to decouple from tilt jitter) or any evolution in atmospheric turbulence during the observation.

1.5.3 Astrometric Accuracy

The goal of astrometry is to measure the position of the target star over many epochs. Astrometrically interesting timescales range from hours to years. Clearly, the optical systems must be stable over these spans for astrometry with AO to be viable. There

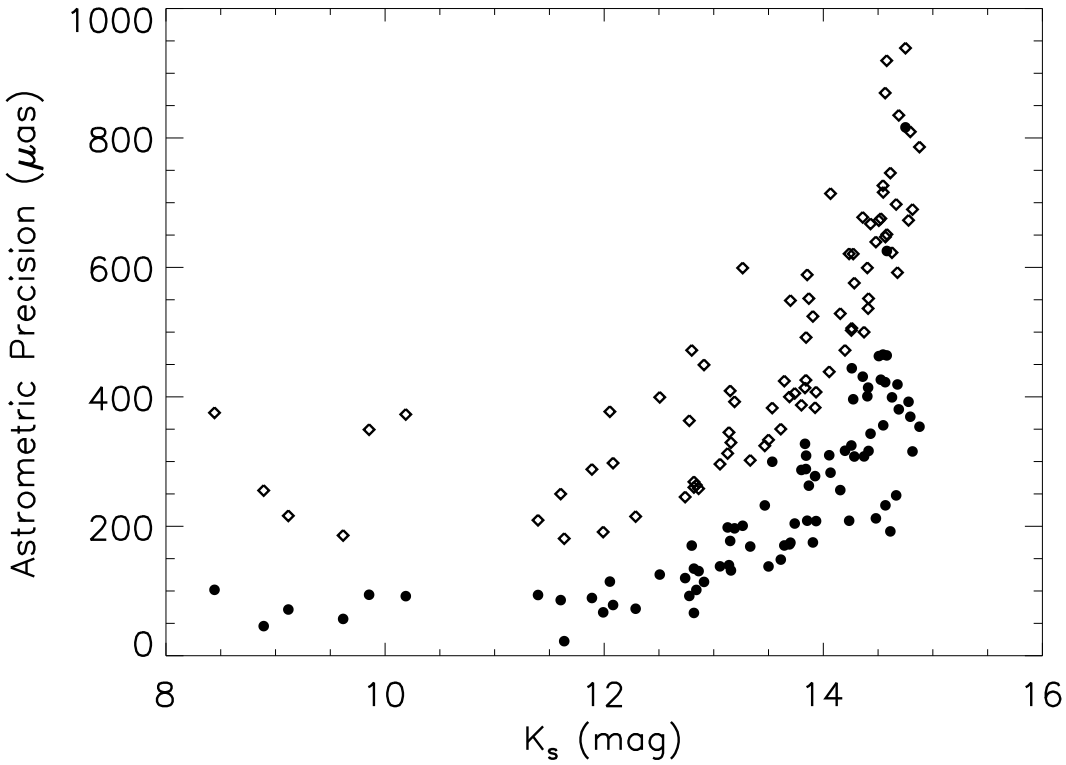

Figure 1.5 The astrometric precision (Allan deviation after 2 minutes) using the theoretical covariance matrix (open diamonds) and the covariance matrix from data (filled circles) as function of K_s magnitude for all 82 detected stars on 2007 May 29. The precision in both cases is essentially constant for $K_s \lesssim 13$ mag. However, the astrometric precision for the theoretical $\mathbf{\Sigma_d}$ is a factor of 2–4 times larger than when calculated from data.

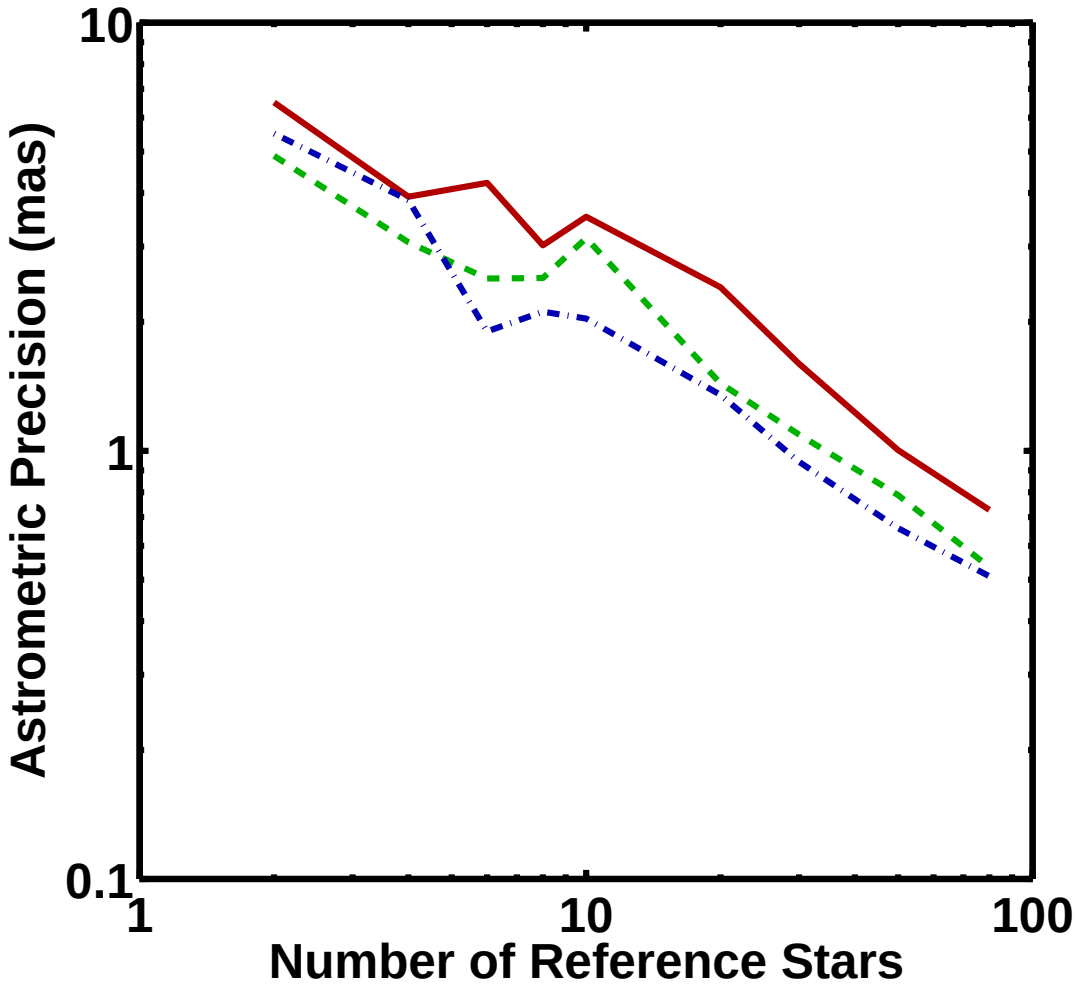

Figure 1.6 Allan deviation in 1.4 seconds for the AO guide star's position as a function of the number of reference stars on 2007 May 28 (solid curve), May 29 (dash-dotted), and July 22 (dashed). The astrometric precision scales as $N^{-0.60\pm0.03}$.

are several obstacles that could render the single-epoch precision obtained in §1.5.2 meaningless. For example, PHARO is mounted at the Cassegrain focus which results in flexure of the instrument as the telescope tracks, and undergoes warming and cooling cycles between observing periods (typically twice per month) that could cause small changes in the powered optics. Either of these facts could alter the geometric distortion and make astrometric measurements unrepeatable. In order to probe the system stability, we have designed our experiment to be as consistent as possible, and it has spanned many removal and reinstallations of PHARO over 2 months.

In order to investigate the accuracy of the M5 measurements, we first measured and corrected the small rotational ($\lesssim 0.04^\circ$) and plate scale ($\lesssim 10^{-5}$) changes between the May 29 and July 22 data and the May 28 images. We also calculated the optimal weights for a given star on all three nights, and averaged them to create one weighting matrix to use for each epoch. This is not strictly optimal, since each night has different turbulence conditions, for example, but it ensures that the scenario $\vec{p} \rightarrow \vec{p} + \vec{\epsilon}$. We see in Figure 1.7 that the measured position of the AO guide star is accurate from epoch-to-epoch at the $\approx 100\,\mu$as. The error ellipses are those estimated by continuing to extrapolate the precision found in Figure 1.4 by $1/\sqrt{t}$ to the full 10–15 minute timeseries. This is an impressive level of accuracy, but unfortunately is a factor of 3 worse than our expectation. It suggests that there is some instability, likely in the distortion, over the two months that limit the astrometric accuracy.

The other stars in M5 show a similar level of astrometric accuracy (Figure 1.8) up to $K_s \approx 13\,$mag. This limit can certainly be pushed considerably fainter within increased integration time or a larger aperture. The achievement of such high levels of astrometric performance on faint targets, given the modest time investment, short integration time, and narrow-band filters, illustrates the substantial signal-to-noise ratio gain and potential for astrometry enabled by AO.

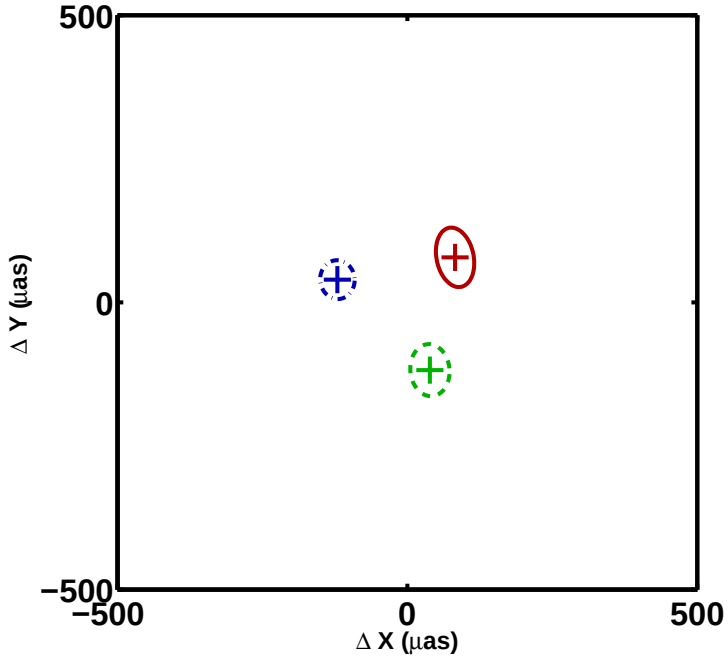

Figure 1.7 The position of the AO guide star in an arbitrary coordinate system on three dates: 2007 May 28 (solid), 2007 May 29 (dashed), and 2007 July 22 (dash-dotted; see §1.5.3). The error circles are inferred by averaging the covariance matrix measured from the data and extrapolating to the total 10–15 minute integration time as $1/\sqrt{t}$ (e.g., Figure 1.4). The positions agree at the $\lesssim 100\,\mu$as level — a factor of 2–3 larger than the expected dispersion. This discrepancy indicates that some systematic errors have occurred between epochs, most likely optical distortion.

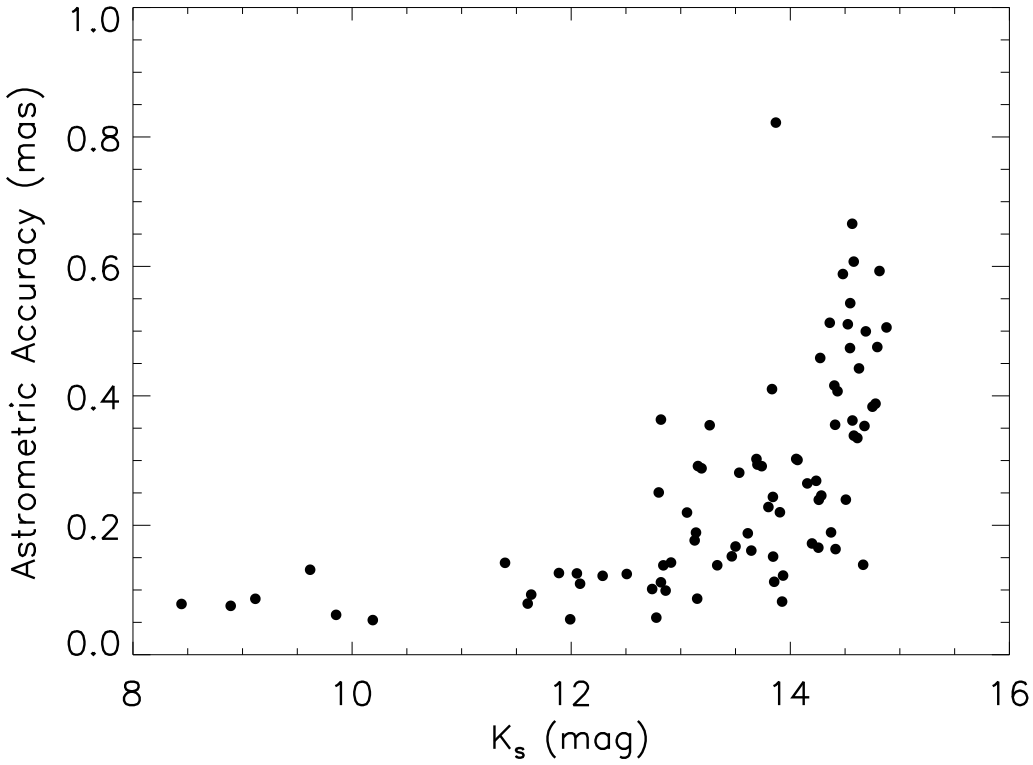

Figure 1.8 Astrometric accuracy (geometric mean of the RMS in each coordinate over the three epochs) versus K_s magnitude. The level of accuracy is $\lesssim 100\,\mu$as, and is essentially unchanged for $K_s \lesssim 13$ mag. However, this is a factor of 2–3 above our expectations from the achieved astrometric precision, suggesting a systematic limitation between epochs.

1.6 Discussion and Conclusions

We have presented a technique for performing high-precision grid astrometry using ground-based telescopes equipped with adaptive optics systems. With this technique, the effects of distortion and atmospheric dispersion that give rise to systematic errors are mitigated through the design of the experiment. Random errors arising from differential tilt jitter and measurement noise are minimized through the use of an optimal estimation scheme that accounts for the correlated noise statistics through the covariance matrix $\mathbf{\Sigma_d}$. The experimental results obtained on the Hale 200-inch Telescope have demonstrated single epoch astrometric precision of $\lesssim 100\,\mu$as in 2 minutes and multi-epoch astrometric accuracy at the same level. This level of precision is comparable to that afforded by ground-based interferometry and is better than the precision obtained in seeing-limited programs on single apertures.

The simulation of astrometric precision afforded by the optimal weighting scheme shown in Figure 1.2 illustrates that measurement noise is the dominant residual astrometric error on a 5 meter telescope for stellar fields that contain more than a few reference stars. The scaling laws for differential tilt jitter ($D^{-7/6}$) and measurement noise (D^{-2}) indicate that on larger aperture telescopes measurement noise will represent a smaller fraction of this residual error. This effect is illustrated in Figure 1.9, which shows the RMS error between pairs of stars for a range of telescope apertures and angular separations.

The values in Figure 1.9 assume that tilt jitter is resolved by sufficiently short exposures. Longer exposure times will certainly reduce the differential tilt jitter by $1/\sqrt{t}$, but the measurement noise will also be decreased by this factor (for a given stellar brightness). The implication being that if tilt jitter dominates for short exposure times, it will continue to dominate longer exposures.

In situations where fewer images are available, either due to time constraints or longer exposure times per frame, it is difficult or impossible to effectively calculate the covariance matrix directly from the data. Our results show that independent measurements of the turbulence profile, for example from a DIMM/MASS unit, are

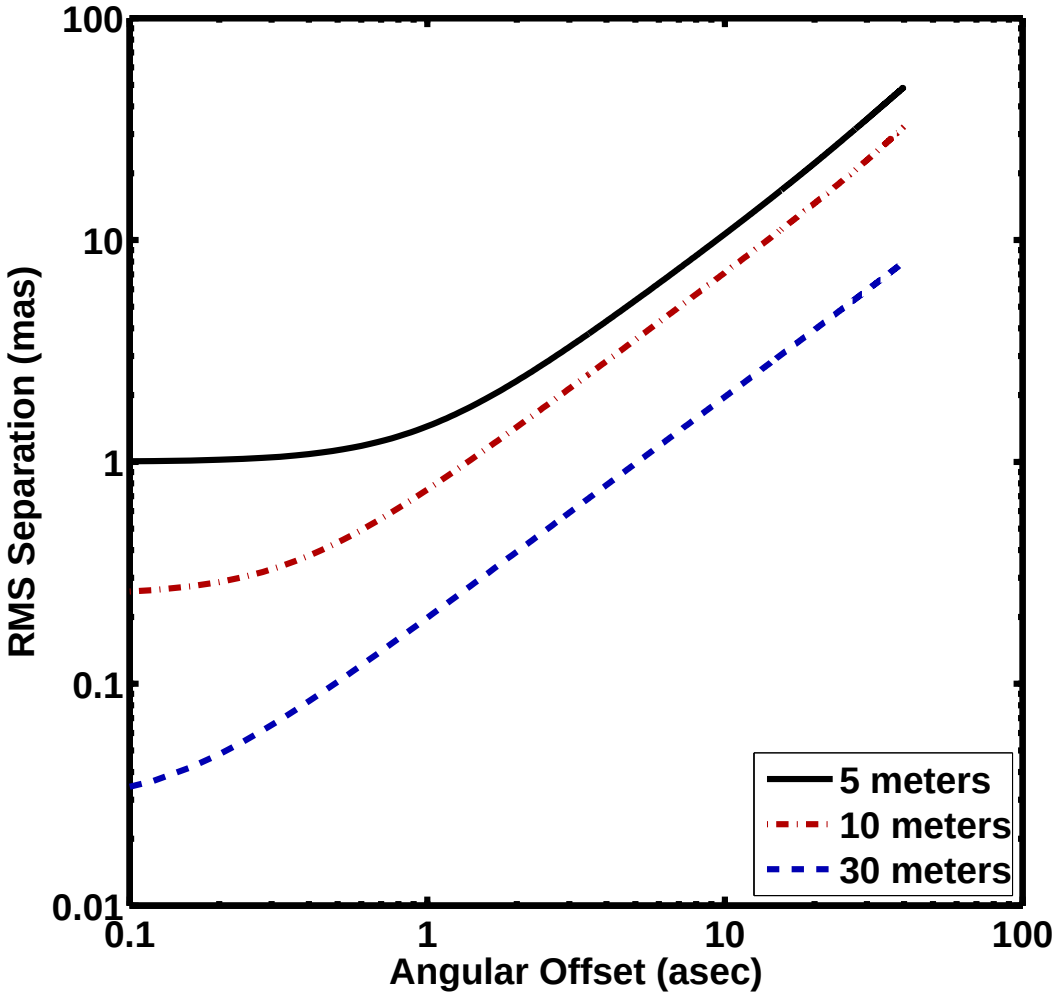

Figure 1.9 The RMS separation between a pair of stars versus angular offset and aperture diameter. We have assumed the turbulence profile on 2007 May 28, a measurement error of $1/\sqrt{2}$ mas for each star for a 5 m telescope, and included the geometric mean of each component of Equation 1.1. Relative to Palomar (solid curve), there are substantial astrometric gains to be made for larger 10 m (dash dotted) and 30 m (dashed) telescopes due to the reduction of both measurement noise (the y-intercept; $\propto D^{-2}$) and tilt jitter ($\propto D^{-7/6}$). Because measurement noise falls off more quickly with D, tilt jitter becomes the dominant source of astrometric error for large aperture telescopes.

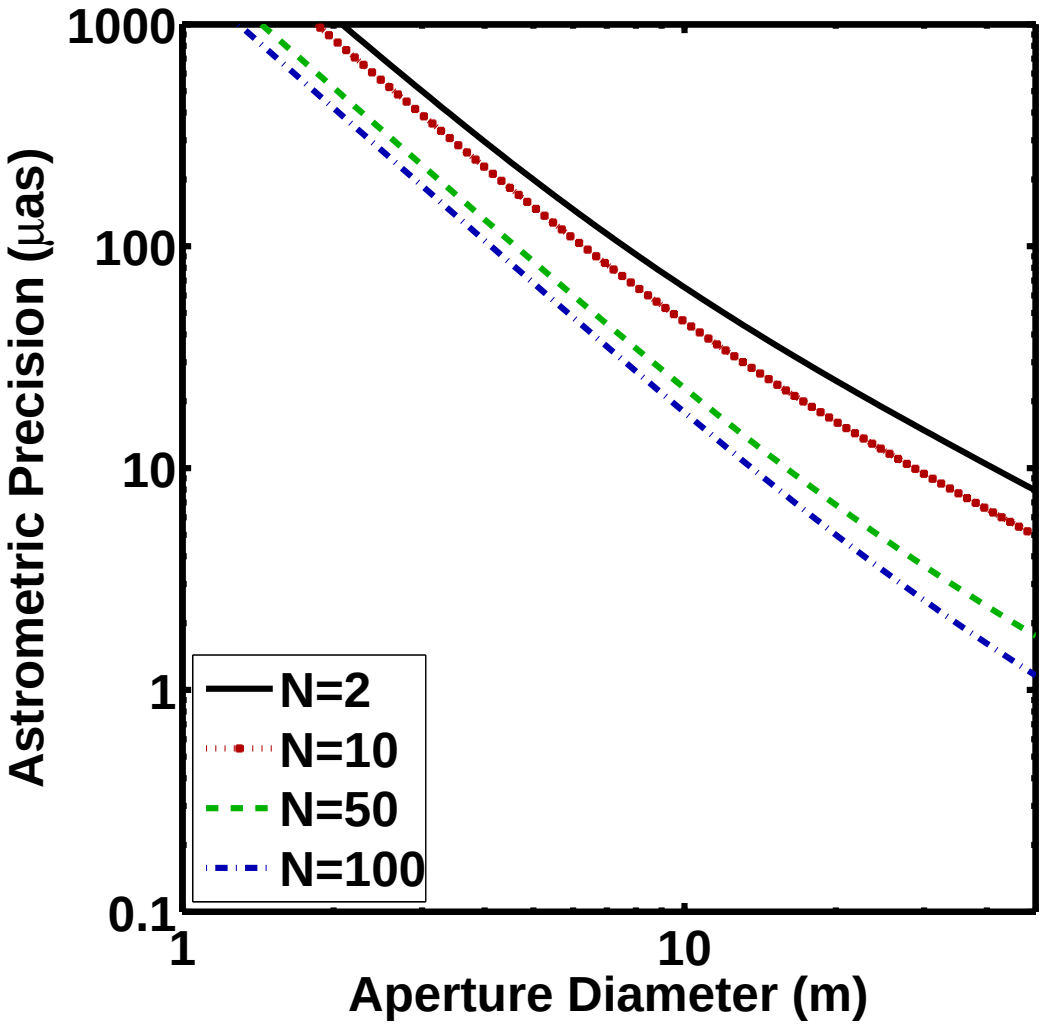

Figure 1.10 Astrometric precision as a function of aperture size and stellar density. We have used Equation 1.30 with the assumptions of the Palomar turbulence profile, a $25'' \times 25''$ field of view, the M5 brightness distribution, and photon noise limit as described in §1.6. The astrometric precision demonstrates a very favorable scaling law with aperture diameter, and suggests orders of magnitude improvement in precision may be available using large aperture, AO equipped telescopes. In practice, the level of astrometric accuracy will depend on the extent to which current and future facilities can characterize and control systematic errors.

sufficient to calculate $\mathbf{\Sigma_d}$, and result in astrometric precision within a factor of 2–4 of the levels achieved using the data itself. Thus, the astrometric applications of turbulence sensors are two-fold; they can be used to independently assess astrometric data quality and predict the AO PSF (Britton 2006).

The scaling laws presented throughout this paper indicate a substantially improved astrometric performance on large aperture telescopes equipped with adaptive optics. We have used the measured performance on M5 with the Hale Telescope combined with these scaling laws to predict the astrometric performance of a single conjugate AO system as a function of aperture diameter and number of reference stars. The relationship can be summarized using the results of simulation and data analysis as

$$\sigma^2_{\rm tot} = \sigma^2_{\rm meas} + \sigma^2_{\rm TJ} = \left(\frac{1.4\ {\rm sec}}{t}\right)\left\{\left[2\ {\rm mas}\left(\frac{2}{N}\right)^{0.3}\left(\frac{5\ {\rm m}}{D}\right)^{2}\right]^2 + \left[2\ {\rm mas}\left(\frac{2}{N}\right)^{0.7}\left(\frac{5\ {\rm m}}{D}\right)^{7/6}\right]^2\right\}. \tag{1.30}$$

This equation assumes that measurement error is dominated by photon noise ($\propto D^{-2}$) and that the other dependencies (field of view, stellar brightness distribution, turbulence profile) are identical to those for the M5 experiment.

Figure 10 shows the resulting estimates for astrometric precision as a function of aperture diameter and number of reference stars for a 2 minute exposure. These predictions demonstrate that limits to astrometric precision arising from random errors (dominated by tilt jitter) lie below 10 μas for 30 m telescopes. However, very careful characterization and control of systematic errors will be be required to achieve this level of precision in an actual experiment. The extent to which systematic errors can be eliminated will distinguish the scientific goals that can be accomplished with ground-based facilities from those that require a space-based solution.

Acknowledgements

We thank Nicholas Law, Michael Ireland, David Le Mignant, Adam Kraus, Marten van Kerkwijk, and Andrew Gould for useful discussions on astrometry. We also thank Palomar Observatory for providing support for the DIMM/MASS unit used in this study. This work has been supported by NASA, and by the National Science Foundation Science and Technology Center for Adaptive Optics, managed by the University of California at Santa Cruz under cooperative agreement No. AST - 9876783.

Chapter 2

Kinematics of Magnetars

Abstract

We present near-infrared imaging of 5 magnetars with Keck Laser Guide Star adaptive optics over a span of 3 years. The unprecedented angular resolution and sensitivity afforded by adaptive optics allow us to measure proper motions at the milliarcsecond level and characterize the space velocities of these faint objects ($K' > 19$ mag). We find that, in contrast to the theoretical predictions, magnetars are not kinematically distinct from the canonical radio pulsar population. They typically show transverse space velocities $\lesssim 600\,\mathrm{km\ s^{-1}}$, which suggests that the mechanism responsible for generating ultra-strong magnetic fields does not necessarily impart a large net momentum to the neutron star.

In particular, we identify the near-infrared counterpart to SGR 1900+14 and find that it is moving radially away from the nearby embedded massive star cluster with a transverse velocity of $553 \pm 136\,\mathrm{km\ s^{-1}}$ (assuming $d = 13\,\mathrm{kpc}$). This measurement provides the first direct evidence that SGRs are very young objects (in this case $\sim 10^3\,\mathrm{yr}$), and are directly associated with massive stars. We find that 1E 2259+586 is only marginally consistent with radial motion away from the center of CTB 109, and, if associated, it implies an age of $\approx 2.5 \times 10^4\,\mathrm{yr}$. SGR 1806−20 is shown to have a direction of motion to the southeast, away from a cluster of massive stars, with a transverse velocity of $225 \pm 97\,\mathrm{km\ s^{-1}}$. We are unable to conclusively identify the near-infrared counterpart of 1E 1841−045, but based on the content of the error

circle we constrain the magnetars proper motion to be $< 430\,\mathrm{km\ s^{-1}}$ $(3\,\sigma)$ if it is present. We discuss the implications of these direct measurements for the origins and evolution of magnetars.

2.1 Introduction

Soft γ-ray repeaters (SGRs) and anomalous X-ray pulsars are famous for their conspicuous high-energy radiation. In addition to their bright quiescent X-ray emission ($L_X \sim 10^{34}$–$10^{36}\,\mathrm{erg\,s^{-1}}$), they give rise to the most intense high-energy transients ever detected (e.g., Hurley et al. 2005). Their slow spin periods (5–12 s), lack of binary companions, faint near-infrared/optical counterparts, and the discovery of optical pulsations from one AXP suggests that neither rotation nor accretion is powering their emission. As first suggested by Paczynski (1992), it is now generally accepted that SGRs and AXPs are powered by the decay of ultra-strong magnetic fields at or above the quantum critical field limit of $B_{\mathrm{QED}} = 4 \times 10^{14}\,\mathrm{G}$ (Duncan 2000).

How SGRs and AXPs (dubbed 'magnetars') have acquired such incredible magnetic field strengths and their relation to the general neutron star ($B \sim 10^{12}\,\mathrm{G}$) population remains unclear. Some authors have argued that the core collapse process distinguishes magnetars from canonical radio pulsars (Duncan & Thompson 1992; Thompson & Duncan 1993). Strong convection in rapidly spinning ($P \sim 1\,\mathrm{ms}$) proto-neutron star cores is thought to enhance the magnetic field via dynamo action during magnetar formation. Indeed, multidimensional numerical simulations have confirmed that vigorous convection can occur (Dessart et al. 2006). Duncan & Thompson (1992) suggest that various magnetic effects should cause asymmetries in the isotropy of neutrino emission. Given the ubiquity of neutrinos, even a small momentum asymmetry ($\delta p/p \sim 0.03$) will manifest itself as a space velocity $\gtrsim 1000\,\mathrm{km\ s^{-1}}$in contrast to the 200–300 $\mathrm{km\ s^{-1}}$ velocities of radio pulsars (Hobbs et al. 2005).

Observationally this expectation arises from the large offsets measured to nearby putative supernova remnant and massive star cluster associations that would require large space motions (e.g., Helfand & Long 1979). These associations have also lead

to the suggestion that magnetars are young ($\lesssim 10^4\,\mathrm{yr}$) and born from more massive progenitors than normal neutron stars ($\sim$ 30–40 $\mathrm{M}_\odot$; Gaensler et al. 2005c; Muno et al. 2006), in a territory previously reserved for black holes. Scrutiny has called into question a number of these associations as coincidence. Gaensler et al. (2001) searched for and reviewed magnetar associations and suggested that AXPs are young and low velocity ($\lesssim 500\,\mathrm{km\ s^{-1}}$) and called into question the connection between SGRs and AXPs.

It is clear that only direct measurements of magnetar proper motions will settle questions of their space velocity, age, and birth site. Unfortunately, such measurements have proved elusive due to their faintness at lower energy wavebands. To date, one magnetar has a measured proper motion. XTE J1810−197 was discovered to have bright transient radio emission (Camilo et al. 2006), which allowed Helfand et al. (2007) to measure a transverse velocity of $212 \pm 35\,\mathrm{km\ s^{-1}}$ using the Very Long Baseline Array.

As opposed to the radio band, the majority of magnetars have confirmed near-infrared counterparts. As such, ground-based adaptive optics (AO) offer an attractive avenue for measuring the proper motions of magnetars. AO corrects atmospheric turbulence above the telescope, thereby improving the telescope's angular resolution to near the diffraction limit. Near diffraction-limit imaging improves the resolution and increases the signal-to-noise ratio, thus substantially improving astrometric precision, mitigating confusion in the Galactic plane, and AO operation in the near-infrared reduces the detrimental effects of interstellar extinction.

Here we present the identification of the infrared counterpart to SGR 1900+14, a measurement of its proper motion along with kinematic studies of four other magnetars. We will review the salient features and history of each of the five magnetars in §2.2. We describe the observations and data reduction methodology in §2.3. The results of the analysis for each source are presented in §2.4, and we will discuss the implications of these measurements in §2.5.

2.2 Properties of Individual Sources

Magnetars are a very-well studied class of objects (see Woods & Thompson 2006 for a review), and each one has a storied history. Here will summarize the relevant state of our knowledge and the outstanding problems that exist for the 2 SGRs and 3 AXPs in our sample.

2.2.1 SGR 1900+14

SGR 1900+14 was identified in the late 1970s as a source of sporadic high-energy emission, and had a suggested association with the 12′ diameter supernova remnant (SNR) G042.8+00.6 located 17′ to the southeast (Mazets et al. 1979; Kouveliotou et al. 1993; Vasisht et al. 1994). On 1998 August 27, a giant γ-ray flare was detected from the SGR, and the high energy localization allowed the exact position to be pinpointed upon the discovery of a fading radio source (Hurley et al. 1999a; Frail et al. 1999). Subsequent high energy follow-up confirmed the 5.16 s periodicity seen in the giant flare and the column density from the X-ray spectrum suggested a distance of 5 kpc (Hurley et al. 1999b).

Multiwavelength studies of the region have placed strong constraints on the magnetar emission, and also led to the identification of a nearby massive star cluster previously hidden by two bright M5 supergiants (Kaplan et al. 2002a; Vrba et al. 2000). The cluster is 12″ due east of SGR 1900+14, and has an estimated distance of 12–15 kpc if associated with the M5 supergiants.

The massive star cluster and supernova remnant associations have widely disparate interpretations. If SGR 1900+14 originated in the massive cluster, it would require only a velocity of $\sim 400\,\mathrm{km\ s^{-1}}$ depending on the distance and assuming a young age. However, if G 042.8+00.6 is the birth site, it implies either a very large velocity or a very old age. The association with the SNR is further complicated by the discovery of the young pulsar PSR J1907+0918 only 2′ from SGR 1900+14 that could also claim one of the above associations (Lorimer & Xilouris 2000).

Recent high-resolution observations have independently suggested a tentative near-

infrared counterpart to SGR 1900+14 based on its location in the error circle and marginal ($\lesssim 3\sigma$) variability (Testa et al. 2008). We confirm that this identification is indeed correct.

2.2.2 SGR 1806−20

SGR 1806−20 is found near a very massive embedded star cluster containing a number of Wolf-Rayet stars and LBV 1806−20, which may be the most massive star in the galaxy (Eikenberry et al. 2004). In the mid-1990s it was suggested that the LBV and its surrounding radio nebula were associated with SGR 1806−20 (Kulkarni et al. 1995; van Kerkwijk et al. 1995), but the precise localization of Kaplan et al. (2002a) showed the two are significantly separated. However, the association of SGR 1806−20 with the nearby massive stars remained and allowed the first distance estimate of $15^{+1.8}_{-1.3}$ kpc with a strict lower limit of 5.7 kpc from ammonia absorption in the LBV.

This picture was revised substantially when on 2004 Dec 27 the SGR emitted the most intense high-energy transient ever detected (Hurley et al. 2005). The blast saturated nearly every detector in space, and left a long lived radio afterglow (Cameron et al. 2005; Gaensler et al. 2005a), which confirmed the precise localization of Kaplan et al. (2002a). It also lead to the first direct estimate of the distance to SGR 1806−20 via an HI absorption spectrum that constrained the allowed distance to be 6.5–9.8 kpc (Chapter 3). This distance estimate has proven to be controversial (e.g., McClure-Griffiths & Gaensler 2005); however, evidence is mounting that a nearer distance of $8.7^{+1.8}_{-1.5}$ kpc is indeed correct based on spectroscopy of the cluster and a dust scattering halo from SGR 1806−20 (Bibby et al. 2008; Goad et al. 2006).

Shortly after the giant flare, Israel et al. (2005) announced the discovery of the near-infrared counterpart to SGR 1806−20 based on astrometry and brightening leading up to the giant flare. This brightening and post-flare fading (see below) of the counterpart is correlated with the variable X-ray emission (Rea et al. 2005).

2.2.3 AXP 4U 0142+61

Israel et al. (1994) discovered that 4U 0142+61 was an 8.7 s pulsar. It is the nearest, brightest magnetar in the near-infrared/optical wavelengths, and as a consequence is the most studied magnetar outside the high-energy band. 4U 0142+61 was the first to have an identified counterpart due to its peculiar colors (Hulleman et al. 2000). This allowed Kern & Martin (2002) to use a novel device to measure optical pulsations at the pulsar period, providing strong evidence of a magnetospheric origin of the emission as opposed to X-ray reprocessing in a putative accretion disk. A small dusty disk was discovered, via a mid-IR excess, indicating a fallback from the supernova, but it is insufficient to power the observed X-ray emission (Wang et al. 2006).

It has no known associations despite the fact that the region has been searched to the limits of the faintest SNR known (Gaensler et al. 2001). As such, the best distance estimate comes from a novel technique employed by Durant & van Kerkwijk (2006), who use the column density as derived from the X-ray spectra in combination with red clump stars along the line of sight (to ascertain the run of reddening), who estimate a distance of 3.6 ± 0.4 kpc. This puts it inside or just behind the Perseus spiral arm.

2.2.4 AXP 1E 2259+586

1E 2259+586 was identified as pulsar near the center of the young ($\approx 10^4$ yr) SNR CTB 109 (Fahlman & Gregory 1981). It is located less than $4'$ from the center of the $14'$ diameter shell, suggesting $\approx 10^{-4}$ chance of coincidence (Green 1989; Rho & Petre 1997; Gaensler et al. 2001). It is an important object since it solidified the connection between SGRs and AXPs after it exhibited SGR-like bursts in 2002 (Kaspi et al. 2003). Tam et al. (2004) used the identified near-infrared counterpart to show the correlation between the high-energy emission and that of longer wavelengths (Hulleman et al. 2001).

The red clump method suggests that 1E 2259+586 lies just inside the outer spiral arm at a distance of 7.5 ± 1.0 kpc, but distance estimates for CTB 109 have been

as close as 3.5 kpc (Kothes et al. 2002). These distance and age estimates, with the measured offset, have lead to the prediction that the proper motion of 1E 2259+586 is $\lesssim 500\,\mathrm{km\ s^{-1}}$.

2.2.5 AXP 1E 1841−045

1E 1841−045 is the 11.8 s pulsating central source of SNR Kes 73 (Vasisht & Gotthelf 1997). Kes 73 is a limb-brightened, compact ($\approx 4'$ diameter), young ($\approx 2\,\mathrm{kyr}$) supernova remnant in the Galactic Plane. It is suggested to have a massive ($> 8\,M_\odot$) progenitor and could be in the transition between the free expansion and Sedov phase (Sanbonmatsu & Helfand 1992; Gotthelf & Vasisht 1997). The AXP's proximity to the center of the remnant ($< 30''$) is consistent with the young age, and a modest proper motion ($\lesssim 500\,\mathrm{km/s}$; Vasisht & Gotthelf 1997; Gaensler et al. 2001).

Despite deep near-infrared searches, no counterpart has been conclusively identified (Durant 2005; Testa et al. 2008). The best estimate of the source distance comes from the SNR distance estimates of 6–7.5 kpc, which is consistent with the limit of $> 5\,\mathrm{kpc}$ from the red clump method (Sanbonmatsu & Helfand 1992; Durant & van Kerkwijk 2006).

2.3 Observations and Data Reduction

We observed a total of five magnetars over three years using Laser Guide Star Adaptive Optics (LGS-AO; Wizinowich et al. 2006b; van Dam et al. 2006) and the Near-Infrared Camera 2 (NIRC2) on the Keck II telescope. The fields were imaged with wide and narrow cameras (depending on their stellar density) which provided $\approx 40'' \times 40''$ and $\approx 10'' \times 10''$ fields of view with $\approx 0.04''$and $\approx 0.01''$pixel scales, respectively. A summary of the observations can be found in Table 2.1. We used varying exposure times and on-chip additions to achieve 60 s integrations without saturation in a 4-point dither pattern. The typical full-width at half maximum was 50–80 milliarcseconds (mas) depending on conditions with marked improvement after the upgrade of the wavefront controller in the beginning of 2007.

Table 2.1. Summary of Keck LGS-AO Observations

Object	Date (UT)	Mid-exposure (UT)	Band	Camera	Integration Time (sec)	Brightness (mag)
SGR 1806−20	2005 Sep 26	06:20	K'	N	600	≈ 22
	2006 Jul 03	10:19	K'	N	2820	22.1 ± 0.2
	2006 Aug 17	07:34	K'	N	1800	≈ 22
	2007 May 22	11:55	K'	N	1080	22.2 ± 0.4
	2007 Jun 11	10:09	K'	N	2040	22.1 ± 0.4
	2007 Jul 16	08:59	K'	N	3060	21.5 ± 0.2
	2007 Aug 6	08:31	K'	N	2700	21.3 ± 0.2
SGR 1900+14	2005 Apr 30	13:48	K'	N	1300	See Table 2.2
	2006 Aug 17	10:56	K'	N	1140	
	2007 May 22	13:30	K'	N	1560	
	2007 Jun 11	13:29	K'	N	1200	
	2007 Aug 6	11:16	K'	N	1860	
	2007 Nov 03	05:45	K'	N	1320	
4U 0142+61	2005 Sep 26	14:15	K'	W	1440	19.88 ± 0.09
	2006 Aug 17	14:44	K'	W	2100	19.74 ± 0.09
	2006 Oct 13	13:33	K'	W	1560	19.74 ± 0.09
	2006 Dec 20	07:37	K'	W	1860	19.61 ± 0.09
	2007 Aug 6	15:01	K'	W	720	19.58 ± 0.09
1E 1841−045	2005 Sep 26	07:06	K'	W	720	see Table 2.3
	2005 Sep 26	07:17	K'	N	780	
	2006 Jul 04	11:38	K'	N	1560	
	2006 Aug 17	09:53	K'	N	720	
	2007 May 22	11:07	K'	N	1680	
	2007 Jun 11	11:54	K'	N	2340	
	2007 Aug 6	10:11	K'	N	2460	
	2008 May 21	14:43	K'	N	1680	
1E 2259+586	2005 Aug 10	10:32	K'	W	780	21.5 ± 0.3
	2005 Sep 26	11:11	K'	W	1320	21.3 ± 0.3
	2006 Jul 03	13:36	K'	W	1140	21.5 ± 0.3
	2005 Jul 04	13:39	K'	W	1080	21.4 ± 0.3
	2006 Aug 17	13:17	K'	W	1800	21.3 ± 0.3
	2006 Oct 13	7:43	K'	W	960	21.1 ± 0.3
	2006 Dec 20	6:02	K'	W	1920	21.3 ± 0.3

Each frame was dark subtracted, flat-fielded, background subtracted, and repaired for bad pixels using custom PyRAF software[1]. We then performed a second round of sky subtraction using a median combination of similarly processed frames of a nearby field or the target field itself. All processed frames were corrected for optical distortion using the solution derived in Appendix A.[2]

2.3.1 Absolute Photometry and Astrometry

We performed photometry of the sources in each image using PSF-fitting photometry as implemented by DAOPHOT in PyRAF. The zeropoints were determined with nearby stars found in the 2MASS catalog or using published photometry of the field (Cutri et al. 2003a). Color corrections between the K_s and K' bands were negligible for the precision we sought here. Where possible, we used only stars near ($\lesssim 10''$) the SGR or AXP to ensure that PSF variations due to anisoplanatism would be minimized.

We measured the positions of stars using DAOPHOT PSF-fitting. We derived the PSF using the brightest stars in the field, and assumed that it was constant over the field. As for absolute photometry, we used the 2MASS catalog or published studies for absolute astrometry. The positional measurements relative to the International Celestial Reference Frame (ICRF) were typically dominated by the catalog systematic errors (typically 0.1-0.2$''$). These errors were added in quadrature to obtain the total astrometric accuracy. The details of the absolute astrometry and photometry for each source will be enumerated below (see §2.4).

2.3.2 Relative Astrometry Measurement Model

To compute the relative astrometry of stars in each field, we will build on the framework presented in Chapter 1. The faintness of our targets and long exposure times render differential atmospheric tilt jitter negligible, and thus our covariance matrix

[1]PyRAF is a product of Space Telescope Science Institute, which is operated by AURA for NASA.

[2]This solution was also made available to the community at http://www2.keck.hawaii.edu/inst/nirc2/forReDoc/post_observing/dewarp/

will be modified. In addition, we are unable to estimate the covariance matrix from data since our magnetars are only detected in the final combined image, and thus we lack a sufficient numbers of images to calculate statistics. The covariance matrix was constructed theoretically using geometry of the field and a typical turbulence profile from Mauna Kea.

Due to concerns over the residual distortion for stars far from the target in our 2005 and 2006 that were substantially dithered, we have moved to a distance weighted measurement scheme to downweight stars far from the target for improved accuracy. We calculated weights using $w_{xx,ij} = w_{yy,ij} = 1/\sigma_{ij}^2$, where $\sigma_{ij}^2 = \sigma_m^2 + \sigma_{\rm TJ}^2\theta^2$, $\sigma_{\rm TJ}^2$ is the geometric mean of the parallel and perpendicular components of Equation 1.5, and θ is the angular offset between the target (i) and the reference star (j).

The globular cluster M5 was chosen for the experiment in Chapter 1 since it represented a fixed grid to high accuracy. For general observations of the Galactic Plane we must account for the fact that all the reference stars are moving with proper motions significant on the angular scales probed here, so the grid is slowly changing over time. Thus it is necessary to incorporate the measurement model into a least-squares framework capable of simultaneously solving for the best-fit proper motions of all the stars in the field.

Measurement of the offset between the target star and each of the N reference stars results in a set of vectors at each of the E epochs. For example, the differential offsets between star 0 and the grid of reference stars at epoch k will be written as a single column vector

$$\mathbf{d}_{0k} = [x_{01}, \cdots, x_{0N}, y_{01}, \cdots, y_{0N}]^{\rm T}. \tag{2.1}$$

Here $x_{ij} \equiv x_j - x_i$ is the distance between the jth reference star's x-coordinate and the ith target star's x-coordinate, and likewise for y. The goal of differential astrometry is to use $\mathbf{d}$ to determine the position of the target star with respect to the reference grid of stars at each epoch.

To obtain the position of target star i at epoch k, we use the weights computed

as mentioned above to evaluate

$$\vec{p}_{ik} = \mathbf{W}_i \mathbf{d}_{ik}, \tag{2.2}$$

where, for example, $\mathbf{W}_0$ is

$$\mathbf{W}_0 = \begin{bmatrix} w_{xx,01} & \cdots & w_{xx,0N} & w_{xy,01} & \cdots & w_{xy,0N} \\ w_{yx,01} & \cdots & w_{yx,0N} & w_{yy,01} & \cdots & w_{yy,0N} \end{bmatrix}. \tag{2.3}$$

We have used the notation $w_{xy,0i}$ to denote the weighting of the offset from the target star to star i in the y direction which is used to determine the x component of the target's position, $\vec{p}$.

If we assume a simple linear model for the stellar motion, then the differential offsets should be the column vector

$$\mathbf{d}_0 = \begin{bmatrix} z_{x,1} + v_{x,1}t - (z_{x,0} + v_{x,0}t) \\ \vdots \\ z_{x,N} + v_{x,N}t - (z_{x,0} + v_{x,0}t) \\ z_{y,1} + v_{y,1}t - (z_{y,0} + v_{y,0}t) \\ \vdots \\ z_{y,N} + v_{y,N}t - (z_{y,0} + v_{y,0}t) \end{bmatrix}, \tag{2.4}$$

and we can write the unknown quantities as

$$\mathbf{b} = [z_{x,0}, \cdots, z_{x,N}, v_{x,0}, \cdots, v_{x,N}, z_{y,0}, \cdots, z_{y,N}, v_{y,0}, \cdots, v_{y,N}]^{\mathrm{T}}. \tag{2.5}$$

The best determination of the stellar motions is the solution $\hat{\mathbf{b}}$ that minimizes the residuals $\mathbf{e}$ from

$$\mathbf{p} = \mathbf{X}\mathbf{b} + \mathbf{e}, \tag{2.6}$$

in a least squares sense. Here all the positional measurements are incorporated into

$$\mathbf{p} = [p_{x,00}, p_{y,00}, \cdots, p_{x,0E}, p_{y,0E}, \cdots, p_{x,N0}, p_{y,N0}, \cdots, p_{x,NE}, p_{y,NE}], \tag{2.7}$$

and the design matrix can be identified by performing the multiplication in Equation 2.4. Doing so yields

$$\mathbf{X} = \begin{bmatrix}
-\sum_k w_{xx,0k} & w_{xx,01} & \cdots & w_{xx,0N} & -t\sum_k w_{xx,00} & tw_{xx,01} & \cdots & tw_{xx,0N} & \\
 & -\sum_k w_{xy,00} & w_{xy,01} & \cdots & w_{xy,0N} & -t\sum_k w_{xy,00} & tw_{xy,01} & \cdots & tw_{xy,0N} \\
-\sum_k w_{yx,00} & w_{yx,01} & \cdots & w_{yx,0N} & -t\sum_k w_{yx,00} & tw_{yx,01} & \cdots & tw_{yx,0N} & \\
 & -\sum_k w_{yy,00} & w_{yy,01} & \cdots & w_{yy,0N} & -t\sum_k w_{yy,00} & tw_{yy,01} & \cdots & tw_{yy,0N} \\
\vdots & & & & & & & & \\
w_{xx,N1} & \cdots & w_{xx,NN-1} & -\sum_k w_{xx,Nk} & tw_{xx,N1} & \cdots & tw_{xx,NN-1} & -\sum_k tw_{xx,Nk} & \\
 & w_{xy,N1} & \cdots & w_{xy,NN-1} & -\sum_k w_{xy,Nk} & tw_{xy,N1} & \cdots & tw_{xy,NN-1} & -\sum_k tw_{xy,Nk} \\
w_{yx,N1} & \cdots & w_{yx,NN-1} & -\sum_k w_{yx,Nk} & tw_{yx,N1} & \cdots & tw_{yx,NN-1} & -\sum_k tw_{yx,Nk} & \\
 & w_{yy,N1} & \cdots & w_{yy,NN-1} & -\sum_k w_{yy,Nk} & tw_{yy,N1} & \cdots & tw_{yy,NN-1} & -\sum_k tw_{yy,Nk}
\end{bmatrix} \tag{2.8}$$

The least squares solution to this problem is

$$\hat{\mathbf{b}} = (\mathbf{X}^{\mathrm{T}}\mathbf{X})^{-1}\mathbf{X}^{\mathrm{T}}\mathbf{p}, \tag{2.9}$$

which we solve using singular value decomposition since the rows of $\mathbf{X}$ are nearly linearly dependent. The errors for each quantity b_i are then the diagonal elements of $\sigma(\mathbf{X}^{\mathrm{T}}\mathbf{X})^{-1}$ where

$$\sigma = \sqrt{\hat{\mathbf{e}}^{\mathrm{T}}\hat{\mathbf{e}}/(2NE - 4N)}. \tag{2.10}$$

As in Chapter 1, we use the same weights for each epoch for each target. We also take the additional step of correcting plate scale changes and rotations between epochs before applying the measurement model.

The final step in calculating the proper motions is to correct for effects not captured in the above model. The framework laid out in this section implicitly assumes that there is no net velocity of reference field, and we have no ability to capture that information without knowing the absolute motion of a star in the field (e.g., an extragalactic source). However, the Sun's peculiar motion and the differential rotation of the galaxy ensure a measurable velocity dispersion and some net motion of the field. To correct this effect, we construct a model assuming the Sun has motion $(U, V, W) = (10.0, 5.2, 7.2)\,\mathrm{km\ s^{-1}}$ (Dehnen & Binney 1998) and that the Galaxy is rotating with a constant circular speed outside of $R = 2\,\mathrm{kpc}$ of $220\,\mathrm{km\ s^{-1}}$, decreasing linearly inside of that radius, and that the distance to the Sun is $R_0 = 8.0\,\mathrm{kpc}$. We then apply an offset to the observed proper motions to fit them to the expected proper motion distribution along a particular line of sight. This gives us the magnitude and direction of the stars in right ascension and declination. Finally, using an estimate of the distance to the source we correct for the Solar and Galactic rotation to obtain the velocity relative to the local standard of rest (LSR).

2.4 Analysis and Results

2.4.1 SGR 1900+14

The position of SGR 1900+14 was measured to be $\alpha_{\rm J2000} = 19^{\rm h}07^{\rm m}14.33^{\rm s}$, $\delta_{\rm J2000} = +09^\circ19'20.1''$ with an uncertainty of $0.15''$ in each coordinate after the giant flare on 1998 August 27 (Frail et al. 1999). To place this position on our Keck images, we determined the best astrometric solution using 5 stars reported in Kaplan et al. (2002a) and our data from 2006 Aug 17. The resulting residuals were negligible in comparison to the $0.2''$ accuracy of the USNO-A2.0 catalog relative to the ICRF. When combined with the radio positional uncertainty, this yields a $0.8''$ error circle at 99% confidence. A finder chart of the field with the astrometric error circle can be found in Figure 2.1 with the corresponding absolute astrometry of sources in Table 2.2.

We see two additional sources in the error circle as compared to Kaplan et al. (2002a): sources H and J. We note that source H has been tentatively suggested as the counterpart independently by Testa et al. (2008) based on its astrometric location and $\lesssim 3$-σ variability using VLT. The resolution and performance of Keck LGS-AO allows us to perform accurate PSF-fitting photometry. We determine the zeropoint of each frame using the photometry of star B of Kaplan et al. (2002a). The uncertainty in this determination dominates the random errors. We assume the color correction from K_s to K' is negligible.

Both source H and J show significant variability over the two years of observations. Source H shows a secular brightening by nearly a magnitude during this time, which is well-correlated with the increased activity of SGR 1900+14 in 2006 (Israel et al. 2008). Source J also shows rapid variability of up to a magnitude. However, a number of facts lead us to disfavor source J as the counterpart to SGR 1900+14. The first is that in our deepest images, source J appears extended, and thus may not be a stellar source, in which case PSF-fitting photometry is unreliable. The presence of the nearby source C could lead to an underestimate of the photometric errors, especially prior to the wavefront controller upgrade when it was at our detection limits. Most importantly, the proper motion of source H (see below) suggests that it is very likely

the counterpart to SGR 1900+14.

We computed the proper motion of all of the stars in the field using the measurement model presented in §2.3.2 in Figure 2.2. The scatter of the field star proper motions is < 2 mas in each axis, which is consistent with the small amount of differential rotation seen along this line of sight. There are two outlying stars with significant proper motions. The first is far from the radio error circle, and the second is source H. The measured proper motion after correction for the field's bulk motion is $\mu_\alpha = -10.9 \pm 0.8\,\mathrm{mas\,yr^{-1}}$,$\mu_\delta = -4.4 \pm 0.8\,\mathrm{mas\,yr^{-1}}$.

As mentioned above, there is a relatively large uncertainty in the distance to this source. Estimates of the distance from N_H suggest a 5 kpc distance. Alternatively, if SGR 1900+14 is associated with the nearby massive star cluster, and those cluster members are associated with the M5 supergiants, this suggests a distance of 12-15 kpc. Luckily, along this line of sight the correction for the Earth's peculiar motion and galactic rotation are roughly the same (within 0.5 mas). Making this correction implies a transverse space velocity of $205 \pm 50\,\mathrm{km\ s^{-1}}$ or $553 \pm 136\,\mathrm{km\ s^{-1}}$ for 5 and 13.5 kpc, respectively. The errors here include uncertainties in each distance estimate, the measurement errors, and errors in the LSR correction (implicitly depending on distance). After this correction the direction of motion is 243 $\pm$ 10 degrees (east of north). This is consistent with radial motion from the nearby massive star cluster, and is nearly orthogonal to the direction of the supernova remnant.

The velocity of $550\,\mathrm{km\ s^{-1}}$ at the far distance is larger than the typical neutron star. However, it seems hard to reconcile the farther distance with the modest column density. Indeed, Vrba et al. (2000) do not rule out the possibility that the cluster contains massive main sequence stars at the nearer distance.

The measured angular offset between the SGR and the center of the massive star cluster is $12''$, which implies an extremely young age of 1300 years. This represents the first direct evidence of the hypothesis that SGRs are born from more massive stars than normal neutron stars and are very young objects.

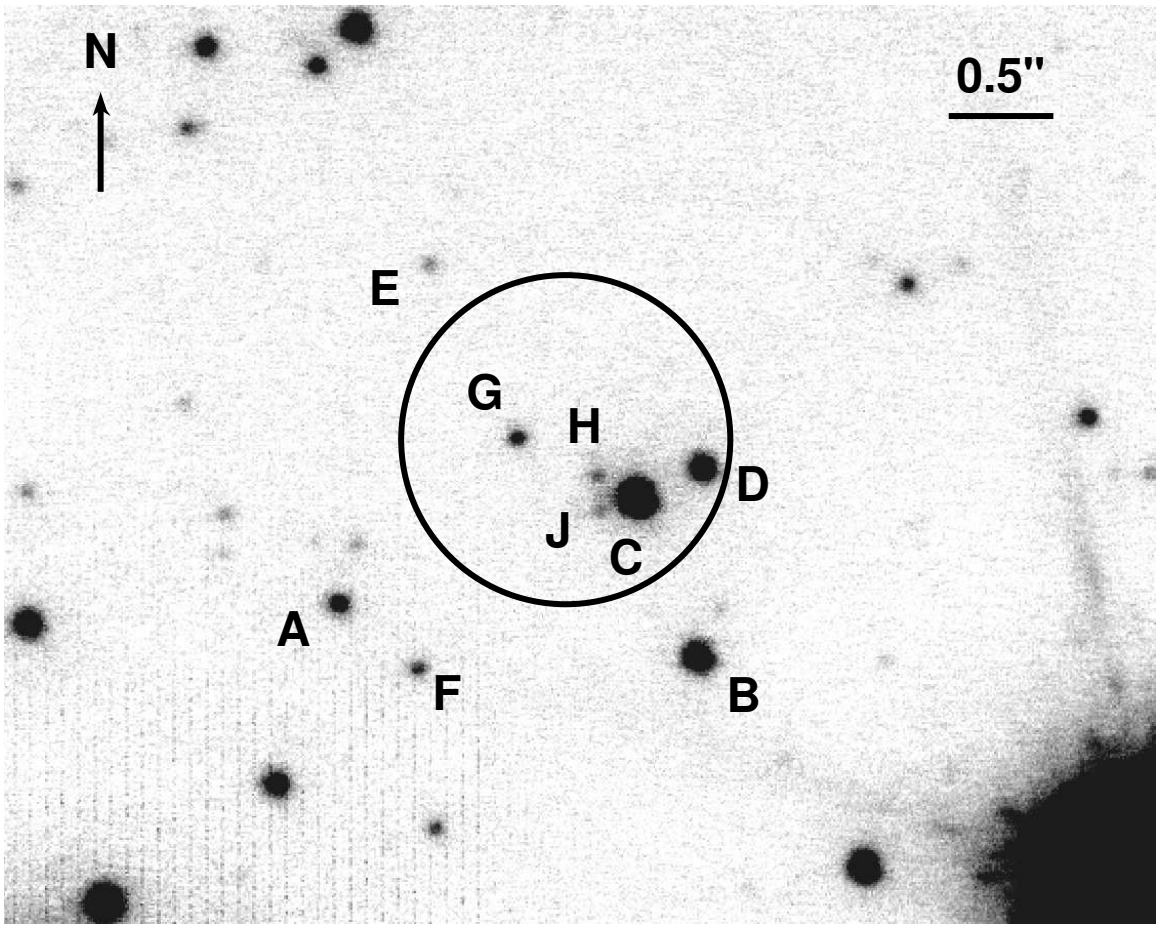

Figure 2.1 Image of the field of SGR 1900+14. The 99% confidence position is marked by the circle, and the sources are labeled as in Kaplan et al. (2002a). In the image, north is up and east is to the left. The massive star cluster identified is $\approx 12''$ due east of this image, corresponding to the origin of the proper motion of source H.

Table 2.2. Astrometry and photometry of stars in and around the error circle of SGR 1900+14

Source	RA 19^h17^m	Dec $+09°19^m$	K' (mag) MJD 53490.6	53964.4	54242.5	54262.6	54318.5	54407.2
A	14.4076	19.198	19.4 ± 0.1	19.3 ± 0.1	19.2 ± 0.1	19.3 ± 0.1	19.3 ± 0.1	19.3 ± 0.1
B[a]	14.2930	18.999	18.0 ± 0.1					
C	14.3082	19.816	17.2 ± 0.1	17.2 ± 0.1	17.2 ± 0.1	17.2 ± 0.1	17.2 ± 0.1	17.2 ± 0.1
D	14.2861	19.987	18.4 ± 0.1	18.4 ± 0.1	18.4 ± 0.1	18.4 ± 0.1	18.4 ± 0.1	18.4 ± 0.1
E	14.3688	20.981	21.0 ± 0.1	20.8 ± 0.1	20.8 ± 0.1	20.7 ± 0.1	20.6 ± 0.1	20.6 ± 0.1
F	14.3839	18.875	20.2 ± 0.1	20.1 ± 0.1	19.9 ± 0.1	19.9 ± 0.1	20.0 ± 0.1	20.1 ± 0.1
G	14.3454	20.103	19.9 ± 0.1	19.8 ± 0.1	19.8 ± 0.1	19.7 ± 0.1	19.7 ± 0.1	19.8 ± 0.1
H	14.3202	19.919	21.5 ± 0.2	21.0 ± 0.1	20.8 ± 0.1	21.0 ± 0.1	20.6 ± 0.1	20.7 ± 0.1
J	14.3199	19.751	—	22.3 ± 0.2	23.1 ± 0.3	22.2 ± 0.2	21.5 ± 0.1	21.9 ± 0.2

[a]Source B is used to set the zero point in each frame using the photometry described by Kaplan et al. (2002a).

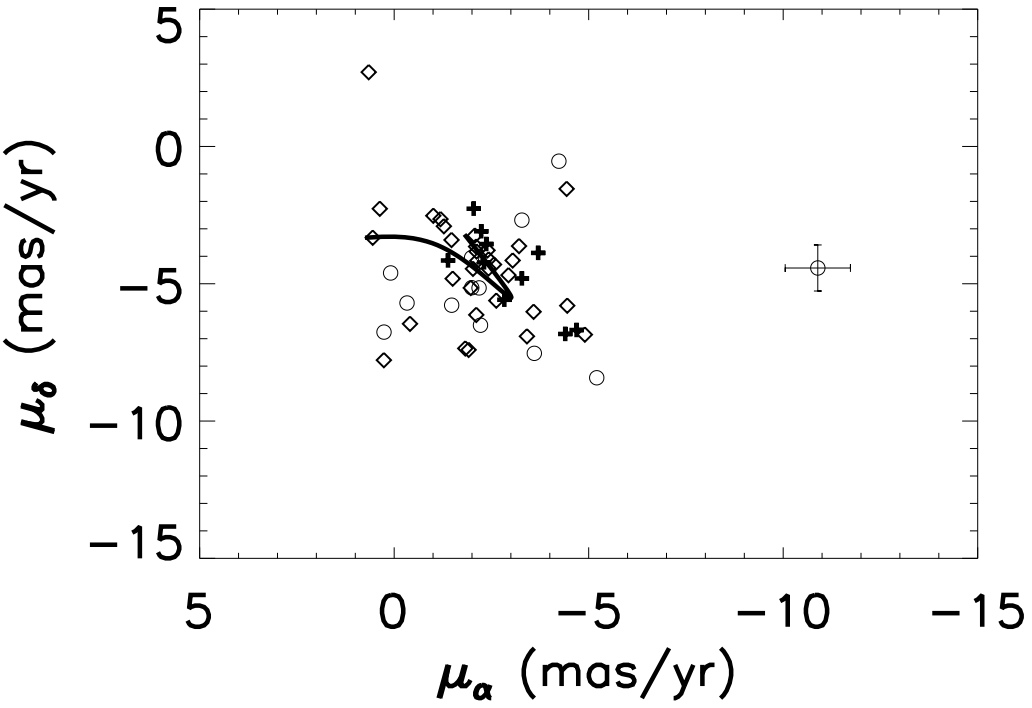

Figure 2.2 Proper motion diagram of 50 stars in the field of SGR 1900+14. The proper motion of source H is denoted with error bars. The remaining stars have only their best-fit values after correction for bulk motion of the field with symbols corresponding to brightness ($K' < 16$ mag, crosses; $16 < K' < 18$, open diamonds; $K' > 20$, open circles). The dispersion in proper motions is $< 2\,\mathrm{mas\,yr^{-1}}$. The expected motion of stars, due to the peculiar motion of the sun and differential Galactic rotation from 1 to 20 kpc along this line of sight, is plotted as a dark line (1 kpc corresponds to $[\mu_\alpha,\mu_\delta] \approx$ [-1,-3.5]).

2.4.2 SGR 1806−20

To calibrate the photometric zeropoints for each epoch of SGR 1806−20 observations, we used stars B and C from Israel et al. (2005), which have K' magnitudes of 19.07 ± 0.04 and 18.77 ± 0.04, respectively. The results are presented in Table 2.1. We see that the counterpart to SGR 1806−20 brightened substantially leading up to the 2004 Dec 27 giant flare, but our subsequent data shows that it has faded considerably (2–2.5 magnitudes) in the aftermath, which poses significant challenges for astrometry.

The proper motions of 80 stars in the narrow camera field of SGR 1806−20 are shown in Figure 2.3. Our best-fit proper motion, including the correction for the bulk motion of the field, is $\mu_\alpha = 1.7 \pm 2.6\,\mathrm{mas\,yr^{-1}}$ and $\mu_\delta = -11.6 \pm 3\,\mathrm{mas\,yr^{-1}}$. As noted above, there has been considerable controversy regarding the distance to SGR 1806−20, but given the preponderance of evidence we adopt a distance of $8.7^{+1.8}_{-1.5}\,\mathrm{kpc}$ (Bibby et al. 2008). This distance results in a transverse velocity of $225 \pm 97\,\mathrm{km\ s^{-1}}$ with an equatorial position angle 172 ± 13 degrees (east of north).

The cluster containing SGR 1806−20 is loosely defined (unlike SGR 1900+14), but it is dominated by LBV 1806−20 (due east of the SGR), a Wolf-Rayet, and 2 B-class supergiants. The latter three are all to the northwest of the SGR, and the measured proper motion would put the SGR in the middle of these objects 10^3–$10^4\,\mathrm{yr}$ ago.

2.4.3 AXP 4U 0142+61

We determined the coadded frame zeropoints with two stars from 2MASS: 2MASS 01462283+6144549 and 2MASS 01462374+6144585. The magnitudes of 4U 0142+61, using these zeropoints, can be found in Table 2.1. The RMS variation in 4U 0142+61 is only 0.9 magnitudes over these two years, which is comparable to the typical RMS variation of 0.08 for stars in our field. Thus, 4U 0142+61 does not show enhanced variability in a relative sense. We do not see any significant change in the IR-flux following the SGR-like outburst from this object on 2006 April 6 or from an activation in 2007 Feb 7 (Kaspi et al. 2006; Gavriil et al. 2007).

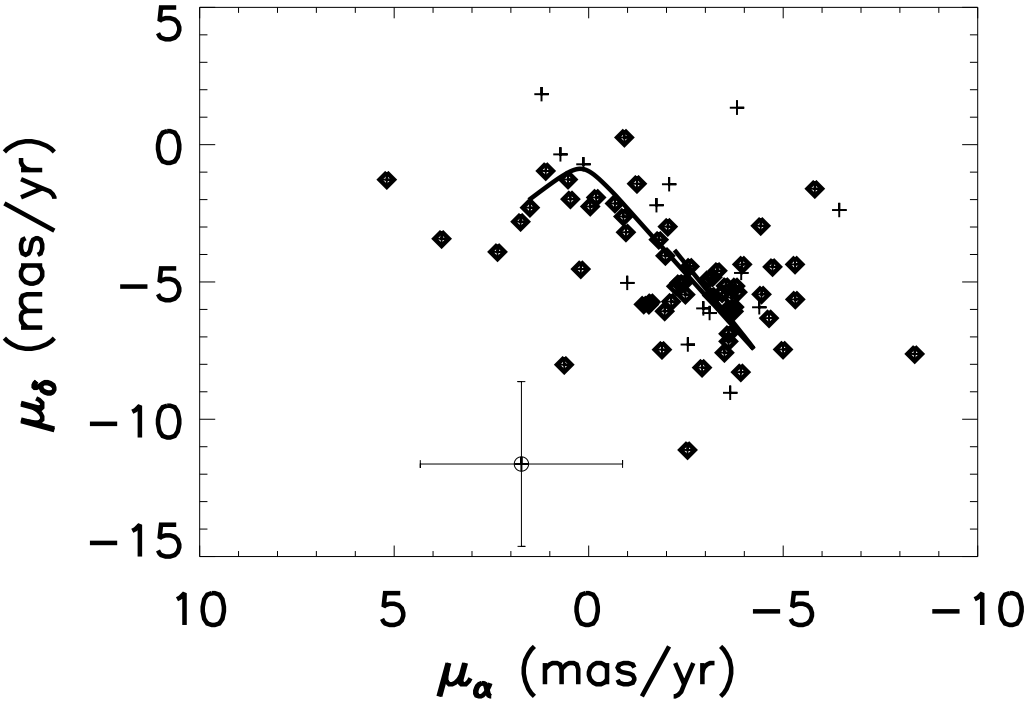

Figure 2.3 Proper motion diagram of 80 stars in the field of SGR 1806−20 (denoted with error bars). The remaining stars have only their best-fit values after correction for bulk motion of the field with symbols corresponding to brightness ($K' < 16$ mag, crosses; $16 < K' < 18$, open diamonds; $K' > 20$, open circles). The expected motion of stars, due to the peculiar motion of the sun and differential Galactic rotation from 1 to 20 kpc along this line of sight, is plotted as a dark line (1 kpc corresponds to $[\mu_\alpha,\mu_\delta] \approx [2,-2]$).

We registered the image from 2005 Sept 26 UT to 2MASS using 5 stars in the NIRC2 wide camera image. We found an RMS variation of 34 mas in each coordinate as a result of this determination. The best-fit position of 4U 0142+61 is $01^{\rm h}46^{\rm m}369^{\rm s}$,$+61^\circ45'03.10''$ with an uncertainty of $0.1''$ in each coordinate relative to the ICRF, which is dominated by the error in the 2MASS catalog. This is $0.3''$ from the position of (Hulleman et al. 2000).

Using the measurement model above, we find that the proper motion of 4U 0142+61 is $\mu_\alpha = -1.05 \pm 2.7\,{\rm mas\,yr^{-1}}$ and $\mu_\delta = -3.7 \pm 2.7\,{\rm mas\,yr^{-1}}$ (Figure 2.4). Correcting the this proper motion to the LSR gives a transverse space velocity of $41 \pm 39\,{\rm km\ s^{-1}}$ assuming a distance of 3.6 ± 0.4 (Durant & van Kerkwijk 2006). This gives a relatively low 3-σ upper limit on the transverse space velocity of $151\,{\rm km\ s^{-1}}$. The directionality of the proper motion is essentially unconstrained at 196 ± 40 degrees east of north, and thus cannot reliably identify a potential birth site. Although, the small proper motion suggests it was born relatively nearby unless it is a very old object.

2.4.4 AXP 1E 2259+586

We determined the coadded frame zeropoints with 3 stars from 2MASS: The magnitudes of 1E 2259+586 using these zeropoints can be found in Table 2.1. The RMS variation in 4U 0142+61 is 0.13 magnitudes over these two years, nearly twice our typical RMS variation of 0.08 magnitudes for stars in our field.

We registered the image from 2005 Aug 10 UT to 2MASS using 9 stars in the NIRC2 wide camera image. We found an RMS variation of 70 mas in each coordinate as a result of this determination. The best-fit position of 1E 2259+586 is $\alpha_{\rm J2000} = 23^{\rm h}01^{\rm m}08.295^{\rm s}$, $\delta_{\rm J2000} = +58^\circ52'44.45''$ with an uncertainty of $0.14''$ in each coordinate relative to the ICRF, which is dominated by the error in the 2MASS catalog. This is $0.326''$ from the position of Hulleman et al. (2001).

Using the measurement model above we find that the proper motion of 1E 2259+586 is $\mu_\alpha = -4.6 \pm 3.9\,{\rm mas\,yr^{-1}}$ and $\mu_\delta = -7.2 \pm 3.9\,{\rm mas\,yr^{-1}}$. We show in Figure 2.5 the proper motions of all the stars in the field along with the expectation from Galac-

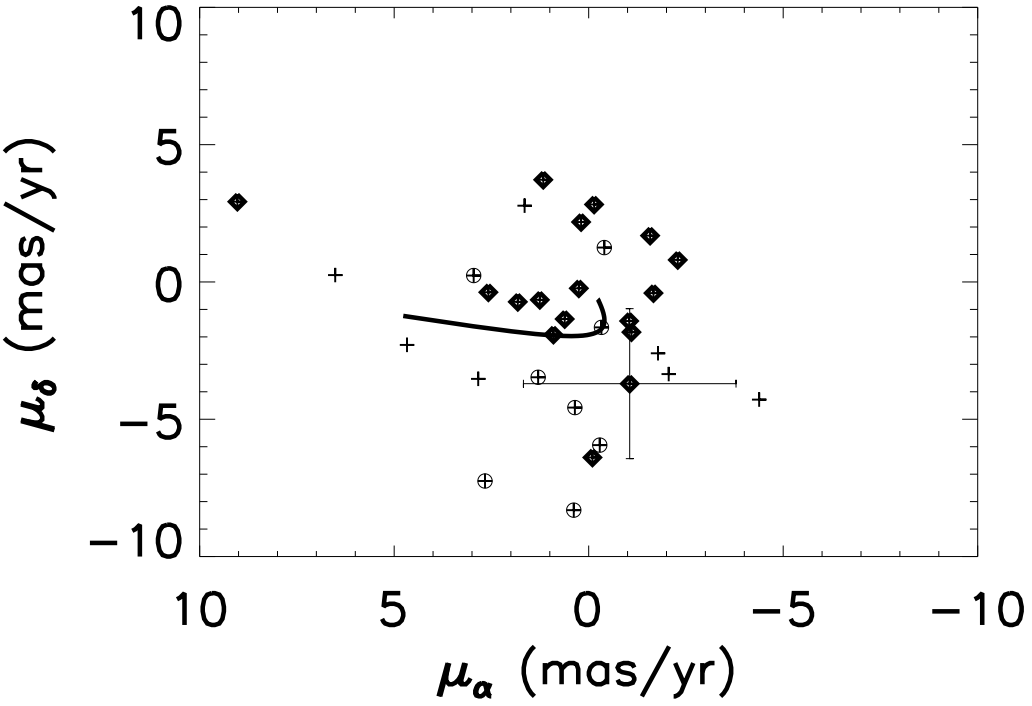

Figure 2.4 Proper motion diagram of stars in the field of 4U 0142+61 (denoted with error bars). The remaining stars have only their best-fit values after correction for bulk motion of the field with symbols corresponding to brightness ($K' < 16$ mag, crosses; $16 < K' < 18$, open diamonds; $K' > 20$, open circles). The expected motion of stars due to peculiar motion of the sun and differential Galactic rotation from 1 to 20 kpc along this line of sight is plotted as a dark line (0.5 kpc corresponds to [μ_α,μ_δ] $\approx$ [5,-1]).

tic rotation and the solar peculiar motion. Correcting the proper motion for those two effects yields a transverse space velocity of 88 ± 52 km s^{-1}at 3.5 kpc or 188 ± 111 km s^{-1} at 7.5 kpc. This gives a 3 σ upper limit on the transverse space velocity of 233 km s^{-1} at 3.5 kpc or 500 km s^{-1} at 7.5 kpc. The position angle is 212 ± 34 degrees east of north, which is only marginally 2–3 σ with the SNR center located at $\alpha_{\rm J2000}$ =23$^{\rm h}$01$^{\rm m}$35.57$^{\rm s}$, $\delta_{\rm J2000}$ =+58°51′08.5″ (Green 1989). If associated with the SNR, the calculated proper motion implies an age of 25000 years.

The astrometric errors for this object are notably larger than our other efforts in part due to the distribution of reference stars around the edges of the chip with little in the vicinity of the AXP. The distortion is largest at the edges of the chips, thus presumably any residual distortion is largest there. In addition, due to the set-up of NIRC the distortion is least well determined in the y-direction (Appendix A). Also, due to poor luck and bad weather we were unable to detect the object in 2007, so the data here have only a 1-year time baseline.

2.4.5 AXP 1E 1841−045

We determined the best astrometric solution by using the data obtained 2005 September 26 UT. We registered a short (1.4 sec) processed exposure with the wide field camera to the 2MASS catalog using 10 stars that were unsaturated and the task CCMAP. This solution had an RMS deviation of ≈ 0.05″ in each coordinate. We then used stars common to both this wide field image and the narrow camera image to transfer the absolute astrometry. The errors involved in this process were negligible by comparison. The astrometric accuracy of the 2MASS catalog with respect to the ICRF is ≈ 0.08, thus our total astrometric uncertainty is 0.11″ (1-σ).

The most precise position for 1E 1841−045 is $\alpha_{\rm J2000}$ = 18$^{\rm h}$41$^{\rm m}$19.343$^{\rm s}$, $\delta_{\rm J2000}$ = −04°56′11.6″ with an error radius of 0.9″ (3-σ; Wachter et al. 2004). This error circle is shown on a registered, stacked image in Figure 2.6. We find 9 sources in the *Chandra* error circle. For comparison, seeing-limited NIR observations by Durant (2005) under excellent conditions (0.35″in K_s) could only identify 4 sources. This

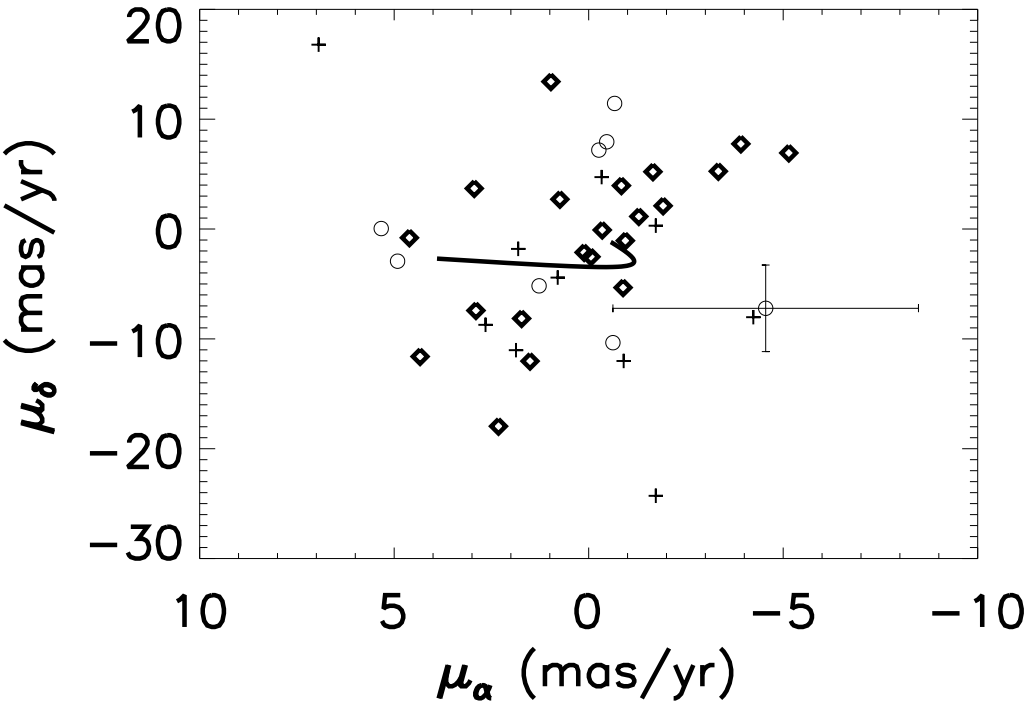

Figure 2.5 Proper motion diagram of 50 stars in the field of 1E 2259+586 (denoted with error bars). The remaining stars have only their best-fit values after correction for bulk motion of the field with symbols corresponding to brightness ($K' < 16$ mag, crosses; $16 < K' < 18$, open diamonds;$K' > 20$, open circles). The expected motion of stars due to peculiar motion of the sun and differential Galactic rotation from 0.5 to 20 kpc along this line of sight is plotted as a dark line (0.5 kpc corresponds to $[\mu_\alpha,\mu_\delta] \approx [4,-3]$).

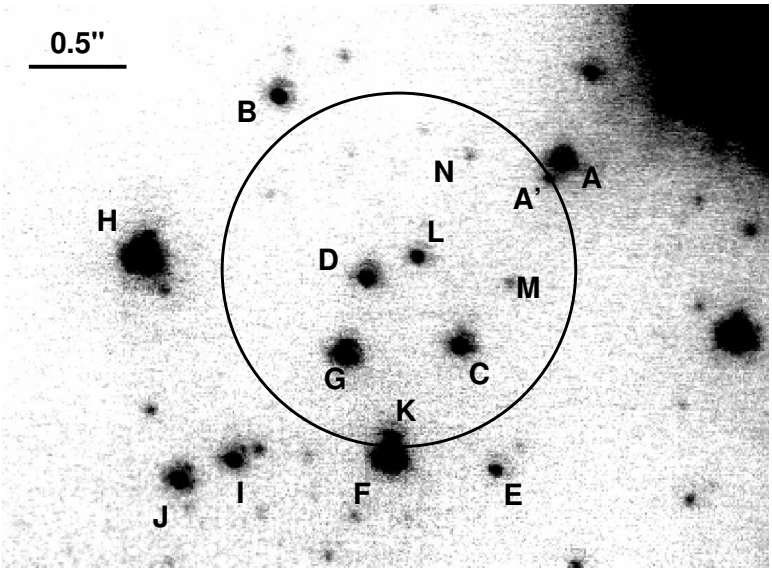

Figure 2.6 Image of the field of 1E 1841−045. The $3\,\sigma$ confidence position is marked by the circle, and the sources are labeled as in Durant (2005). In the image, north is up and east is to the left.

highlights the necessity of adaptive optics for observations in these crowded regions. The astrometry of the identified sources can be found in Table 2.3.

We calibrated the photometric zeropoints of each frame using the brightness of star H as reported to be $K' = 17.4 \pm 0.04$ by Durant (2005). Although several stars have varied during the course of our observation, none can be conclusively identified at counterpart. In particular star B was proposed as the counterpart by Testa et al. (2008), and in addition to the fact that it lies outside our $3\,\sigma$ error circle, it does not show significant variability.

We can place a limit on the proper motion of the magnetar by working under the assumption that the near-infrared counterpart to 1E 1841−045 is among our candidates, but it remains unidentified. None of the candidates in or around the error circle has a proper motion larger than $2\,\sigma$. Star N has the largest proper motion which translates into a $3\,\sigma$ velocity upper limit of $430\,\mathrm{km\ s^{-1}}$ at a distance of 7 kpc.

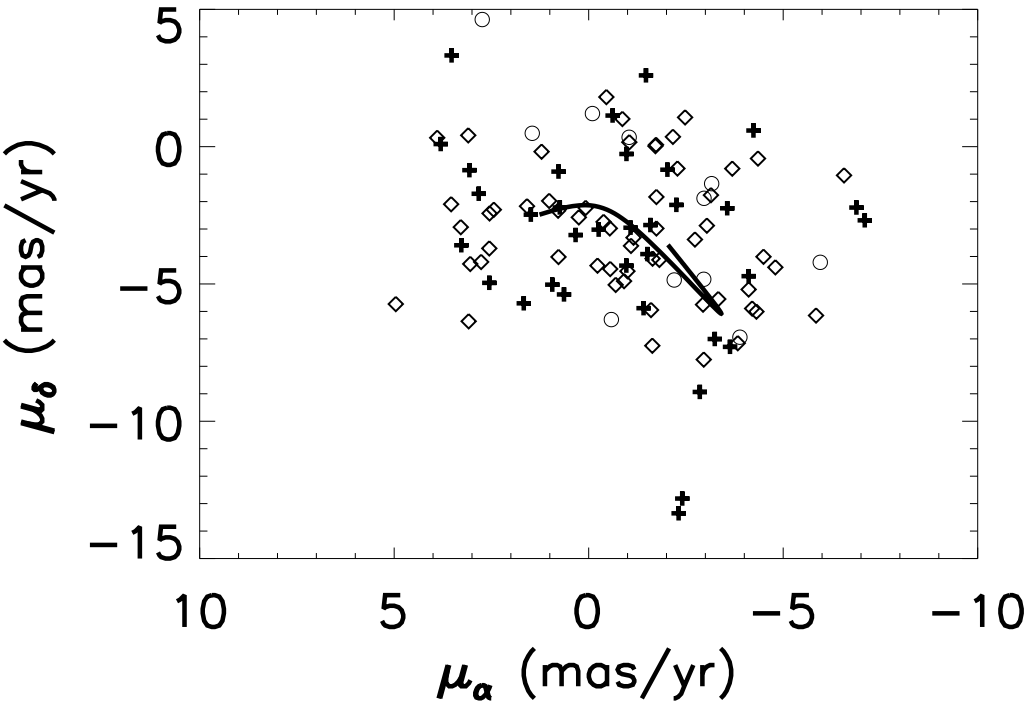

Figure 2.7 Proper motion diagram of 100 stars in the field of 1E 1841−045 (denoted with error bars). The remaining stars have only their best-fit values after correction for bulk motion of the field with symbols corresponding to brightness ($K' < 16$ mag, crosses; $16 < K' < 18$, open diamonds;$K' > 20$, open circles). The expected motion of stars due to peculiar motion of the sun and differential Galactic rotation from 1 to 20 kpc along this line of sight is plotted as a dark line (1 kpc corresponds to [μ_α,μ_δ] $\approx$ [1.5,-2.5]).

Table 2.3. Photometry and Positions of Stars in or Near the Error Circle of 1E 1841−045

Source	RA 18^h41^m	Dec $-04°56^m$	K' (mag) MJD 53639.3	53920.5	53964.4	54242.4	54262.5	54318.4	54607.6
A	19.287	10.63	19.09 ± 0.04	19.09 ± 0.04	19.02 ± 0.04	19.05 ± 0.04	19.07 ± 0.04	19.11 ± 0.05	19.03 ± 0.04
A	19.291	10.71	21.38 ± 0.12	21.03 ± 0.08	20.80 ± 0.06	21.14 ± 0.06	20.84 ± 0.05	20.91 ± 0.08	20.63 ± 0.08
B	19.383	10.29	19.40 ± 0.04	19.40 ± 0.04	19.40 ± 0.04	19.38 ± 0.04	19.39 ± 0.04	19.37 ± 0.04	19.57 ± 0.05
C	19.321	11.56	19.18 ± 0.04	19.20 ± 0.04	19.13 ± 0.04	19.14 ± 0.04	19.14 ± 0.04	19.18 ± 0.04	19.15 ± 0.04
D	19.354	11.21	19.36 ± 0.04	19.27 ± 0.04	19.29 ± 0.04	19.26 ± 0.04	19.26 ± 0.04	19.28 ± 0.04	19.34 ± 0.05
E	19.310	12.19	20.23 ± 0.05	20.16 ± 0.05	20.09 ± 0.05	20.14 ± 0.05	20.09 ± 0.04	20.49 ± 0.07	20.03 ± 0.06
F	19.346	12.13	18.24 ± 0.04	18.27 ± 0.04	18.26 ± 0.04	18.24 ± 0.04	18.25 ± 0.04	18.29 ± 0.04	18.26 ± 0.04
G	19.361	11.61	18.77 ± 0.04	18.77 ± 0.04	18.74 ± 0.04	18.72 ± 0.04	18.73 ± 0.04	18.81 ± 0.04	18.69 ± 0.04
H	19.423	11.26	17.40 ± 0.04	—	—	—	—	—	—
I	19.399	12.13	19.39 ± 0.04	19.30 ± 0.04	19.34 ± 0.05	19.25 ± 0.04	19.31 ± 0.04	19.37 ± 0.05	19.34 ± 0.05
J	19.417	12.24	19.22 ± 0.04	19.11 ± 0.04	19.09 ± 0.04	19.06 ± 0.04	19.11 ± 0.04	19.05 ± 0.04	19.15 ± 0.05
K	19.346	12.01	20.31 ± 0.06	20.12 ± 0.06	20.04 ± 0.05	20.00 ± 0.05	20.16 ± 0.05	20.07 ± 0.07	19.89 ± 0.06
L	19.336	11.11	20.22 ± 0.05	20.01 ± 0.05	19.92 ± 0.05	20.01 ± 0.04	19.98 ± 0.04	20.16 ± 0.05	19.88 ± 0.06
M	19.305	11.24	21.53 ± 0.11	21.55 ± 0.11	21.40 ± 0.09	21.29 ± 0.06	21.33 ± 0.05	21.41 ± 0.10	21.72 ± 0.22
N	19.319	10.60	21.44 ± 0.10	21.71 ± 0.15	21.06 ± 0.08	21.52 ± 0.07	21.38 ± 0.06	21.05 ± 0.08	20.98 ± 0.10

2.5 Discussion and Conclusions

The results of the laser guide star adaptive optics imaging presented here address many of the key issues surrounding magnetar origins and evolution. The 200–500 km s^{-1} transverse motion of SGR 1900+14 radially away from the massive star cluster allows the first model independent determination of a magnetar age, and secures its birth site without the need to appeal to *a posteriori* statistical arguments. The remaining four magnetars in our sample do not have such clear detections of motions, but the limits placed constrain their transverse velocities to be $\lesssim 500$ km s^{-1}(and in two cases $\lesssim 100$ km s^{-1}).

The discovery of 'SGR-like' outbursts from 1E 2259+586 was the first direct evidence of the connection between SGRs and AXPs (Kaspi et al. 2003). However, the nature of the relation based on indirect evidence, such as putative associations and angular offsets, is unclear (Gaensler et al. 2001). On one hand, the proximity of a number of AXPs to SNR centers (e.g., 1E 1841−045 and 1E 2259+586) when compared to the enormous distances of SGR 0526−66 and SGR 1900+14 from nearby SNR suggests that SGRs are either very high velocity objects, or a much older population. On the other hand, the remarkable high-energy activity of SGRs would suggest they are the younger population. The directly measured low proper motions of SGR 1900+14 and SGR 1806−20 presented here prove that the SGRs need not have incredible space velocities when compared to AXPs or radio pulsars. In addition, for the two objects which we can reliably estimate ages (SGR 1900+14 and 1E 2259+586), the conclusion is that SGRs are the younger neutron stars.

The association of magnetars with very massive progenitors has been supposed since the discovery of a wind blown bubble around 1E 1048.1-5937, the embedding of SGR 1806−20 in the unusual cluster containing LBV 1806−20, and the discovery of a magnetar in the massive star cluster, Westerlund 1 (Gaensler et al. 2005c; Kulkarni et al. 1995; Muno et al. 2006). The only questions surrounding these conclusions involve the facts that: the SNR of AXPs are unremarkable, that the revised distance of SGR 1806−20 calls into question its association with the cluster, and that the

magnetar in Westerlund 1 lies many core radii away from the center of the cluster. The direct association of SGR 1900+14 with nearby massive stars lends credibility to the argument of massive magnetar progenitors.

Modern multi-dimensional supernova simulation codes have suggested a number of features relevant to the neutron star kicks. For example, Burrows et al. (2007a) review a mechanism leading to a Standing-Accretion-Shock-Instability (SASI) and acoustic power in the collapsing star which causes an asymmetric wind. In this case, an outflow provides net momentum to the proto-neutron star and also provides a channel which is less opaque to neutrinos, thereby adding the hydrodynamic and neutrino kick mechanisms. The final recoil in their simulations is shown only to be $50\,\mathrm{km\ s^{-1}}$, but it should be noted that the final velocity has not converged at the end of the simulation. This mechanism requires no exotic physics, only an asymmetric explosion mechanism. Since both the explosion energies and neutrino contributions are suggested to rise with progenitor mass (Burrows et al. 2007b), there is a prediction that more massive progenitors should yield neutron stars with higher space velocities. But whether these correlations seen at lower masses ($\approx 10\,M_{\odot}$) extend to the very massive progenitors of magnetars remains to be seen.

In the "flux freezing" magnetar formation scenario it is thought that magnetar fields are generated by the conservation of magnetic flux during the collapse of the stellar progenitor (Ferrario & Wickramasinghe 2006). On average, higher magnetic fluxes are found in more massive progenitors, giving a theoretical expectation to the observed relationship of magnetars and massive stars (Mereghetti 2008). If the supernova simulation results can be extrapolated to high mass, then this would suggest a higher velocity of magnetars when compared to normal neutron stars.

In the magnetar formation scenario of Duncan & Thompson (1992), ultra-strong magnetic fields are generated via an efficient dynamo produced by helical motions in a rapidly spinning proto-neutron star (Thompson & Duncan 1993). They predict that if the magnetic field is generated in this fashion, a number of magnetic effects should generate anisotropic emission of neutrinos resulting in a net momentum to the proto-neutron star with velocities $\gtrsim 1000\,\mathrm{km\ s^{-1}}$. The thinking is that a locally

strong magnetic field on the proto-neutron star will suppress energy transport by convection and thus reduce the local neutrino emission. Additionally, the neutrino interaction cross-section is modified in the presence of a magnetic field due to the weak interaction. At magnetar field strengths this could be sufficient to alter the neutrino radiation field.

Between the 5 objects studied here and the measured proper motion of XTE J1810−197, nearly half of the magnetar population show space velocities that are not distinct from canonical radio pulsars. This implies that whichever mechanism is responsible for generating their ultra-strong magnetic field strengths, it does not manifest itself through remarkable kinematics. Given the ubiquity of large proper motion predictions for magnetars, the lack of correlation of neutron star proper motions with progenitor mass or magnetic field strength challenges our current understanding of core collapse and neutron star formation.

Chapter 3

Discovery of a Radio Counterpart to the 27 December 2004 Giant Flare from SGR 1806−20[†]

Over a decade ago, it was established that the remarkable high energy transients, known as soft gamma-ray repeaters (SGRs), were a Galactic population and originates from neutron stars with intense ($\lesssim 10^{15}$ G) magnetic fields ("magnetars"; Kulkarni & Frail 1993; Murakami et al. 1994; Woods & Thompson 2004). On 27 December 2004 a giant flare (fluence, $\gtrsim 0.3$ erg cm^{-2}; Borkowski et al. 2004; Boggs et al. 2005) was detected from SGR 1806−20. Here we report the discovery of a fading radio counterpart. We began a monitoring program from 0.2 GHz to 100 GHz and obtained a high resolution 21-cm radio spectrum which traces the intervening interstellar neutral Hydrogen clouds. From the analysis of the spectrum, we argue that the source is certainly located at a distance greater than 6.4 kpc and likely less than 9.8 kpc. If so, our distance estimate relaxes the total energy of the explosion and lessens the challenge to theoretical models. The energetics and the rapid decay of the radio source is not compatible with the afterglow model that is usually invoked for gamma-ray bursts. We suggest that the early radio emission arises from the shock of the debris (reverse shock). Radio observations thus offer a new probe into both the explosion and the debris of these rare events.

On 3 January 2005, we observed SGR 1806−20 with the Very Large Array (VLA)

[†]A version of this chapter has been published as Cameron *et al.* 2005, Nature, 434, 1112.

and identified and promptly reported a new radio source at right ascension α_{J2000} $=18^{\rm h}08^{\rm m}39.34^{\rm s}$ and declination δ_{J2000} $=-20^\circ24'39.7$ (with an uncertainty of ±0.1" in each coordinate) coincident with the quiescent X-ray counterpart (Cameron & Kulkarni 2005; Kaplan et al. 2002b). In Table 3.1 we report the results of a subsequent monitoring program undertaken the with VLA, the Giant Metrewave Radio Telescope (GMRT), the Australia Telescope Compact Array (ATCA), the Nobeyama Millimeter Array (NMA), and the Institut de RadioAstronomie Millimétrique (IRAM) 30m Telescope.

The radio source decays in all frequency bands, but the behaviour is complex (Figure 3.1). At each band we model the flux by a power law, $S_\nu(t) \propto t^\alpha$, but allow for changes in α ("breaks") at two epochs. These breaks are clearly seen at the highest frequencies which also have the highest signal-to-noise ratios. Following the first break (9 days, postburst), the light curve steepens, $\alpha \sim -3$ to -4. Subsequently around day 14 the light curve flattens, $\alpha \sim -1$. At any given epoch, the radio spectrum can be modeled by a power law, $S_\nu \propto \nu^\beta$. The spectral index steepens with time, changing from ~ -0.7 to -0.9 (see Figure 3.1, caption). The radio source is similar spectrally and especially temporally to that seen from SGR 1900+14 following the 27 August 1998 giant flare (Frail et al. 1999; Feroci et al. 2001).

We confirm that the source is resolved by an independent analysis (Gaensler et al. 2005b). We find that it is elongated with a major axis $\theta \sim 77$ milliarcsecond (mas) and an axial ratio of 2:1 (Table 3.2). We considered four expansion models, $\theta \propto t^s$ with unconstrained s and s fixed to 0, 2/5 and 1. The best-fit model corresponds to $s = 0.04 \pm 0.15$ (i.e., no expansion), but other models cannot be ruled out.

We took advantage of the brightness of the radio source and obtained a high resolution spectrum (Figure 3.2, second panel) centered around the 21-cm line of atomic Hydrogen (HI). Intervening interstellar clouds appear as absorption features in the spectrum. These clouds are expected to participate in the rotation of the Galaxy and the absorption features allow us to infer "kinematic" distance estimate. Such estimates have several complications. First, in the inner Galaxy the radial velocity curve is double-valued (see Figure 3.2, third panel) leading to a near and

far distance for each velocity. Second, in some directions, there are features with non-circular motion, e.g., the "3 kpc expanding arm" and the "-30 km s^{-1} spiral arm" (Corbel & Eikenberry 2004). Finally, in the innermost part of the Galaxy there is a deficit of cold gas (Kolpak et al. 2002).

Significant HI absorption toward SGR 1806−20 is seen over the velocity range -20 km s^{-1} to $+85$ km s^{-1} (Figure 3.2, second panel). There is also a weak (2.5-σ) absorption feature coincident in velocity with a clearly detected ^{12}CO(1-0) emission feature identified as MC94 (Figure 3.2, first panel; Corbel et al. 1997). Adopting a simple Galactic rotation curve with a circular velocity $\Theta_\circ = 220$ km s^{-1} and a Galactic center distance R$_\circ$=8.5 kpc, the near distance to SGR 1806−20 (for V$_{LSR}$=95 km s^{-1}) is d$_l$=6.4 kpc.

The two HI emission clouds seen at velocities above 100 km s^{-1} toward SGR 1806−20 (Figure 3.2; first panel), with no corresponding HI absorption, may be used to infer an upper limit to the distance provided that we can be reasonably certain that cold neutral gas exists at these velocities. The HI absorption spectrum toward the nearby ($\Delta\theta = 0.77^\circ$) extragalactic source, J1811−2055, shows a strong and broad absorption feature between 110 and 130 km s^{-1} (Figure 3.2, fourth panel). The only HI emission in this direction above 60 km s^{-1} corresponds to an HI cloud at this same velocity (Hartmann & Burton 1997). This feature can be traced in absorption toward several other extragalactic radio sources in this direction, suggesting that cold gas at $\sim$120 km s^{-1} is widespread (Garwood & Dickey 1989). Adopting the same Galactic rotation curve as above, the absorbing cloud at $+120$ km s^{-1} can either be located at 7 kpc or 9.8 kpc (see Figure 3.2, third panel). We thus suggest an upper limit to the distance, d$_u$=9.8 kpc.

These new distance limits differ from the previous d=12–15 kpc inferred for SGR 1806−20, and would require a reduction in the total energy released ($\propto d^2$), and the cosmological event rate of giant flares ($\propto d^3$;Figer et al. 2004; Corbel & Eikenberry 2004). Furthermore, if the upper distance limit is correct, then it implies that the SGR 1806−20 is not physically associated with a massive stellar cluster along the line of sight (Fuchs et al. 1999).

Next we consider the energetics of the material giving rise to the radio emission. As with many other radio sources, the power law spectrum can be attributed to energetic electrons with a power law energy distribution ($dN/d\gamma \propto \gamma^{-p}$; here γ is the Lorentz factor of electrons and p is usually 2.2) which gyrate in a magnetic field and emit synchrotron radiation. We apply the usual "minimum" energy formulation to the radio spectrum (from 0.2 GHz to 100 GHz) of the 3 January 2005 spectrum and find the energy of the radio emitting source and the associated magnetic field strength are $U_{min} \sim 10^{43} d_{10}^{17/7} \theta_{75}^{9/7}$ erg and $B_{min} \sim 13 d_{10}^{-2/7} \theta_{75}^{-6/7}$ mG; here, the angular diameter is $75\theta_{75}$ mas (Table 3.2; Pacholczyk 1970; Scott & Readhead 1977).

Evidently the amount of energy released in the γ-ray flare, $E_{\gamma,\rm iso}$, substantially exceeds $U_{\rm min}$. It is interesting that the ratio $U_{\rm min}/E_{\gamma,\rm iso} \sim 0.4\%$ is similar to that for the 27 August 1998 event. In contrast, this ratio is unity for GRBs and as a result the lower energy and longer duration emission is correctly regarded as arising from the shock of the circumburst medium (the "afterglow" model). Thus, based solely on energetics, there is no *prima facie* reason to suggest that the radio source is the afterglow of the γ-ray flare.

Furthermore, as discussed above, the radio emission decays quite rapidly, $\alpha \sim -3$ to -4. Such a rapid decay is incompatible with the afterglow model (in the non-relativistic limit) in which we expect $\alpha = 3\beta + 0.6$ (Frail et al. 2000). We conclude (in contrast to Cheng & Wang 2003; Nakar et al. 2005, and Wang et al. 2005) that the radio emission must be powered by something very different from that which produced the γ-ray emission.

In summary, the radio emission can be described by two components: a rapidly decaying component and a slowly decaying component (whose angular size is not constrained by our data). The latter becomes detectable when the former has decayed significantly. The rapid decay is phenomenologically similar to that seen from accreting Galactic sources (e.g., Hjellming et al. 2000) – the so-called "plasmon" model framework in which the radio emission arises from a ball of electrons and magnetic field which are initially shocked and then cool down by expansion. We make the specific suggestion that the radio emission up until about 2 weeks is a result of the

shocking of the debris given off in the explosion (the "reverse shock").

Undoubtedly, elaborate and clever models can be invoked to explain the entire complexity of the light curves. However, the comparable ratios $U_{min}/E_{\gamma,\rm iso}$ and the temporal and spectral similarities of the two giant flares do not favor contrived models. Regardless, it is clear that radio afterglow is telling us something entirely different from that revealed by the γ-ray emission. If our suggestion of a reverse shock origin is correct, then radio observations allow us to probe the debris (ejecta). Taken together it appears that rapid and intense monitoring across the radio band of future such flares will be highly fruitful.

ATCA is funded by the Commonwealth of Australia for operation as a National Facility managed by CSIRO. GMRT is run by the National Centre for Radio Astrophysics-Tata Institute of Fundamental Research, India. We thank the GMRT staff and, in particular, C. H. Ishwara-Chandra and D. V. Lal for help with observations and analysis. The VLA is a facility of the National Science Foundation operated under cooperative agreement by Associated Universities, Inc. NMA is a branch of the National Astronomical Observatory, National Institutes of Natural Sciences, Japan. IRAM is supported by INSU/CNRS (France), MPG (Germany) and IGN (Spain). We thank S. Corbel, S. S. Eikenberry and R. Sari for useful discussions, K. Newton-McGee and B. Gaensler for scheduling and performing observations with the ATCA, and A. Weiss from IRAM for help with the observations. Our work is supported in part by the NSF and NASA.

Table 3.1. Flux Density Measurements of the Radio Counterpart to SGR 1806−20

Epoch	Telescope	Δt^a (days)	$S_{0.24}$ (mJy)	$S_{0.610}$ (mJy)	$S_{1.46}$ (mJy)	$S_{2.4}$ (mJy)	$S_{4.86}$ (mJy)	$S_{6.1}$ (mJy)	$S^b_{8.46}$ (mJy)	S_{102} (mJy)
3.84 Jan 2005	VLA	6.94	—	—	178 ± 4	—	79 ± 2	—	53 ± 1	—
4.17 Jan 2005	NMA	7.27	—	—	—	—	—	—	—	16.3 ± 5.6
4.41 Jan 2005	GMRT	7.51	466 ± 28	224 ± 13	—	—	—	—	—	—
4.59 Jan 2005	VLA	7.69	—	—	161 ± 4	—	66 ± 2	—	44 ± 1	—
5.26 Jan 2005	ATCA	8.36	—	—	127 ± 3	80 ± 2	—	—	—	—
5.66 Jan 2005	VLA	8.76	—	—	—	—	55 ± 1	—	33 ± 1	—
5.85 Jan 2005	ATCA	8.93	—	—	113 ± 3	63 ± 2	53 ± 2	—	30 ± 1	—
6.26 Jan 2005	ATCA	9.36	—	—	96 ± 3	73 ± 2	45 ± 2	—	23 ± 1	—
6.38 Jan 2005	GMRT	9.48	462 ± 29	142 ± 8	—	—	—	—	—	—
6.77 Jan 2005	VLA	9.87	—	—	93 ± 2	—	38 ± 1	—	23.5 ± 0.5	—
6.77 Jan 2005	ATCA	9.87	—	—	85 ± 3	67 ± 2	40 ± 1	32 ± 1	—	—
7.20 Jan 2005	ATCA	10.30	—	—	88 ± 2	55 ± 1	—	—	—	—
7.25 Jan 2005	GMRT	10.35	231 ± 20	125 ± 9	—	—	—	—	—	—
7.90 Jan 2005	VLA	11.00	—	—	71 ± 2	—	26 ± 1	—	16.5 ± 0.5	—
8.19 Jan 2005	ATCA	11.29	—	—	67 ± 3	38 ± 2	24 ± 1	20 ± 1	—	—
8.24 Jan 2005	GMRT	11.34	250 ± 17	104 ± 8	—	—	—	—	—	—
9.06 Jan 2005	ATCA	12.16	—	—	42 ± 2	32 ± 1.5	21 ± 1	—	11.4 ± 1	—
9.26 Jan 2005	GMRT	12.36	176 ± 20	86 ± 7	—	—	—	—	—	—
10.07 Jan 2005	ATCA	13.16	—	—	32 ± 2	24 ± 1	17 ± 1	—	10 ± 1	—
10.16 Jan 2005	GMRT	13.26	155 ± 17	82 ± 7	—	—	—	—	—	—
10.60 Jan 2005	VLA	13.70	—	—	—	—	—	—	8.7 ± 0.4	—
12.00 Jan 2005	NMA	15.10	—	—	—	—	—	—	—	7.16[c]
12.04 Jan 2005	ATCA	15.14	—	—	24 ± 1.5	16 ± 1	12 ± 1	9.3 ± 1	7.3 ± 1	—

3.1 Supplemental Information

3.1.1 Further Discussion of Flux Density Measurements

For the VLA observations we used the standard continuum mode with 2×50 MHz bands, with the exception of the 1.46 GHz observation of 4 January 2005, which was taken in spectral line mode with 8 channels of width 3.1 MHz. We used the extra-galactic source 3C 286 (J1331+305) for flux calibration, while the phase was monitored with J1820-254, J1751−253, and J1811−209.

The flux densities and uncertainties listed in Table 3.1 were measured from the resulting maps by fitting an elliptical Gaussian model to the afterglow emission. The GMRT observations were performed in dual frequency mode with 16 MHz of bandwidth divided into a total of 128 frequency channels for the 610 MHz observations, and 6 MHz of bandwidth divided into 64 channels for the 235 MHz observations. 3C 48 (J0137+331) and 3C 286 were used as flux calibrators, and J1822−096 was used as the phase calibrator. These sources were also used for bandpass calibration. We obtained the flux densities of the source by fitting a Gaussian model with a background level plus a slope and removed the contribution from a nearby weak source. Because of the high density of radio sources in the galactic plane in which SGR 1806−20 is located, the antenna system noise temperature has notable contributions from the sky within the telescope beam. This reduces the signal to noise ratio and an appropriate correction must be made to the observed flux (especially at low frequencies), since the flux calibrators which establish the flux scale lie well outside the galactic plane and are in an environment of less sky temperature. We applied a T_{sys} correction factor for 3C 48 of 3.88 and 1.93, and for 3C286 of 3.87 and 1.8, for the 235 MHz and the 610 MHz, respectively.

Both the VLA and GMRT data were reduced and analyzed using the Astronomical Image Processing System. The ATCA observations were performed in snapshot mode with 100MHz of effective bandwidth. The amplitude calibrator was J1934−638, whereas J1711−251, J1817−254, and J1811−209 where used as phase calibrators. The last of these was observed in a rapid (3 minute) cycle mode to compensate for

Table 3.1—Continued

Epoch	Telescope	Δt^a (days)	$S_{0.24}$ (mJy)	$S_{0.610}$ (mJy)	$S_{1.46}$ (mJy)	$S_{2.4}$ (mJy)	$S_{4.86}$ (mJy)	$S_{6.1}$ (mJy)	$S^b_{8.46}$ (mJy)	S_{102} (mJy)
13.00 Jan 2005	NMA	16.10	—	—	—	—	—	—	—	5.50[c]
14.04 Jan 2005	ATCA	17.14	—	—	23 ± 1	15 ± 1	9.7 ± 1	7.3 ± 1	5.5 ± 1	—
16.25 Jan 2005	GMRT	19.35	96 ± 23	31 ± 5	—	—	—	—	—	—
16.37 Jan 2005	GMRT	19.47	—	—	20 ± 2[d]	—	—	—	—	—
18.01 Jan 2005	ATCA	21.11	—	—	24 ± 1.5	17 ± 1	6.2 ± 1	4.7 ± 1	3.8± 1	—
20.10 Jan 2005	ATCA	23.20	—	—	19 ± 1.5	10 ± 1.5	5 ± 1	—	3.2± 1	—
22.07 Jan 2005	ATCA	25.17	—	—	18 ± 1	11 ± 1	5 ± 1	4.3± 1	2.0± 1	—
23.84 Jan 2005	ATCA	26.94	—	—	12 ± 1	7.9 ± 1	5.6 ± 1	3.7± 1	3.6± 1	—
24.85 Jan 2005	ATCA	27.95	—	—	12 ± 1	11 ± 1	4.2 ± 1	5.1± 1	3.6± 1	—
26.26 Jan 2005	GMRT	29.36	104 ± 31	19 ± 6	—	—	—	—	—	—
4.01 Feb 2005	GMRT	38.14	—	—	10[c,d]	—	—	—	—	—
16.87 Feb 2005	ATCA	50.97	—	—	10 ± 1	6.3 ± 1	3.3 ± 0.4	—	2.1 ± 0.3	—

Note. — Flux density measurements of the transient radio counterpart to SGR 1806−20 from the VLA, GMRT, NMA, and ATCA as a function of frequency and time. The reported errors are 1-σ. In addition to these measurements, we obtained IRAM-30m observations on 8 and 9 January 2005 using MAMBO-2 at 250 GHz which show no detection with a value of 0.57 ± 0.46 mJy at the position of the radio source. Finally, we detect linearly polarized emission from the source at the 1.5% to 2.5% level. See the Supplemental Information for observational details.

[a] The epoch of the flare, t_0, was 27.90 December 2004.

[b] ATCA observations in this column have a frequency of 8.6 GHz.

[c] These values represent 2σ upper limits.

[d] The frequency is 1.060 GHz for the 16.37 January 2005 and 4.01 February 2005 GMRT observations.

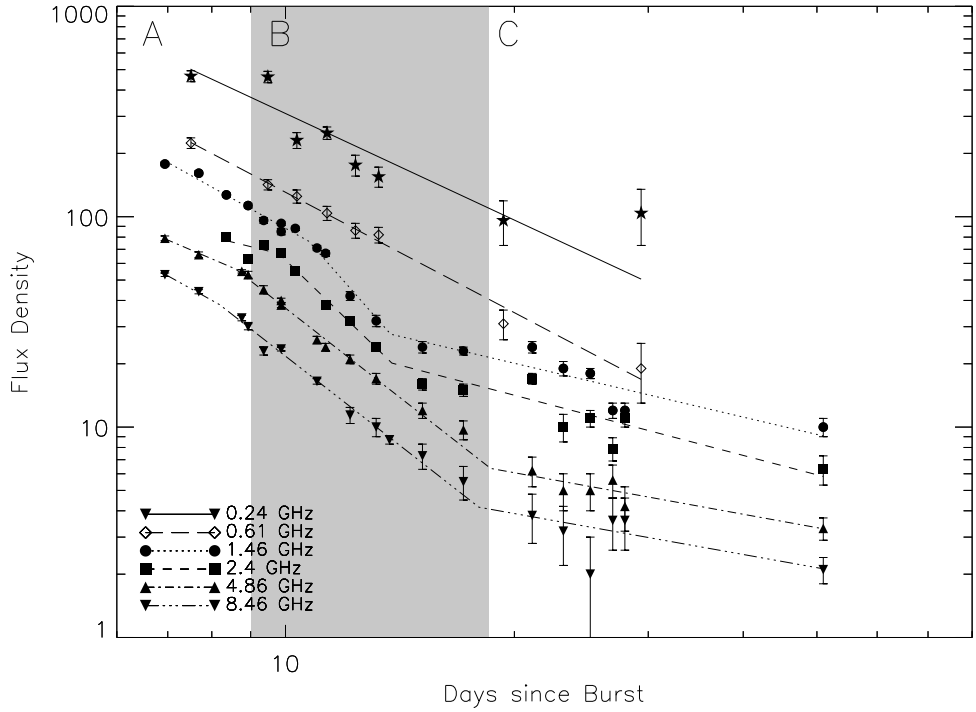

Figure 3.1 Broadband temporal behavior of the transient radio source coincident with SGR 1806−20. The abscissa indicates days elapsed since the giant flare on 27.90 December 2004. The displayed flux density measurements (denoted with symbols) were obtained in six frequency bands with the VLA, GMRT, and ATCA (Table 3.1). The error bars denote 1-σ uncertainties. With the exception of the 6.1 GHz data (which is insufficiently sampled at early and late times and is not shown), the light curves with $\nu > 1$ GHz are best-fit by power-law models (shown as lines, $S_\nu \propto t^{\alpha_i}$) with two breaks at $t_1 \sim 9$ days and $t_2 \sim 15$ days (see Table 3.3 in the Supplemental Information). The temporal index varies chromatically in the time before and after the first break (denoted by regions A and B respectively). The exponent value ranges from $-2 \lesssim \alpha_A \lesssim -1$ and $-4 \lesssim \alpha_B \lesssim -3$; here the subscript identifies the region of interest. After day ~ 15 (region C) the source decay flattens to $\alpha_C \sim -0.9$ at these frequencies which persists until day 51. Region B, the period of steep light curve decline, is shaded gray. The light curves with $\nu < 1$ GHz do not show these temporal breaks, although they are not well sampled at late times. Their single power-law decay slopes are -1.7 ± 0.1 and -1.9 ± 0.1 for 0.24 GHz and 0.61 GHz, respectively. Our substantial frequency coverage (nearly three decades) allows an excellent characterization of the spectrum. The spectrum is consistent with a single power law slope ($S_\nu \propto \nu^\beta$) at all epochs. On day 7, before the first break, we find $\beta = -0.62 \pm 0.02$. The spectrum steepens to a value of $\beta = -0.76 \pm 0.05$ (day 15), reaching $\beta = -0.9 \pm 0.1$ (days 21–51).

Table 3.2. SGR 1806−20 Radio Source Size Measurements

Epoch	Beam (mas)	Beam PA (degrees)	Fit Major Axis (mas)	Axial Ratio	Fit PA (degrees)
03 Jan 2005	349×170	11.8	$78.2^{+3.0}_{-2.9}$	$0.34^{+0.21}_{-0.34}$	$54.6^{+6.7}_{-6.0}$
04 Jan 2005	593×173	−40.3	$72.4^{+14.5}_{-48}$	$0.00^{+0.90}_{-0}$	69^{+20}_{-67}
05 Jan 2005	397×168	−25.7	55^{+18}_{-10}	$0.66^{+0.34}_{-0.66}$	74^{+90}_{-90}
06 Jan 2005	329×178	−16.5	$75.7^{+3.0}_{-3.0}$	$0.48^{+0.18}_{-0.33}$	$51.8^{+9.0}_{-8.8}$
07 Jan 2005	532×178	40.4	78^{+26}_{-18}	$0.60^{+0.4}_{-0.60}$	69^{+90}_{-90}
10 Jan 2005	560×161	−38.8	112^{+30}_{-42}	$0.34^{+0.33}_{-0.34}$	18^{+28}_{-18}

Note. — Source size measurements and 95% confidence limits of the radio source as measured with the VLA at 8.46 GHz. The source is clearly resolved at all VLA epochs. The best constraints on the source size come from the observations which occurred closest to the transit of the source on January 3rd and January 6th. The result is a source with size $\theta \sim 77$ mas with an axial ratio of ~ 0.5 and a position angle (PA) of 60 degrees (measured clockwise from the North). The flux centroid did not change position within the limits of our astrometric accuracy ($\pm$ 100 mas). The best-fit model is consistent with no expansion, $s = 0.04 \pm 0.15$ ($\theta(t) \propto t^s$) with a $\chi^2 = 5.3$ with 4 degrees of freedom. Sedov-Taylor ($s = 2/5$) and free expansion ($s = 1$) model were also fit, and yield $\chi^2 = 20.6$ and $\chi^2 = 91$, respectively. Both models have 5 degrees of freedom. See the Supplemental Information for the details of the source size measurements.

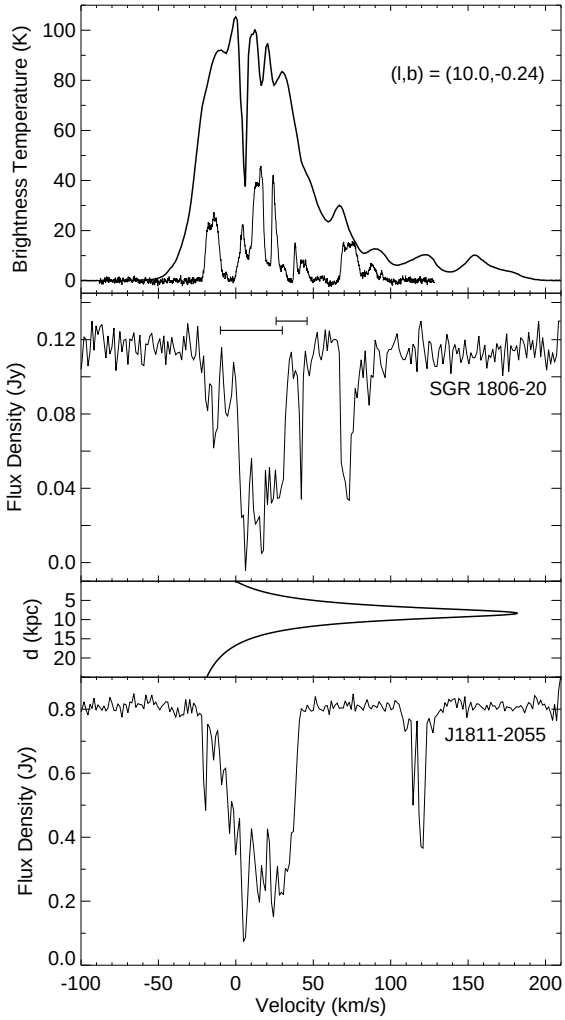

Figure 3.2 Cold atomic and molecular hydrogen spectra used to derive a kinematic distance to SGR 1806−20. The top panel displays the HI emission (upper curve, thick line) in the direction of SGR 1806−20, determined by averaging two adjacent spectra taken by Hartmann & Burton 1997 at l, b=(10.0°,0.0°) and l, b=(10.0°,−0.5°), and a ^{12}CO(1−0) spectrum (lower curve, thin line) taken by Corbel & Eikenberry 2004 with the brightness temperature scaled up by a factor of 11.4. The second panel is an HI absorption spectrum taken toward SGR 1806−20 where the two horizontal bars illustrate the radial velocity measurements of the nearby star LBV 1806−20 (36 ± 10 km s^{-1} and 10 ± 20 km s^{-1}; Figer et al. 2004; Corbel & Eikenberry 2004). The third panel shows the distance as a function of velocity adopting a simple Galactic rotation curve with a circular velocity $\Theta_\circ = 220$ km s^{-1} and a galactic center distance $R_\circ$=8.5 kpc. The fourth panel is an HI absorption spectrum of nearby extragalactic source J1811−2055 at l, b=(9.8°,−1.0°). The absorption spectra were made with the Very Large Array on 4 January 2005, using a 1.56 MHz bandwidth in both hands of polarization centered 50 km s^{-1} with respect to the local standard of rest. The bandwidth was divided into 256 channels each 6.1 kHz in width, or a velocity resolution of 1.3 km s^{-1} covering a velocity range of −115 km s^{-1} to +215 km s^{-1}.

Table 3.3. Summary of Power-law Fits to Lightcurve Decay

Frequency (GHz)	α_A	t_1 (days)	α_B	t_2 (days)	α_C
0.240	-1.7 ± 0.1	—	—	—	—
0.61	-1.9 ± 0.1	—	—	—	—
1.4	-2.0 ± 0.2	10.7 ± 0.3	-4.1 ± 0.3	13.8 ± 0.2	-0.85 ± 0.2
2.4	-0.95 ± 0.3	9.8 ± 0.2	-3.5 ± 0.2	13.8 ± 0.5	-0.95 ± 0.2
4.9	-1.55 ± 0.15	8.8 ± 0.2	-3.1 ± 0.2	18.6 ± 3.0	-0.65 ± 0.3
6.1	-2.3 ± 0.1	—	—	—	—
8.5	-2.00 ± 0.15	8.1 ± 0.3	-2.8 ± 0.24	18.0 ± 3.0	-0.64 ± 0.4

Note. — Summary of temporal indices and breaks in the light curve of SGR 1806−20 in 7 frequency bands. The fits represent minimums in χ^2 subject to the conditions that the two power-law slopes are continuous at the break point and disagree by more than 1-σ. The first and second break points are denoted by t_1 and t_2, respectively. The temporal decay indices ($S_\nu \propto t^{\alpha_i}$) are α_A for $t < t_1$, α_B for $t_1 < t < t_2$, and α_C for $t > t_2$.

its poor phase stability. The flux densities were determined by performing a local parabolic fit to the peak closest to the known position of the source. The NMA observations were performed at 102 GHz in D-configuration (the most compact configuration) on 4 January 2005, and in AB configuration (longest baseline configuration) on 12, 13 January 2005. We used NRAO530 for the phase calibration, and assumed it to have a flux density of 2.3 Jy.

We summarize in Table 3.3 the power-law fits to the decay of the lightcurve of the radio transient.

3.1.2 Further Discussion of Source Size Measurements

The source sizes, listed in Table 3.2, were measured by modeling the calibrated visibilities with the model-fitting procedure in DIFMAP. This procedure employs the Levenberg-Marquardt non-linear least squares minimization technique while fitting a 6 parameter elliptical Gaussian model to the visibilities. The errors were deter-

mined with DIFWRAP using the following scheme: the source size parameters were stepped in small increments around their best-fitted value to form a grid of values. At each grid point, the source size parameters were held fixed while the other model parameters were allowed to 'relax' with 4 model-fitting rounds. The 95% confidence limits were determined by those models that had a $\Delta\chi^2 < 12.8$ as measured from the best-fit total χ^2 (Press et al. 1992). As a check we used phase only self-calibration as well as phase and amplitude self-calibration, both of which give consistent source size measurements. We also used 30 second time-averaged data sets (to reduce the number of degrees of freedom), and found the best-fit model parameters agreed to within the errors.

Chapter 4

Variability of Nineteen Millisecond Pulsars in 47 Tucanae with *CHANDRA*/HRC-S†

Abstract

We present results from our 830 ksec observation of the globular cluster 47 Tucanae with the *Chandra X-ray Observatory's* High Resolution Camera-S. We limit our analysis here to the 19 previously known, localized millisecond pulsars (MSPs) in the cluster. This work more than doubles the sample of X-ray-detected MSPs observed with sensitivity to rotational variability; it is also the first survey of a large group of radio-discovered MSPs for which no previous X-ray pulsations have been detected and is therefore an unbiased survey of the X-ray properties of radio-discovered MSPs. We find that only 47 Tuc D, O and R show significant pulsations at the $\gtrsim 4$-σ level, but there is statistical evidence for rotational variability in five additional MSPs. Furthermore, we constrain the pulsed magnetospheric emission of 7 more MSPs using Monte Carlo simulations. The result is that the majority of the 47 Tuc MSPs are characterized by low pulsed fractions, $\lesssim 50\%$. In cases where larger pulsed fractions are measured the folded pulse profiles show relatively large duty-cycles. When considered with previous spectroscopic studies, this suggests that the X-ray emission arises from the neutron star's heated polar caps, and in some cases, from intra-binary shocks,

†A version of this chapter has been published as Cameron *et al.* 2007, ApJ, 660, 587.

but generally not directly from the star's magnetosphere. We discuss the impact of these results on our understanding of high energy emission from MSPs.

4.1 Introduction

Millisecond pulsars (MSPs) are old neutron stars spun-up by accretion of mass and angular momentum from the matter of a donor binary companion (Alpar et al. 1982). When compared to the canonical radio pulsar population they are distinguished by short spin periods, $P \lesssim 25\,\mathrm{ms}$, small spin-down rates, $\dot{P} \gtrsim 10^{-20}\,\mathrm{s/s}$, and thus low inferred dipole magnetic field strengths, $B_{\mathrm{dipole}} \propto (P\dot{P})^{1/2} \sim 10^{8-10}\,\mathrm{G}$, with large characteristic ages, $\tau \equiv P/2\dot{P} \gtrsim 1\,\mathrm{Gyr}$. Studies of the ≈ 150 known MSPs are difficult at wavebands outside of the radio due to their intrinsic faintness. The vast majority ($\approx 80\%$) of MSPs have binary companions that dominate at optical wavelengths, thus X-rays are an important avenue for studying MSPs.

Currently, only 16 MSPs outside of 47 Tucanae (NGC 104, hereafter 47 Tuc) have been detected in X-rays, and only 12 of these have been observed with sufficient time resolution to explore variability on rotational timescales (see Table 4.1). There are several proposed physical mechanisms capable of generating X-rays from these MSPs. Non-thermal emission processes in the neutron star magnetosphere generate power-law components in their X-ray spectra with characteristic photon indices $\Gamma \approx 1.5$–2. Pulsars in this class (e.g., PSRs B1937+21 and B1821−24A; those above the first horizontal line in Table 4.1) have large spin-down energies ($\dot{E} \gtrsim 10^{35}$ erg s^{-1}), bright X-ray emission ($L_X \gtrsim 10^{32}$ erg s^{-1}), low duty-cycles and pulse profiles that closely resemble the radio emission in morphology and phase with large pulsed fractions, $f_p \gtrsim 50\%$ (see §4.3.1). Power-law spectral components can also be produced when the wind from the MSP interacts with material from the binary companion causing an intra-binary shock. These pulsars have similar properties to those above, with the exception that they lack strong rotational modulation (e.g., the 'black widow' pulsar, PSR 1957+20). Finally, heating of the neutron star polar cap by the bombardment of relativistic particles provides a mechanism for producing thermal X-ray emission.

MSPs dominated by thermal spectra (e.g., PSRs J0437−4715, J2124−3358; most of those below the first horizontal line in Table 4.1) are characterized by lower spin down energies ($\dot{E} \lesssim 10^{34}$ erg s^{-1}), lower X-ray luminosities ($L_X \lesssim 10^{32}$ erg s^{-1}) and pulse profiles with large duty-cycles. As seen in Table 4.1, the pulsed fractions of these MSPs are usually poorly constrained, but generally show $f_p \approx 50\%$. The emission of thermal cooling X-rays from the neutron star surface and those from pulsar wind nebulae are not thought to be important for these old objects, so we will not consider them here.

The unprecedented spatial resolution of *Chandra* has enabled detailed studies of MSPs in globular clusters. Observations of M28, M4, NGC 6397, M30, and others have provided the first census of low-luminosity X-ray sources in these clusters (Rutledge et al. 2004; Becker et al. 2003; Bassa et al. 2004; Grindlay et al. 2002; Ransom et al. 2004). However, the largest endeavor has been *Chandra's* observing campaign of 47 Tuc (Grindlay et al. 2001, 2002; Heinke et al. 2005; Bogdanov et al. 2006). This work has shown that the spectral characteristics of the 47 Tuc MSPs are relatively homogeneous. Their luminosities fall in a narrow range, $L_X \approx 10^{30-31}$ erg s^{-1}, and are well described by thermal spectral models with small emission radii, $R_{\rm eff} \approx$ 0.1-3 km and temperatures of $T_{\rm eff} \approx$1–3$\times 10^6$ K. The only exceptions are the radio-eclipsing binaries 47 Tuc J, O and W, which require additional power-law components above 2 keV with $\Gamma \approx 1.0$–1.5. These results are reinforced by the findings of detailed spectroscopic studies by *Chandra* and *XMM-Newton* that have emphasized the dominant thermal components in nearby MSP X-ray spectra over the fainter power-law features (Zavlin et al. 2002; Zavlin 2006). Consequently, we expect the predominant X-ray emission from the MSPs in 47 Tuc to arise from heated polar caps, and to be modulated just by rotating a small area relative to the observer (i.e., sinusoidal pulse profiles; Grindlay et al. 2002; Cheng & Taam 2003; Bogdanov et al. 2006).

In this paper, we present high-time resolution data capable of exploring the fast time variability of the X-ray counterparts to the 47 Tuc MSPs. In § 4.2 we present the details of the observations and data reduction, followed by the variability analysis (§ 4.3) and an examination of the accuracy of the HRC-S time tags (§ 4.4). We

find that the HRC-S remains capable of detecting fast modulation, but the MSPs in 47 Tuc lack strong variability on all timescales probed. We discuss the impact of this result on our understanding of the X-ray emission from MSPs in § 4.5.

4.2 Observations and Data Reduction

Observations of 47 Tuc were performed with *Chandra's* HRC-S detector (Zombeck et al. 1995; Murray et al. 1998). They began 2005 Dec 19 7:20 UT with 14 subsequent visits over the next 20 days for a total of 833.9 ksec of exposure time (see Table 4.2 for a summary). The observing plan of dividing the 833.9 ksec into 50–100 ksec visits spread out over 20 days was adopted – instead of the optimal choice for pulsar detection of an uninterrupted observation – to mitigate a thermal limitation in spacecraft operations. The HRC-S has a timing resolution of 15.625 μs in the nominal energy range of 0.1-2 keV, although it has essentially no energy resolution. The data were analyzed using Chandra Interactive Analysis of Observations[1] software (CIAO) version 3.3 and CALDB version 3.2.1.

We began the data analysis of each observation by registering it to the first pointing (ObsID 5542) using the relative astrometry of the four brightest sources in the field. These corrections typically resulted in $\lesssim 0.5''$corrections to the native astrometry. Data were filtered on a pulse invariant (PI) channel to maximize the signal-to-noise ratio (SNR) for the known MSPs using the following approach. We compared the PI channel distribution of all counts extracted from regions corresponding to the known MSPs with that extracted from a background region. The background and source PI distributions are identical below PI = 25 (within 1% in counts/area). Above this value the source region counts are significantly in excess, so we adopt PI = 25 as the lower PI limit for background filtering. We determined the upper-limit in PI channel by maximizing the total source SNR, therby finding the maximum when data at PI $>$ 120 are excluded from analysis. Thus, we adopt a PI range of 25–120 for all analyses; this decreases the MSP source count rates by 6%, while excluding

[1] http://cxc.harvard.edu/ciao/

51% of the total background counts. The resulting background contribution is 17.9 counts arcsec^{-2} over the entire observing span.

Currently, positions are known for 19 of the 22 MSPs in 47 Tuc. Published pulsar timing solutions can account for 16 of these positions (Freire et al. 2001, 2003), while 47 Tuc R and Y have unpublished solutions (Freire et al. in preparation). 47 Tuc W has only a preliminary timing solution, but was localized by the eclipses of its optical counterpart (Freire et al. unpublished; Edmonds et al. 2002). The close proximity of pulsars 47 Tuc G and I and 47 Tuc F and S (separations 0.12″and 0.7″, respectively) do not allow them to be resolved by *Chandra*, so their counts must be considered jointly. For analysis purposes we attribute 50% of detected photons to each pulsar (see §4.3.1).

We extracted photons from within circular regions surrounding each of the known MSP positions. The size of each extraction region can be found in Table 4.3. The radius was chosen adaptively in order to maximize SNR, but constrained to mitigate contamination by nearby objects. However, some contamination due to source crowding is unavoidable. We estimate this contribution by modeling the PSF as a Gaussian with $\sigma = 0.29''$, calculating the number of photons that fall in the extraction region of a given source from each neighboring source, and using this estimate to update the extracted source counts. We iterate this procedure until we have an estimate of the source crowding contamination for all sources in the field. This analysis shows that the contamination is negligible ($< 1\%$ of extracted counts) for all MSPs except O and R, which each have ~ 13 additional background counts due to nearby sources. We include these in our estimate of their backgrounds in the subsequent analysis (Table 4.3). Assuming these background estimates, we detect sources at each of the 17 independent pulsar positions with > 5-σ significance.

Throughout the analysis we assume a distance of 4.85 kpc to 47 Tuc (Gratton et al. 2003). We apply an energy correction factor of 5.044×10^{-12} erg cm^{-2} s^{-1} or 1.42×10^{34} erg s^{-1} (0.5-2.0 keV) per 1 HRC-S count/sec, which is the unabsorbed X-ray flux assuming N_{H_2}=1.3×10^{20} cm^{-2} and blackbody emission with a temperature

of 0.178 keV as determined from WebPIMMS[2] (Bogdanov et al. 2006). In addition to the extraction region size, we list the total counts extracted, expected background counts and the time averaged luminosity in Table 4.3.

4.3 Variability Analysis

Prior to the timing analysis, we use the CIAO tool `axbary` to convert the event times to the solar system barycenter using the JPL DE200 solar system ephemeris, the *Chandra* orbital ephemeris, and the radio/optical position of each MSP (see § 4.2).

4.3.1 Rotational Variability

We calculated the rotational phase of each arriving photon for each MSP using the latest radio ephemerides corrected to X-ray frequencies (Freire et al. 2003; Freire et al., in preparation). The resulting phases were searched for variability with the Z_n^2-test (Buccheri et al. 1983), where n is the optimal number of harmonics as determined from the H-test (de Jager et al. 1989). The variable Z_n^2 has a probability density function distributed as χ^2 with $2n$ degrees of freedom. We list the value of this variable, the detection significance in equivalent Gaussian σ and n in Table 4.3. Only 47 Tuc D, O and R show variability above the ≈ 4-σ level. Their folded pulse profiles are shown in Figure 4.1. All three pulsars' profiles are characterized by large duty-cycles. 47 Tuc O shows evidence for two peaks centered at phases, $\phi \approx 0.0$ and $\phi \approx 0.4$ with widths of $\delta\phi \approx 0.2$ and $\delta\phi \approx 0.4$, respectively. Only a single peak is evident in the profiles of 47 Tuc D and R centered at $\phi \approx 0.45$ with $\delta\phi \approx 0.25$ and $\phi \approx 0.5$ with $\delta\phi \approx 0.3$, respectively.

As seen in Table 4.3, 5 of the 19 MSPs are detected with marginal significance, 2.8–3.3-σ. Given the relatively large size of our MSP sample, we can quantify the significance of these marginal detections. We are free to choose the significance level with which we call an MSP 'variable'. Once we choose this level, the problem becomes one of binomial statistics where each MSP represents an independent measurement

[2]http://heasarc.gsfc.nasa.gov/Tools/w3pimms.html

for variability. Choosing the 99% percent confidence level for Z_n^2 (corresponding to 2.58-σ) allows us to identify 8 'variable' sources when only ≈ 0.2 are expected if the MSPs were drawn from a random distribution. The probability of 8 of 19 trials being labeled 'variable' is 6.7×10^{-12}. The probability of one or more of these being false detections is 17.4%. Since the confidence level at which we label an MSP as 'variable' is arbitrary, we list a range of confidence levels and the number of corresponding detections with the binomial and false detection probabilities in Table 4.4. For the remainder of our analysis, we will adopt the 99% confidence level. This results in 47 Tuc D, E, F, H, O, Q, R, and S being labeled as 'variable.' Their profiles are shown in Figure 4.1.

The pulsed fraction, f_p, for each MSP can be determined using two steps. First, we estimate the DC (unpulsed) level with the non-parametric bootstrapping method of Swanepoel et al. (1996). The advantage of this technique is that it works on the raw phases without the need to construct a phase histogram or know the pulse shape a priori. This level is shown by the solid line in Figure 4.1 with ±1-σ errors. Next, we correct for the fact that the DC component includes both unpulsed photons from the MSP and background photons. Note that for MSPs F and S we consider 50% of the background subtracted source counts to be unpulsed background photons. The expected background contribution to the pulse profile is denoted by the dashed line in Figure 4.1 (see § 4.2). The pulsed fraction determined by the bootstrapping method can be related to the true pulsed fraction by $f_p = f_{p,\mathrm{boot}} N_t/(N_t - N_b)$, where $f_{p,\mathrm{boot}}$ is the pulsed fraction determined by the bootstrapping method, N_t is the total number of extracted counts, and N_b is the total number of background counts contributing to N_t. Both N_t and N_b can be found in Table 4.3. The pulsed fractions derived in this manner are also listed in Table 4.3.

We calculate upper limits on the pulsed fractions of the remaining 11 MSPs with timing solutions (note that W has only a preliminary solution) with Monte Carlo simulations assuming two scenarios. First, we make the conservative assumption that the underlying pulse shape is sinusoidal. For each MSP and pulsed fraction, we simulate 500 light curves with a total number of counts $N_t = N_b + N_s$, where N_s

is the number of source counts. If the pulsed fraction is $f_{p,\mathrm{sine}}$, then N_s consists of $(1 - f_{p,\mathrm{sine}})N_s$ unpulsed counts and $f_{p,\mathrm{sine}}N_s$ pulsed counts. For the two unresolved MSPs that do not show pulsations (G and I), we assume that 50% of the source photons constitute an unpulsed background. We determine the 90% confidence upper limit on the pulsed fraction as the value of $f_{p,\mathrm{sine}}$ at which 450 synthetic light curves have values of $Z_1^2 \gtrsim 27.4$ (corresponding to 5-σ). The result is that only J, L, W and Y have sufficient counts to be constrained in this way.

Motivated by the close correspondence of the radio and X-ray pulse profiles of magnetospherically dominated MSPs (see § 4.1), we determine a second set of upper limits based on the assumption that the underlying X-ray pulse has the same morphology as the radio pulse. We denote this pulsed fraction as $f_{p,\mathrm{radio}}$. In the case of the weak radio pulsars, N, R, T, W, and Y it was necessary to model the radio pulse(s) with Gaussians and use these as the assumed X-ray pulse shape. The radio pulse profiles for remaining MSPs have sufficient signal-to-noise to be used directly. We then perform the Monte Carlo simulations with the technique described above to determine the 90% confidence upper limits. The results can be found in Table 4.3. It is possible to constrain the X-ray emission with the same morphology as the radio pulse from 7 pulsars in this way.

4.3.2 Orbital Variability

The orbital periods of the 12 binary 47 Tuc MSPs span the range 0.07–2.4 days. In order to search for variability during these orbits, we calculated the orbital phase of each arriving photon for each MSP and constructed histograms with 5, 10 and 20 bins. We then corrected each bin for the variation of exposure time during that particular orbital phase so that we have a histogram of counts per second per bin and subtracted the expected background contribution. We search for variability by computing χ^2 between the histogram and a constant count rate. We found that none of the 47 Tuc binary MSPs showed significant orbital variability.

Substantial X-ray eclipses, characterized by a complete disappearance of hard

($> 2\,\mathrm{keV}$) photons and a decline in soft ($< 2\,\mathrm{keV}$) photons for $\approx 30\%$ of the orbit, have been reported for 47 Tuc W (Bogdanov et al. 2005). Thus, the lack orbital variability in 47 Tuc W is surprising. We reduced archival ACIS-S data of 47 Tuc W from ObsIDs 2735, 2736, 2737, and 2739 in order to quantify the properties of the eclipse in the HRC-S bandpass. We reprocessed the level 1 event files to make use of the latest calibration and filtered periods of high background flaring (i.e., periods with count rates > 3-σ above the mean full-frame rate). This resulted in 251.3 ksec of exposure time. We computed the orbital phase of each photon within a $1''$ radius of the position of 47 Tuc W in the energy range 0.3–2.0 keV with the preliminary timing solution (see § 4.2). The X-ray eclipse is evident in the histogram shown in Figure 4.2a at phase, $\phi \approx 0.2$, where $\phi = 0$ at the time of the ascending node. This X-ray eclipse timing agrees well with observed radio eclipse from $\phi = 0.1$–0.4 (Camilo et al. 2000; Edmonds et al. 2002). The variability is significant at the 4.3-σ level from the measured value of $Z_1^2 = 30.1$ and we determine an orbital modulation of $f_p = 36 \pm 9\%$ using the non-parametric bootstrap method (see § 4.3.1). This is consistent with the 90% confidence limit of $f_{p,\mathrm{sine}} < 48\%$ on a sinusoidal signal in the HRC-S time series of 47 Tuc W (see § 4.3.1).

4.3.3 Aperiodic Variability

To search for aperiodic variability in the 47 Tuc MSPs, we have applied the Bayesian blocks algorithm of Scargle (1998) as implemented by the Interactive Spectral Interpretation System (ISIS; Houck & Denicola 2000). The algorithm determines the optimal decomposition of the light curve into constant count rate segments based on a parametric maximum likelihood model of a Poisson process. The raw (unbinned) events are divided into 'blocks' and the odds ratio that the count rate has varied is computed. If variability is found, each 'block' is further subdivided to characterize the structure of the light curve (e.g., step-function variation, flaring, etc.). We could not identify any intra-observation variability from 17 MSPs using an odds ratio corresponding to a 68% chance that any variability is real. In addition, the

inter-observation count rates for each MSP derived from this process do not show significant variability over the ≈ 20 day span of our observations. Thus, the X-ray emission from the 47 Tuc MSPs is stable on timescales ranging from minutes to days.

4.3.4 ACIS-S vs. HRC-S Comparison

With such a large sample of constant luminosity X-ray sources, we can compare the count rates between the ACIS-S and HRC-S for soft thermal sources. In Figure 4.3, we compare the count rate for the two detectors using each of the 17 independent MSP detections. For the ACIS-S count rate, we summed the values in the 0.3–0.8 keV and 0.8–2.0 keV bands listed by Heinke et al. (2005). The relation between count rates in the two different detectors was $I(\mathrm{HRC-S}) = (0.43 \pm 0.024) \times I(\mathrm{ACIS-S})$. This is consistent with the conversion from HRC-S to ACIS-I (Rutledge et al. 2004).

4.4 HRC-S Timing Accuracy

The accuracy of the HRC-S time tags was demonstrated to be ± 12 μs in an observation of M28 (Rutledge et al. 2004). We investigated several issues to ensure that the HRC-S has sufficient accuracy to detect MSPs. In addition to accounting for a leap second that occurred during the middle of the observing span, we examined the effect of telemetry saturation, different solar system ephemerides, and analyzed a recent calibration observation of the globular cluster M28.

4.4.1 Telemetry Saturation

The maximum telemetered full-field, unfiltered count rate for the HRC-S is 184 counts s^{-1}(*Chandra* Proposers' Observatory Guide [3]). At rates above this, a decreasing fraction of all counts will be telemetered. The data will be affected if this count rate is exceeded during the 2.05 s full-frame readout time. The effect of telemetry saturation on timing certainty is that, when telemetry is saturated, not all events are

[3] http://cxc.harvard.edu/proposer/POG/index.html

telemetered back to Earth. Due to the HRC wiring error (Tennant et al. 2001), the Nth event detected by the HRC-S has its time assigned to the N+1st event[8]. The true time series can be reconstructed if both are telemetered; if either is not, then the wrong time will be assigned to one event (either the Nth event, or the $N-1$st event).

To test the extent to which this saturation impacts our observations, we constructed a light curve of our entire dataset binned in 2.05 s intervals. We found that only $\approx 0.1\%$ of the bins exceeded the maximum count rate. Thus telemetry saturation will effect only $\approx 0.1\%$ of the counts in any given MSP, which is negligible.

4.4.2 Ephemeris Comparison

We performed a preliminary extraction of data using DE405 and compared the timing precision of data corrected to DE200 using one of the brightest sources in the field. We found the entire observational period was offset by $t_{\rm DE405} - t_{\rm DE200} = 1.3809$ ms at the start of the observational period, decreasing monotonically to 1.3719 ms at the end of the observation period. Thus, there was an average direct offset between the photon time-of-arrivals (TOAs) in the two ephemerides of $\approx$1.3764 ms, and a range of variation of $\approx 9\,\mu s$. This $9\,\mu s$ therefore amounts to the relative timing uncertainty due to the adopted ephemeris, comparable to the uncertainties in HRC digitization ($\pm 5\,\mu s$) and Chandra clock stability ($\pm 5\,\mu s$) (Rutledge et al. 2004).

4.4.3 Spacecraft Clock Stability

A calibration observation of PSR B1821−24A was performed on May 27, 2006 starting at 12:30 UT for 40887 sec in order to evaluate the stability of the HRC-S clock. A complete analysis is beyond the scope of this work. However, a search of the data using the known radio timing ephemeris (Rutledge et al. 2004) clearly detects the 3.05 ms pulsar with $Z_1^2 = 330$ corresponding to a detection significance of $\approx$ 18-σ. Thus, we conclude the HRC-S clock has remained sufficiently stable to detect MSPs.

4.5 Discussion and Conclusions

Chandra HRC-S observations of 47 Tuc have allowed us to study a relatively large sample of 19 MSPs on millisecond to week timescales. We find that the MSPs in 47 Tuc uniformly show very low levels of variability on all scales probed. We have sufficient statistics to meaningfully constrain (under the assumption that their X-ray pulse profiles match the radio) or measure the rotational modulation of 15 MSPs. Eight of these objects have low pulsed fractions, $f_p \lesssim 50\%$. MSPs 47 Tuc D, O, and R each have pulsations detected at $\gtrsim 4$-σ significance with relatively large pulsed fractions, $f_p \gtrsim 60\%$, which are similar to the levels seen from luminous MSPs dominated by non-thermal emission (e.g., PSRs B1821−24A and B1937+21). However, the pulse profiles of these objects (see Figure 4.1) are characterized by large duty-cycle features that do not resemble the sharp, low duty-cycle profiles seen in the non-thermal MSPs (e.g., see Becker & Aschenbach 2002).

The existing ACIS data show that the 47 Tuc MSPs have fairly homogeneous spectroscopic properties (Grindlay et al. 2002; Bogdanov et al. 2006). All but 3 of the 47 Tuc MSPs are characterized by 1–3$\times 10^6$ K thermal spectra with low luminosities in a narrow range, $L_{\rm X} \approx 10^{30-31}$ erg s^{-1}, and have small emission radii, $R_{\rm eff} \approx 0.1$–3.0 km. The low level of measured variability presented here indicates that rotational averaging does little to affect these values, which agree with the predictions of polar cap heating scenarios (Harding & Muslimov 2002). Thus we conclude that, unlike the luminous non-thermal MSPs, the vast majority of the X-ray emission from the 47 Tuc MSPs is created by the heating of the neutron star polar cap by a return current of relativistic particles produced in the magnetosphere (Arons 1981; Harding & Muslimov 2001, 2002; Grindlay et al. 2002; Bogdanov et al. 2006). For older MSPs with very short spin periods and low magnetic fields, like those in 47 Tuc, the main source of the $e^{\pm}$-pair production is thought to be through inverse Compton scattering of thermal X-rays from the neutron star surface off of electrons in the pulsar magnetosphere (Harding & Muslimov 2002).

Only the radio-eclipsing binaries 47 Tuc J, O, and W show power-law spectral

components that contribute significantly (70%, 50% and 75%, respectively) to their total flux (Bogdanov et al. 2006). The lack of strongly pulsed emission in 47 Tuc J and W suggests that the X-ray emission does not arise in the neutron star magnetosphere, but instead is likely the consequence of an intra-binary shock. This is in agreement with conclusions based on orbital phase resolved spectroscopy of 47 Tuc W by Bogdanov et al. (2005). Conversely, the current data do not conclusively identify the origin of X-rays from 47 Tuc O, which shows significant pulsations. The X-rays from an intra-binary shock are not expected to be modulated at the rotational period of the MSP, so the measured pulsed fraction, $f_p = 83 \pm 21\%$, is only marginally consistent with the 50% spectroscopic allocation of X-rays due to a shock. In addition, its large duty-cycle does not immediately imply that polar cap heating is the source of the pulsed X-rays, since broadly beamed magnetospheric emission viewed off-axis would appear to have a large duty-cycle (Becker & Trümper 1999a).

The apparent non-detection of low duty-cycle pulsars is significant in comparison with the pulse profile of B1821−24A. If all 19 MSPs had X-ray pulse profiles identical to that of PSR B1821−24A, all would have been detected with $\gtrsim$ 7-σ significance (which we find for the lowest SNR MSP, 47 Tuc T). Those MSPs with higher count rates would have been detected with even greater significance. The implication is that PSR B1821−24A has an unusually low duty-cycle for a MSP. If we assume that low duty-cycle MSPs make up a fraction f of the globular cluster population, then the non-detection of even 1 such pulsar in 47 Tuc implies that B1821−24A-like pulsars comprise f <20% of the MSP population in GCs (90% confidence limit). This limit could be much lower, if the intrinsic distribution of duty-cycles in magnetospheric pulsars is lower than that of B1821−24A, for example; however, there seems to be little observational work quantifying the distribution of duty-cycles of observed pulsars.

Acknowledgements

The authors would like to thank P. Freire for providing us with data prior to publication. Support for this work was provided by NASA through Chandra Award Number

Table 4.1. X-ray Properties of Millisecond Pulsars Outside of 47 Tuc.

PSR	P (ms)	d (kpc)	τ (Gyr)	$\log \dot{E}$ ($\mathrm{erg\,s^{-1}}$)	$\log L_X$ ($\mathrm{erg\,s^{-1}}$)	f_p (%)	Refs.
B1937+21	1.56	3.57	0.23	36.04	33.15	54 ± 7	1,2
B1957+20	1.61	2.49	2.22	35.04	31.81	< 60	1,3
J0218+4232	2.32	2.67	0.48	35.38	32.54	59 ± 7	4,5
B1821−24A (M28)	3.05	5.5[a]	0.03	36.35	33.22	85 ± 3	6,7
J0751+1807	3.48	1.15	7.08	33.86	30.84	52 ± 8[b]	8,9
J0030+0451	4.87	0.32	7.71	33.53	30.40	69 ± 18	10,11
J2124−3358	4.93	0.25	6.01	33.83	30.23	56 ± 14	1,12
J1012+5307	5.26	0.84	4.86	33.68	30.38	77 ± 13[b]	13,9
J0437−4715	5.76	0.14[a]	4.91	33.58	30.47	40 ± 2	14,12
J1024−0719	5.16	0.39	27	32.93	29.30	52 ± 22	1,12
J1744−1134	4.07	0.36[a]	9.1	33.62	29.49[c]	—	1,3
J0034−0534	1.88	0.54	6.03	34.48	29.60[c]	—	12
No High Time Resolution Imaging							
B1620−26 (M4)	11.08	1.73[a]	0.26	34.28	30.08[c]	—	15,16
J1740−5340 (NGC 6397)	3.65	2.55[a]	0.34	35.15	30.9[c]	—	17,18
J1911−6000C (NGC 6752)	5.28	4.1[a]	38.1	32.77	30.34[c]	—	19
J2140−2310A (M30)	11.02	9.0[a]	>0.08	<34.79	30.64[c]	—	20

[a]Accurate distance measurement.

[b]Detection significance is low.

[c]X-ray luminosity in the 0.5–2.5 keV band.

Note. — All distances are estimated from the pulsar dispersion measures and the model of Galactic distribution of free electrons (Cordes & Lazio 2002), except where noted. X-ray luminosities are quoted in the 0.2–10 keV band as adopted from Table 1 of Zavlin (2006) and references therein, except where noted. Pulsed fractions are quoted roughly in the HRC-S band (0.1–2.0 keV), but see references for the specific bandpass. The spectra of MSPs above the first horizontal line are dominated by non-thermal X-ray emission. Those below the line have significant thermal components or are indeterminate (and thus presumed to be thermal) in nature. References: 1 – Toscano et al. (1999), 2 – Nicastro et al. (2004), 3 – Becker & Trümper (1999b), 4 – Navarro et al. (1995), 5 – Webb et al. (2004a), 6 – Becker et al. (2003), 7 – Rutledge et al. (2004), 8 – Nice et al. (2005), 9 – Webb et al. (2004b), 10 – Lommen et al. (2000), 11 – Becker & Aschenbach (2002), 12 – Zavlin (2006) 13 – Lange et al. (2001), 14 – Zavlin et al. (2002), 15 – Thorsett et al. (1999), 16 – Bassa et al. (2004), 17 – D'Amico et al. (2001), 18 – Grindlay et al. (2002), 19 – D'Amico et al. (2002), 20 – Ransom et al. (2004).

G05-6060 issued by the Chandra X-ray Observatory Center, which is operated by the Smithsonian Astrophysical Observatory for and on behalf of NASA under contract NAS8-03060. L. B. acknowledges support from the NSF through grant PHY99-07949.

Table 4.2. HRC-S Observations of 47 Tuc.

ObsID	Obs. Start (UT)	Obs. Start (MJD)	Exp. Time (sec)
5542	2005 Dec 19.29	53723.79	51918.2
5543	2005 Dec 20.62	53725.12	53962.6
5544	2005 Dec 21.98	53726.48	52036.6
5545	2005 Dec 23.21	53727.71	54203.5
6237	2005 Dec 24.59	53729.09	51920.8
6238	2005 Dec 25.88	53730.38	50887.6
5546	2005 Dec 27.23	53731.73	51939.3
6230	2005 Dec 28.57	53733.07	52401.0
6231	2005 Dec 29.91	53734.41	48963.7
6232	2005 Dec 31.22	53735.72	49139.0
6233	2005 Jan 2.24	53737.74	103433.2
6235	2005 Jan 4.17	53739.67	51932.1
6236	2005 Jan 5.48	53740.98	54729.8
6239	2005 Jan 6.92	53742.42	52241.6
6240	2005 Jan 8.10	53743.60	54178.4

Table 4.3. HRC-S Derived X-ray Properties of the 47 Tuc Millisecond Pulsars.

Name	Total[a] Counts	Background Counts	Extraction Radius	$\log(L_X)$[b] (0.5-2.0 keV)	Harmonics[c] (n)	Z_n^{2}[c]	Significance[c] (σ)	$f_{p,\mathrm{radio}}$[c,d]	$f_{p,\mathrm{sine}}$[c,d]	f_p[c]
47 Tuc C	173	94.8	1.3	30.12	1	2.5	1.5	<76	< 100	
47 Tuc D	221	94.8	1.3	30.33	2	21.7	3.9	—	—	70 ± 21
47 Tuc E[g]	254	94.8	1.3	30.43	1	12.5	3.3	—	—	50 ± 19
47 Tuc F[e]	413	80.7	1.2	<30.75	1	10.1	2.9	—	—	2 ± 12
47 Tuc G[f]	322	80.7	1.2	<30.61	1	1.0	1.0	< 100	< 100	
47 Tuc H[g]	176	94.8	1.3	30.14	2	12.7	2.8	—	—	26 ± 20
47 Tuc I[f,g]	322	80.7	1.2	<30.61	1	6.0	2.3	<81	< 100	
47 Tuc J[g]	266	94.8	1.3	30.46	1	6.5	2.3	<38	<77	
47 Tuc L	342	35.9	0.8	30.71	2	10.0	2.4	<50	< 49	
47 Tuc M	151	94.8	1.3	29.98	1	2.2	1.4	< 100	< 100	
47 Tuc N	186	94.8	1.3	30.19	1	4.8	2.0	<73	< 100	
47 Tuc O[g]	431	94.1[h]	1.2	30.77	3	39.1	5.1	—	—	81 ± 21
47 Tuc Q[g]	186	94.8	1.3	30.19	6	28.3	3.1	—	—	83 ± 42
47 Tuc R[g]	288	80.4[h]	1.1	30.57	2	24.1	4.1	—	—	63 ± 29
47 Tuc S[e,g]	413	80.7	1.2	<30.75	8	33.4	3.1	—	—	20 ± 15
47 Tuc T[g]	133	80.7	1.2	29.94	1	1.2	1.1	< 100	< 100	
47 Tuc U[g]	193	94.8	1.3	30.22	1	0.1	0.7	< 100	< 100	
47 Tuc W[g]	433	80.7	1.2	30.77	1	0.8	1.0	<48	<48	
47 Tuc Y[g]	218	94.8	1.3	30.32	1	6.5	2.3	<40	<96	

[a] This number includes the expect background counts listed in the subsequent column.

[b] X-ray luminosity (logarithm of erg s^{-1}) derived in the band 0.5–2.0 keV.

[c] See the text (§ 4.3.1) for a description of these parameters.

[d] <100% means the undetected pulsation is consistent with 100% pulsed signal, and therefore is unconstrained by simulations.

[e] 47 Tuc F and S have overlapping positions. The total counts represent all photons extracted from the 1.2″extraction radius and the background counts are only those expected from a uniform background.

[f] 47 Tuc G and I have overlapping positions. The total counts represent all photons extracted from the 1.2″extraction radius and the background counts are only those expected from a uniform background.

[g] Binary MSP.

[h] Includes an estimate of the contamination due to source crowding (see § 4.3.1).

Table 4.4. Summary of 47 Tuc MSP Detection Significance.

Pulsation Detection Threshold (1)	Number of Detections (2)	Binomial Probability (3)	False Detection Probability (4)
99%	8	6.9×10^{-12}	17.5%
99.73%	6	1.0×10^{-11}	5%
99.947%	3	1.4×10^{-7}	1%

Note. — (1) – Confidence level of Z_n^2 above which a 47 Tuc MSP is labeled 'variable.' (2) – The number of 'variable' MSPs for the given confidence level. (3) – The binomial probability that the number of 'variable' MSPs is due to chance. (4) – The probability that one of the 'variable' MSPs is a statistical fluctuation.

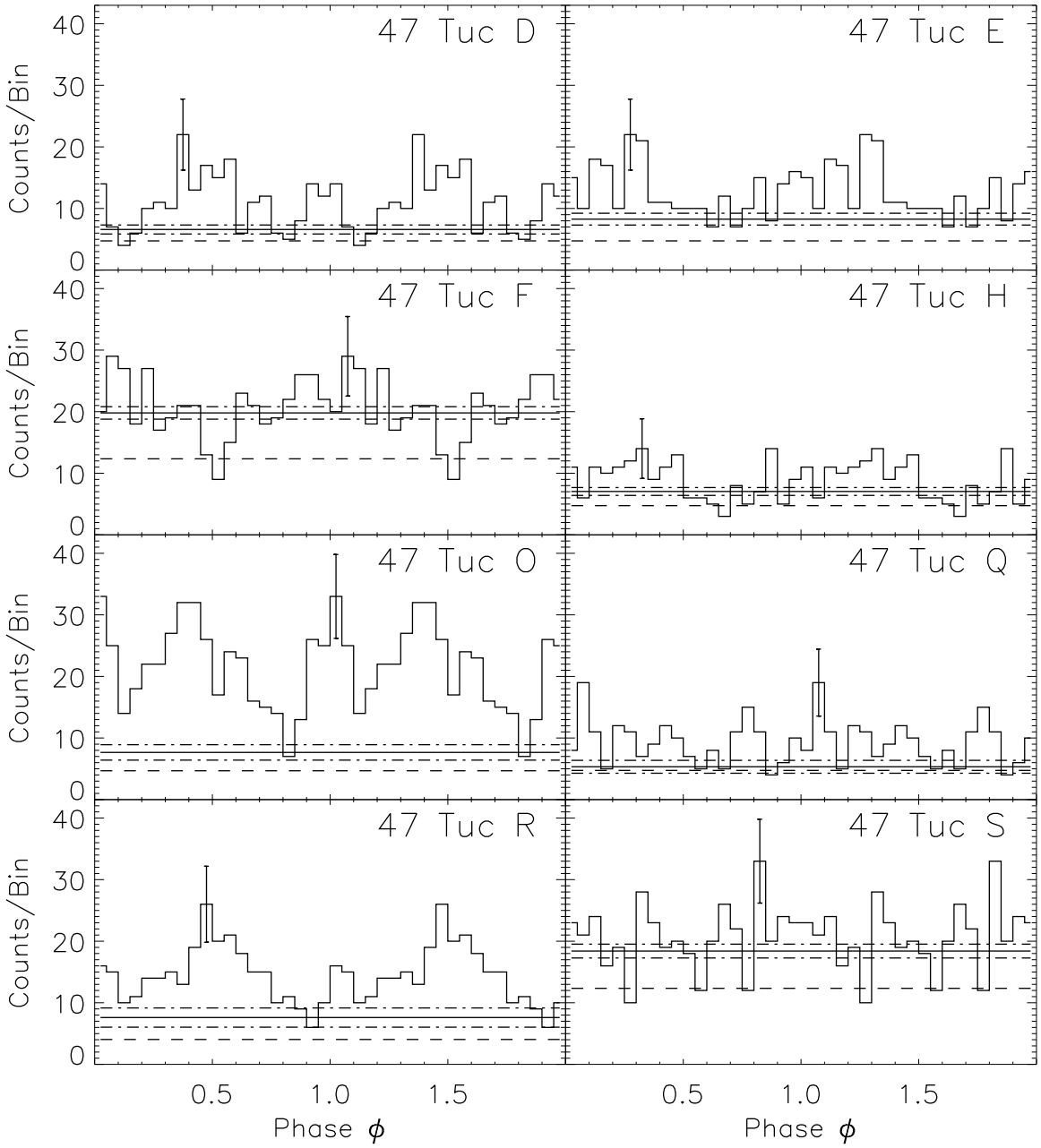

Figure 4.1 Pulse profiles of the variable 47 Tuc MSPs with a typical error bar (two periods are shown for clarity). The histograms were constructed with 20 bins per period. The solid horizontal line denotes the DC (unpulsed) contribution to the pulse profile as determined by the nonparametric bootstrapping algorithm with the associated 1-σ uncertainties denoted with dashed-dotted lines. The dashed line denotes the estimated contribution to this level due to the uniform background and source crowding (50% of the background subtracted counts are attributed to this total for MSPs F and S; see § 4.3.1 for details).

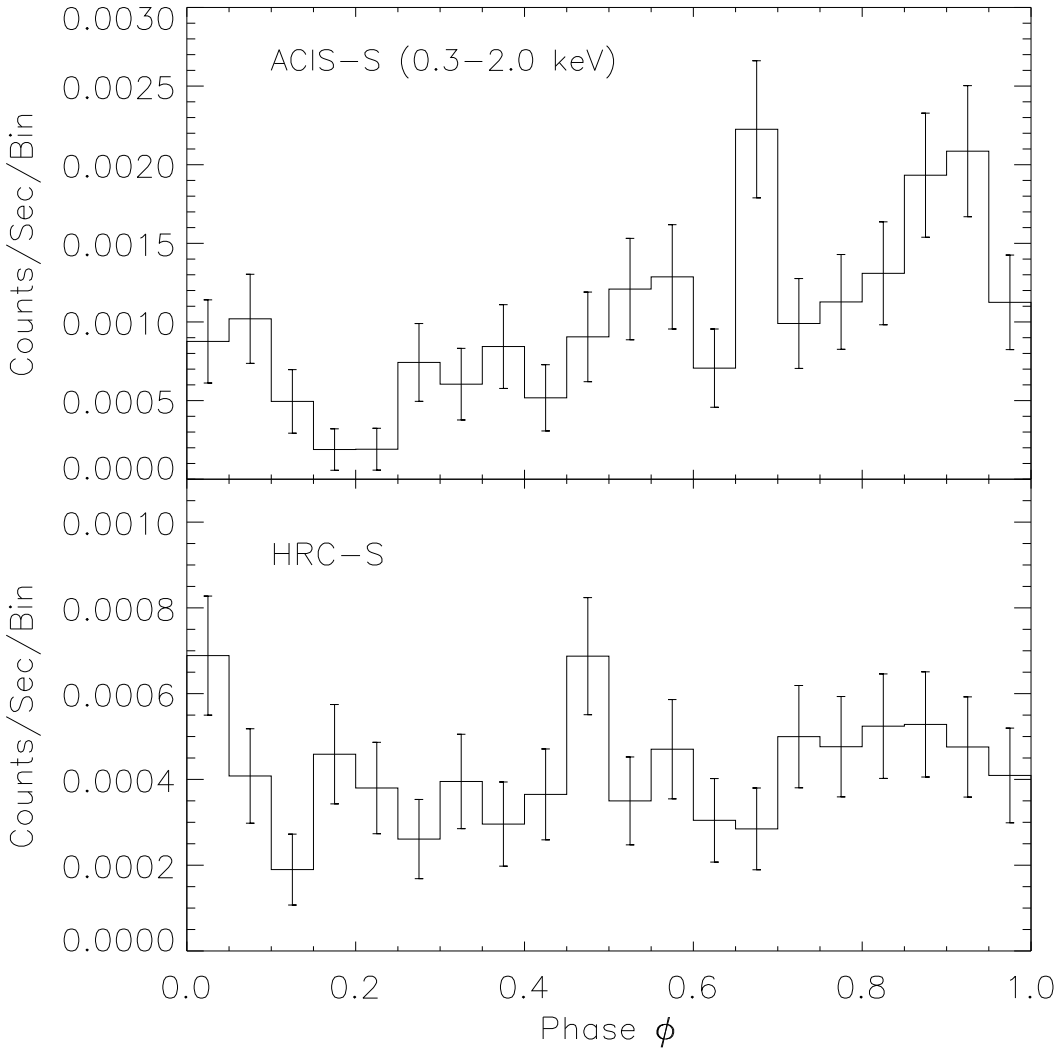

Figure 4.2 Orbital Profiles of 47 Tuc W from ACIS-S (upper) and HRC-S (lower). The error bars are 1-σ and histograms contain 20 bins per period.

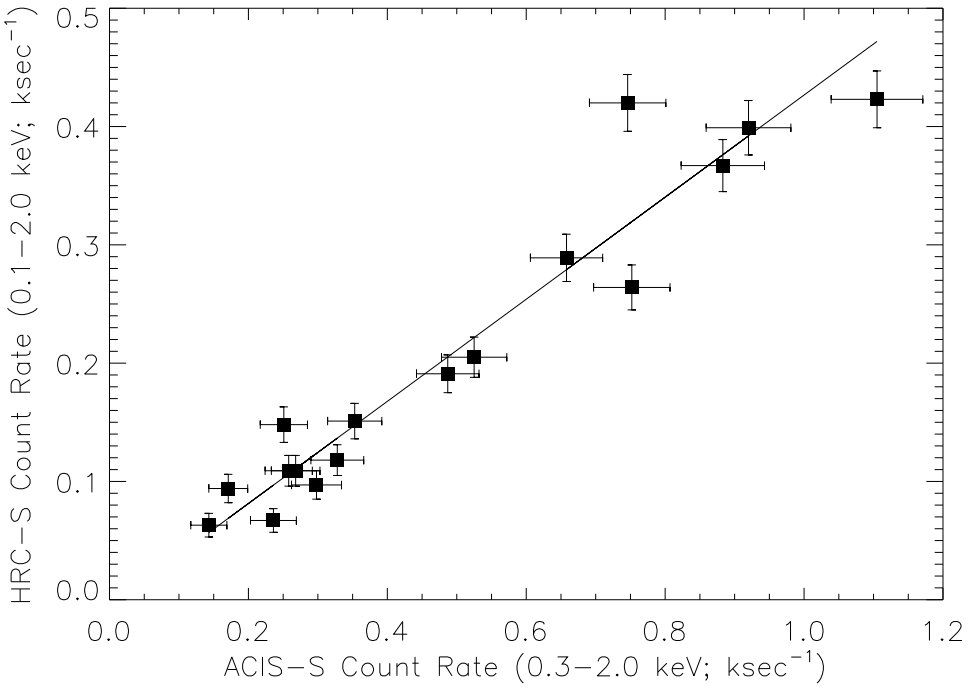

Figure 4.3 HRC-S/ACIS-S count rate comparison using the 17 independent 47 Tuc MSP detections. The line represents the best linear fit to the data.

Chapter 5

Near-Infrared and X-ray Observations of the Enigmatic G70.7+1.2[†]

Abstract

We present high resolution imaging of the puzzling radio and optical nebula G70.7+1.2 with the Keck Observatory's laser guide star adaptive optics (LGS-AO) system and the *Chandra X-ray Observatory*. The archival X-ray observations show a hard ($\Gamma \approx 1.8$), low luminosity ($L_X \approx 4 \times 10^{31}$ erg s^{-1}) point source at the center of the nebula. Follow-up LGS-AO near-infrared imaging of the *Chandra* error circle reveals a relatively bright ($K' \approx 14$ magnitude) counterpart. Both its color and brightness are consistent with a heavily obscured B-star or possibly a late-G/early-K giant. The most plausible explanation is that this newly discovered X-ray source is a non-accreting B-star/pulsar binary powering the radio and optical nebula. If so, the luminous Be-star, discussed in the literature, seemingly embedded in the nebula is not the dominant force responsible for shaping G70.7+1.2. Thus, we suggest that G70.7+1.2 is the result of two unrelated objects (a B-star X-ray binary and a Be star) interacting with a dense molecular cloud. With this explanation we believe we have solved the mystery of the origin of G70.7+1.2.

[†]A version of this chapter has been published as Cameron *et al.* 2007, ApJ Letters, 665, 135.

5.1 Introduction

G70.7+1.2 is a compact ($\approx 20''$) radio and optical nebula in the Galactic Plane whose origin is controversial (Reich et al. 1985; Green 1986; de Muizon et al. 1988; Bally et al. 1989). The shell-like radio morphology is accompanied by broad, blue-shifted [O I] and [S II] emission lines indicative of an interstellar shock (de Muizon et al. 1988; Kulkarni et al. 1992). Millimeter CO emission traces this radio and optical emission, suggesting the shock is interacting with molecular material (Bally et al. 1989; Phillips et al. 1993; Onello et al. 1995). In addition, a bright near-infrared (NIR) star appears to be embedded in G70.7+1.2, and it is surrounded by a strong Hα reflection of spectral type Be (Becker & Fesen 1988; Kulkarni et al. 1992).

Ironically, it is the plethora of clues that make G70.7+1.2 a perplexing object, despite its discovery more than six decades ago (Minkowski 1948). G70.7+1.2 is unique in that nearly every Galactic prototype has been proposed to explain it: young supernova remnant, nova shell, stellar wind bubble, H II region and Herbig-Haro-like outflow (Reich et al. 1985; de Muizon et al. 1988; Green 1986; Becker & Fesen 1988). However, none of these can explain the low expansion velocities and the non-thermal radio emission. The only currently proposed consistent theory to explain these properties is one in which the bright Be-star is paired with an unseen neutron star to form a Be-radio pulsar binary moving supersonically through the dense gas (Kulkarni et al. 1992). In this model, significant mass loss from the luminous Be-star inflates a bubble which is filled by a mixture of the stellar wind with energetic particles and magnetic field from the pulsar. This combination creates the non-thermal radio emission coincident with the optical bow shock of the medium surrounding the system. This model makes the prediction that an X-ray source or pulsar should be seen coincident with the embedded Be-star.

We report on archival X-ray and new Keck LGS-AO observations that reveal an X-ray source with a NIR counterpart in the center of G70.7+1.2 which is unassociated with the Be-star. G70.7+1.2 appears to be the result of the combined interaction of two distinct stars with dense molecular material: a luminous Be-star and an X-ray

emitting B-star pulsar binary. If correct, the resulting study of this object will be an interesting laboratory for the study of plasma processes. The observations and results are presented in §5.2. In §5.3 we discuss the implications of this source as it relates to resolving the mystery surrounding G70.7+1.2.

5.2 Observations and Analysis

5.2.1 X-ray

G70.7+1.2 was observed 2003 October 11.33 UT with the ACIS-S detector on *Chandra* in the standard, timed exposure mode. The archival data were analyzed with CIAO version 3.2[1]. We reprocessed the level 1 events from the *Chandra* X-ray Center (CXC) in order to make use of the latest calibration and removed pixel randomization. The level 2 event file was created by filtering grades 0,2,3,4,6 and good-time intervals. The total exposure time, after filtering periods higher than 3-σ above the mean background level, was 37.6 ksec.

Diffuse emission and a point source (hereafter CXO J200423.4+333907; Figure 5.1) are detected at the position of G70.7+1.2 (as first noted by Arzoumanian et al. 2004). We compared the positions of 27 X-ray sources on the S3 chip with counterparts in the 2MASS point source catalog to correct the native astrometry (Cutri et al. 2003b). This comparison showed evidence for a small systematic shift, $\Delta\alpha_{\rm 2MASS-CXO}$ = -0.13″ ± 0.11″, $\Delta\delta_{\rm 2MASS-CXO}$ = -0.08″ ± 0.11″. The best-fit position of CXO J200423.4+333907 including this offset, is α(J2000)=$20^{\rm h}04^{\rm m}23.430^{\rm s}$ and δ(J2000)=33°39′06.73 with measurement uncertainty of 0.03″ and 0.08″ in each coordinate, respectively. Combining the measurement and transformation errors in quadrature gives an uncertainty of 0.18″ (1-σ) for the X-ray position of the point source relative to 2MASS. This position lies 3.6″ from the nearby luminous Be-star, which implies the two are not associated (Kulkarni et al. 1992; Arzoumanian et al. 2004).

[1] http://www.cxc.harvard.edu/ciao/

We applied the adaptive smoothing algorithm CSMOOTH to highlight the diffuse emission after subtraction of CXO J200423.4+333907 and produced a flux-calibrated image by applying an exposure map as outlined in the CIAO threads. The contours of this emission are overlaid on a NIR image (see §5.2.2) of the nebula in Figure 5.1. Evidently, most of the diffuse X-ray emission is not coincident with the diffuse NIR emission.

We extracted photons within a 1.5″ circle (corresponding to 90% of the expected counts at 1.4 keV) around CXO J200423.4+333907 to perform spectral and variability analyses. The source contains only 33^{+7}_{-6} counts. Upon examination of regions both inside the diffuse emission and in a source-free area, we expect only two of these to be background photons. A Kolmogorov-Smirnov test shows that the arrival times of the source photons differed from a constant rate at only the ≈ 1-σ level, thus the source cannot be considered variable.

We begin our spectral analysis by noting that all the photons from CXO J200423.4+333907 fall in the range 1.0–4.5 keV, suggesting a hard spectrum. After calculating the response matrix and effective area of this portion of the CCD, we fit an absorbed power-law model to the spectrum using Cash statistics (due to the limited number of counts; Cash 1979). The best-fit parameters in Table 5.1 show a relatively hard photon index, $\Gamma \approx 1.8$, and low luminosity, $L_X \approx 4 \times 10^{31}\,\mathrm{erg\,s^{-1}}$ (2.0–10.0 keV) for an assumed distance of 4.5 kpc (Bally et al. 1989). These values are consistent with known accreting neutron stars in quiescence (e.g., Campana et al. 2002; Rutledge et al. 2007). In addition, we fit two absorbed power-law models with fixed parameters (see Table 5.1). The first has the photon index set to a typical value for quiescent neutron stars, $\Gamma = 2$. In this case the inferred column density is somewhat higher than that encountered by the diffuse emission (at the > 1 σ level; see below). The second model has the column density fixed to the best-fit value of the diffuse emission, $N_H = 1.0 \times 10^{22}\,\mathrm{cm^{-2}}$. Not surprisingly, this requires a harder photon index than the full fit of $\Gamma \approx 1.3$.

The probability of finding a source as bright or brighter than CXO J200423.4+333907 within the extent of G70.7+1.2 can be determined from the local source density. A

WAVDET analysis of the active CCDs (ACIS-I2,3 and ACIS-S1,2,3,4) finds that 12 sources are as bright or brighter than CXO J200423.4+333907. The inferred density is then ≈ 112 sources/deg^2. This density is consistent with observations taken as part of the ChaMPlane Survey (Grindlay et al. 2005), which predicts ≈ 100 sources/deg^2 with fluxes as bright or brighter than CXO J200423.4+333907 (Hong et al. 2005). Consequently, there is a 0.3% probability that such a source would be found within G70.7+1.2 by chance.

The diffuse emission presented enough counts for basic spectroscopy with χ^2 statistics. We extracted events from a region of dimension $\approx 30'' \times 30''$ surrounding the diffuse emission (excluding the point source) and a source-free background region immediately east of the nebula with the same shape. This yielded 690 ± 26 source counts, of which ≈ 320 are expected to be due to the background. The resulting source plus background photons were grouped such that each bin contained at least 25 counts.

The background subtracted spectrum was analyzed using XSPECv11[2]. We fit two models modified by absorption to the spectrum: a power-law and a Raymond-Smith plasma (see Table 5.1). The unphysically steep photon index of the power-law model and the lower χ^2_ν value lead us to adopt the Raymond-Smith model for the remainder of our analysis. Thus, we interpret the diffuse emission as a thermal plasma with $k_B T \approx 0.7\,\mathrm{keV}$ and $N_H \approx 1 \times 10^{22}\,\mathrm{cm}^{-2}$. The derived value of N_H is reasonably consistent with that of CXO J200423.4+333907 and the estimated value of $1.25 \times 10^{22}\,\mathrm{cm}^{-2}$ from Dickey & Lockman (1990). Integrating this model over the 0.5–2.5 keV bandpass implies a luminosity of 8.1×10^{32} erg s^{-1} at the distance of G70.7+1.2, although it is not clear that this emission is associated with the nebula (see §5.3).

[2]See http://heasarc.nasa.gov/docs/xanadu/xspec/

5.2.2 Near-Infrared LGS-AO

G70.7+1.2 was observed under photometric conditions on 2005 April 30 UT with Laser Guide Star Adaptive Optics (LGS-AO; Wizinowich et al. 2006b; van Dam et al. 2006) on the Keck II telescope and the Near-Infrared Camera 2 (NIRC2). We imaged the field in the J, H and K'-bands with the wide camera of NIRC2, which provides a $\approx 40'' \times 40''$ field of view and a $\approx 0.04''$ pixel scale. The H and K'-band data sets consisted of five frames in each band. Each frame was exposed for 5 sec with 10 additions performed on the chip at five dither positions separated by $\approx 30''$. The J-band data consisted of two images at the center of the chip.

Each frame was flat-fielded, background subtracted, and repaired for bad pixels using custom PyRAF software[3]. We then performed a second round of sky subtraction using a median combination of similarly processed frames of a nearby field. We used these processed images of G70.7+1.2 for photometric analysis, but produced a separate set of images for astrometry due to optical distortion in the NIRC2 camera. The distortion in the second set was corrected using algorithms derived from the preshipment review documents[4] with the IDL procedure provided by the Keck Observatory[5]. The correction does not conserve flux, and thus is not suitable for photometry.

We registered a median combination of the distortion corrected H-band frames to the 2MASS point source catalog using 8 stars that were not over-exposed. We find residuals of $0.04''$ and $0.09''$ in right ascension and declination, respectively. Registering the J and K'-band frames to this image yielded negligible residuals. Combining these errors with those in the X-ray position of CXO J200423.4+333907 yields an uncertainty of $0.19''$ (1-σ) of the X-ray image with respect to the NIR images. Figure 5.1 shows the registered H-band frame with the *Chandra* error circle (99% confidence). We clearly identify a single NIR counterpart in all filters within the X-ray error circle. The best-fit position of this source is α(J2000)=$20^{\rm h}04^{\rm m}23.446^{\rm s}$ and

[3]PyRAF is a product of Space Telescope Science Institute, which is operated by AURA for NASA.
[4]available at http://www2.keck.hawaii.edu/inst/nirc2/
[5]See http://www2.keck.hawaii.edu/optics/lgsao/software/

δ(J2000)=33°39′06.62 with an uncertainty of 0.04″ and 0.09″ (relative to 2MASS), respectively. The centroiding errors are negligible. This position lies 0.23″ from the *Chandra* position.

We performed aperture photometry of the source in each band on each individual frame relative to the 2MASS stars in the field with the IRAF package APPHOT. We assume that the color term used to transform from the 2MASS K_s filter to the K' is negligible for our purposes. The uncertainties were determined with the 2MASS photometric uncertainty, the standard deviation of the zero-point determinations from the same 2MASS star in multiple frames, and the photometric error of the NIR source itself added in quadrature. We find magnitudes of $J = 15.56 \pm 0.09$, $H = 14.51 \pm 0.11$, and $K' = 13.97 \pm 0.06$.

The probability of finding a star with $K' \approx 14$ magnitude in our *Chandra* error circle by chance is very low. To quantify this, we extracted all sources present in the 2MASS catalog within 20′ of G70.7+1.2. We find that the differential number of sources per magnitude per square arcsecond is well described by a single power-law with index 0.35 over the magnitude range $3 < K_{\rm s} < 15$. We can conservatively assume (based on Galactic star count models by Nakajima et al. 2000) that this can be extrapolated to our 5-σ detection limit of $m_{K'} \approx 20.0$ magnitude. From this we calculate that there is a $\approx 25\%$ percent chance of finding a source brighter than our detection limit in a circular region with a 0.49″ (99% confidence) radius. However, the probability of finding a source with $K_s = 14.0$ magnitude or brighter is $\lesssim 0.1\%$. Thus it is unlikely that our NIR counterpart is drawn from the background population, and we assume that it associated with CXO J200423.4+333907.

The key issue in determining the nature of this source is the assumed extinction. Based on the colors of the luminous Be-star, Becker & Fesen (1988) estimate $A_V \approx 5.6$. This agrees well with the value of $A_V \approx 5.4$ obtained by taking N_H as determined from the spectrum of the diffuse X-ray emission and translating it into extinction (Predehl & Schmitt 1995). If we plot the NIR counterpart on a color-magnitude diagram (Figure 5.2) using this reddening, we find that the star is consistent with a late G/early K giant spectral type at a distance of ≈ 11 kpc. Consequently, the star

is underluminous if of this spectral type and associated with G70.7+1.2 at a distance of 4.5 kpc (Figure 5.2).

The spectral fitting of the point source spectrum itself, albeit with poor statistics, implies a higher extinction of $A_V = 8.4^{+6.4}_{-5.5}$. This allows for the possibility that the NIR counterpart is a heavily obscured main sequence B-star with $A_V \approx 10.0$ at the distance of G70.7+1.2. We prefer this interpretation when we consider the probabilistic arguments and existing multifrequency observations of G70.7+1.2 (see §5.3).

5.3 Discussion and Conclusions

We identify a low-luminosity, hard X-ray point source with a NIR counterpart at the center of G70.7+1.2 using high resolution imaging. Both the measured X-ray luminosity, $L_X \approx 4 \times 10^{31}$ erg s^{-1}, and the photon index, $\Gamma \approx 1.8$, of CXO J200423.4+333907, are consistent with quiescent high-mass X-ray binaries containing a neutron star (e.g., Campana et al. 2002; Rutledge et al. 2007). The magnitude and J-K' color in combination with the X-ray column density suggests the NIR counterpart is either an evolved background star or a heavily extincted B-star. However, an isolated background late-G/early-K giant cannot explain the observed X-ray flux. These stars have deep convective zones that power coronal X-ray emission, but it is typically $\lesssim 10^{31}$ erg s^{-1} (Güdel 2004). This is an order of magnitude below the required $L_X \approx 2.5 \times 10^{32}$ erg s^{-1} calculated by assuming the observed X-ray flux at a distance of 11 kpc. In addition, spectral types later than B2 have have observed X-ray luminosities $\lesssim 10^{31}$ erg s^{-1} (Berghoefer et al. 1997). This suggests that the NIR source and CXO J200423.4+333907 constitute an X-ray binary, and probabilistic arguments suggest that this binary is associated with G70.7+1.2.

A simple geometric model can explain the existing multifrequency data (Figure 5.3). The velocity of the molecular gas as measured by CO observations is 5km s^{-1} with respect to the local standard of rest (Bally et al. 1989). The stellar Hα line profile from the bright Be-star is redshifted with respect to the CO with a velocity of

20–60km s^{-1}, while Hα reflected by dust in the eastern region is also redshifted with respect to the CO, but is blueward of the stellar Hα by 10–50km s^{-1}. This implies that the bright Be-star is moving into the cloud, away from the Earth. However, the [O I] and Hα throughout the rest of nebula traces the non-thermal radio emission and is uniformly blue-shifted by 10–120km s^{-1} with respect to CO, suggesting that the source responsible for the shock is moving into the cloud, toward the Earth.

The cloud size, as inferred from CO, is $3D_{4.5}$ pc on the sky, where $D_{4.5}$ is the distance to G70.7+1.2 in units of 4.5 kpc. If the cloud is roughly spherical and has $n_H \sim 10^3\,\mathrm{cm}^{-3}$, then objects will have an additional ≈ 5 magnitudes of extinction with respect to objects on the near side. Thus, a natural explanation for the geometry of G70.7+1.2 is that the bright Be-star is moving into the near side of the cloud creating a reflection nebula, while on the far side, a heavily extincted B-star/pulsar binary is moving into the cloud creating a bow shock and powering the nebula (Figure 5.3).

One remaining puzzle is the origin and impact of the hot gas powering the diffuse X-ray emission. Figure 5.1 shows that the radio/optical and diffuse X-ray morphologies are substantially different, and the peak of the diffuse X-ray emission is separated $\approx 20''$ from the center of the radio/optical emission (which contains the Be-star and X-ray binary). Thus, it is apparent that this hot gas does not play an important dynamic nor, given its luminosity is $\sim 10^{32}$ erg s^{-1}, energetic role in shaping G70.7+1.2. Two viable explanations for the origin of the hot gas are, given the quasi-shell like morphology, that it is the result of a previous explosive event that the X-ray binary is overtaking or it may be unassociated with the G70.7+1.2. In any case, the origin of this plasma — either related or unrelated to G70.7+1.2 — is unknown.

The definitive proof of the proposed model (Figure 5.3) would be the discovery of a pulsar associated with G70.7+1.2. A search for pulsations with the Green Bank Telescope at 2.2 GHz is underway. If a pulsar is found, G70.7+1.2 will be an important laboratory for studying plasma processes taking place between the pulsar/B-star wind and the interaction of that mixture with the cold molecular gas.

Table 5.1. X-ray Spectral Fits

Model	N_H (10^{22} cm^{-2})	Γ/k_BT (keV)	Flux (10^{-14} erg cm^{-2} s^{-1})	χ^2/ν
(1)	(2)	(3)	(4)	(5)
Diffuse Emission				
Power-law	$0.70^{+0.19}_{-0.13}$	$4.4^{+0.9}_{-0.5}$	31^{+22}_{-11}	18.2/13
Raymond-Smith Plasma	$1.04^{+0.08}_{-0.07}$	$0.71^{+0.05}_{-0.07}$	33^{+9}_{-5}	9.75/13
CXO J200423.4+333907				
Power-law	$1.5^{+1.1}_{-1.0}$	$1.8^{+1.2}_{-1.1}$	$1.7^{+5.6}_{-1.7}$	—
Power-law ($\Gamma = 2.0$)	$1.6^{+0.5}_{-0.4}$	(2.0)	$1.6^{+0.5}_{-0.4}$	—
Power-law ($N_H = 1 \times 10^{22}$)	(1.0)	$1.3^{+0.5}_{-0.4}$	$2.0^{+1.0}_{-0.7}$	—

Note. — All errors are 68% confidence levels. Values in parentheses are held fixed. (1) – Absorbed spectral model. (2) – Best-fit column density. (3) – Measured photon index for power-law models and k_BT for the Raymond-Smith plasma. (4) – The unabsorbed flux in the 0.5–2.5 keV band for the diffuse emission and 2–10 keV band for CXO J200423.4+333907. (5) – The value of χ^2 for diffuse emission models and the number of degrees of freedom, ν. This column is not applicable to CXO J200423.4+333907 since the spectral fitting was performed with Cash statistics.

Acknowledgements

We thank A. Kraus for useful discussions and the anonymous referee for helpful comments. This work is supported in part by grants from the National Science Foundation and NASA. The W. M. Keck Observatory is operated as a scientific partnership among the California Institute of Technology, the University of California, and the National Aeronautics and Space Administration. The Observatory was made possible by the generous financial support of the W. M. Keck Foundation.

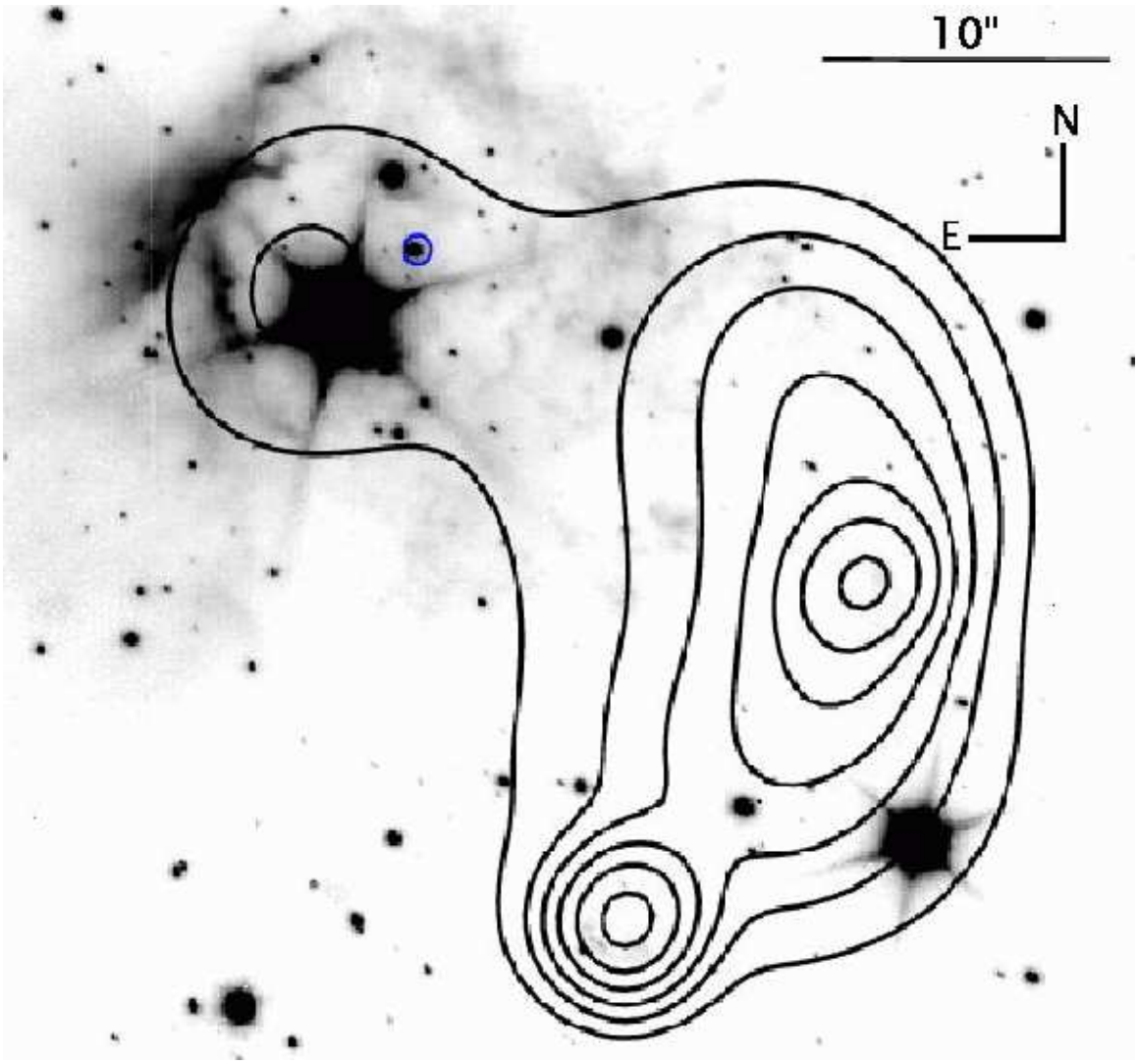

Figure 5.1 H-band image of G70.7+1.2 with contours of the adaptively smoothed X-ray emission (black lines) and the *Chandra* 99% confidence (0.49″) error circle for CXO J200423.4+333907 (blue circle). The X-ray contours are logarithmically spaced between 10% and 90% of the peak emission.

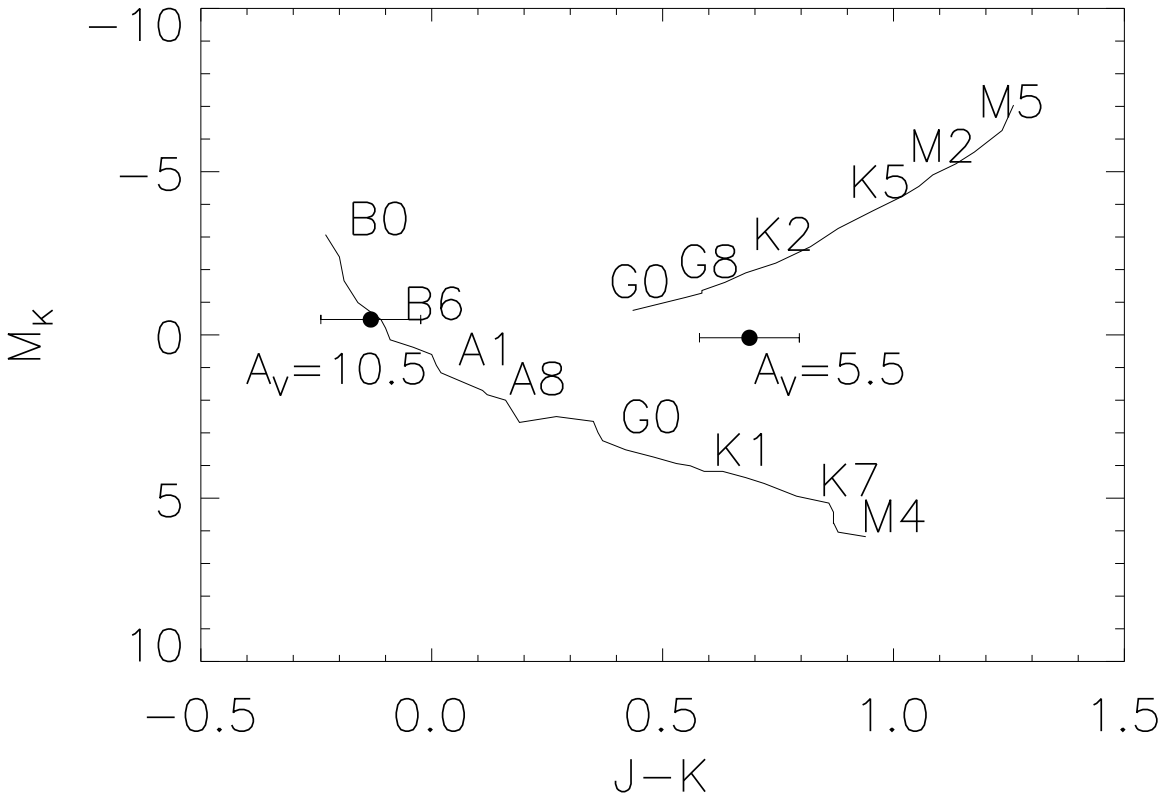

Figure 5.2 Color magnitude diagram using data from Bessell & Brett (1988). Filled circles show the IR counterpart for $A_V = 5.5$ and $A_V = 10.5$ at a distance of 4.5 kpc. The error bars are 1 σ.

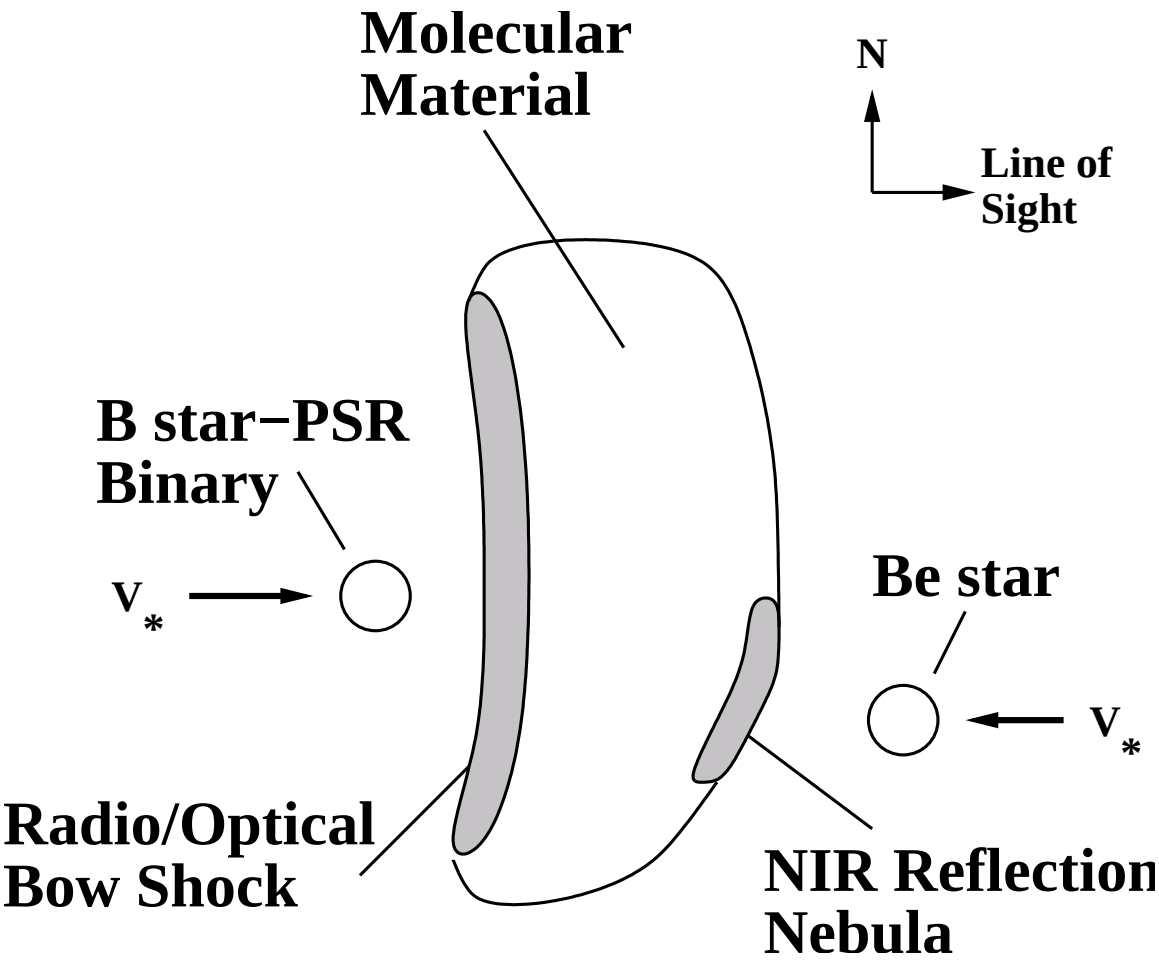

Figure 5.3 Diagram of the geometry of G70.7+1.2. The newly discovered X-ray binary moves into the far side of the molecular material powering the radio/NIR/optical nebula, whereas the Be-star creates a reflection nebula on the near-side. See the text for details.

Chapter 6

Summary and Future Directions

In this thesis we have applied a variety of techniques to tackle open questions regarding neutron stars. In particular, we have developed and demonstrated that unprecedented precision and accuracy, $\lesssim 100\,\mu$as, is achievable with single aperture telescopes through the use of our optimal estimation technique and careful experimental design. We have used this technique on some of the faintest detectable near-infrared targets to substantively and directly address outstanding issues regarding their origins and evolution. These facts show that astrometry with adaptive optics has incredible potential for future scientific returns on the world's largest apertures.

If future AO systems are to be utilized to the full astrometric potential predicted here, a number of issues will need to be further addressed. The first is the issue of a better understanding of the AO PSF. Our technique successfully eliminates the astrometric noise inherent in AO observations, leaving the determination of the stellar centers as the dominant random error. A better analytic formulation and the development of computational tools are necessary to reduce centering determination (particularly for LGS-AO) to the levels predicted by photon noise.

The techniques developed here could also be improved. In Chapter 1 we utilized the spatial correlation due to atmospheric tilt jitter to help eliminate noise caused by the atmosphere. One aspect we have not considered, which is also useful from an AO control system perspective, are the temporal correlations that exist. An approach using Kalman filtering, for example, could yield astrometric benefits.

Design considerations for future AO systems must consider the astrometric sys-

tematic implications of their choices, since they will provide the practical limits achievable. In particular, the distortion in the optical path will need to be calibrated and tracked consistently. For larger apertures, the effects of differential chromatic refraction will become larger and larger as fraction of the diffraction limit. Thus, any devices that correct atmospheric refraction at high accuracy will need to be thoroughly characterized.

One of the most exciting areas for astrometry in the near future is GAIA, which will provide an incredibly precise and accurate astrometric catalog of the entire sky. The absolute state of motion of at least one star in the field (and of tip-tilt stars in MCAO systems), provides an important constraint for the least-squares astrometric formalism utilized in Chapter 2, and will revolutionize the field of astrometry.

On the scientific front, a number of new avenues are now available for study given the astrometric performance demonstrated here, specifically for compact objects. Our understanding of Galactic compact objects has suffered from the lack of astrometric measurements. Determinations of their proper motions, distances, and binary inclinations have been largely inaccessible to current ground and spaced-based instrumentation. Their large distances and location in the Galactic Plane results in small astrometric signals, faint targets, and confusion. With the accuracy demonstrated here it would be possible to obtain parallax measurements to accreting systems and even some dynamical masses. Thus, accurate astrometric knowledge of fundamental quantities is in reach with modest aperture AO-equipped telescopes, and can answer fundamental questions in astrophysics: *How does the diversity of cosmic explosions result in the diversity of compact objects? What is the equation of state of neutron stars? How massive are Galactic black holes?*

Appendix A

NIRC2 Geometric Distortion

A.1 Summary

Here we compute a new solution for the geometric distortion in the wide (40 mas/pixel) and narrow (10 mas/pixel) cameras of NIRC2. We find the post-fit residuals are improved by a factor of 6–8 over the previous (preship) solution with magnitudes $\lesssim 0.1$ pixels (1-σ). There is still some small scale structure in the residuals indicating that a higher order solution may be necessary. We also include a comparison with the previous solution.

A.2 Introduction

All optical systems suffer from some type of geometric distortion. Here we will characterize this distortion for the NIRC2 camera behind the AO system at the Keck II telescope.

A solution for all three NIRC2 cameras was derived from images of a grid of holes drilled in fused silica to simulate a known reference grid (which we will refer to also as the pin hole mask; Figure A.1). The current distortion solutions for each camera have a polynomial expression in the form

$$x' = a_0 + a_1 x + a_2 y + a_3 x^2 + a_4 xy + a_5 y^2 + a_6 x^3 + a_7 x^2 y + a_8 x y^2 + a_9 y^3, \quad \text{(A.1)}$$

$$y' = b_0 + b_1 x + b_2 y + b_3 x^2 + b_4 xy + b_5 y^2 + b_6 x^3 + b_7 x^2 y + b_8 xy^2 + b_9 y^3, \quad \text{(A.2)}$$

where

$$x = x_{\rm obs} - 512, \quad \text{(A.3)}$$

$$y = y_{\rm obs} - 512. \quad \text{(A.4)}$$

Here $x_{\rm obs}$ and $y_{\rm obs}$ are the observed locations of the pin holes, whereas x' and y' are their positions after correcting for the geometric distortion (i.e., their 'true' positions in a distortion free system).

One minor point — there is an inconsistency with this solution. First, the center of the array ($x_{\rm obs} = 512, y_{\rm obs} = 512$) is, by definition, free of distortion. However, fitting for the constants a_0, b_0 shifts a star at 512,512 from the center of the array. In reality, these coefficients just represent an overall shift of the pin hole image, so they should be dropped when applying the solution.

The preship solution can be found in Table A.1 (Thompson et al.) and is shown graphically for the wide camera in Figures A.4 & A.5 and in Figures A.10 & A.11 for the narrow camera. The post-fit residuals, after applying this preship solution, were reported as $(\sigma_x, \sigma_y) = (0.57, 0.29)$ for the wide camera and $(\sigma_x, \sigma_y) = (0.81, 0.62)$ for the narrow camera (Thompson et al. 2001[1]). Our goal is to improve these values.

A.3 Data

We will consider two data sets for determining the wide (40 mas/pixel) and narrow (10 mas/pix) camera solutions (the medium resolution camera is used rarely for imaging). The wide camera data set consists of 5 images of the illuminated pin hole mask taken with 5 second integrations and 4 on chip coadds. The data were taken on 2006 Dec 20 UT. The narrow camera consists of 10 images with 20 second exposure times and 3 coadds taken on 2006 Nov 29 UT. The data have images taken at two different dither positions separated by $\sim 1/2$ a hole spacing. Both data sets are after the large earthquake to hit Hawaii in 2006 Oct. A diagram of the pin hole mask is seen in

[1] available at http://www2.keck.hawaii.edu/inst/nirc2/preship_testing.pdf

Figure A.1, and has an expected hole separation of 24.25 pixels in the wide camera and 48.41 pixels in the narrow. An image of the coarse grid with the wide camera can be seen in Figure A.2. The sliding mechanism that holds the slit masks can't quite move the coarse grid over the entire chip; thus, we can only characterize the region of $x \sim [0 : 800]$. The difference image of the fine grid at two positions with the narrow camera can be seen in Figure A.3.

A.4 Analysis

The data reduction is straight forward. First we linearize the frames according the the prescription of Stan Metchev[2], then flat field with dome flats. The leakage of light from the lamps in the AO bench (used to illuminate the mask) is significant and leads to a gradient across the chip. Moving the pin hole mask by $\sim 1/2$ the hole spacing is effective for narrow camera, but doesn't yield good background subtraction for the wide camera.

The next step is to derive the observed positions for the pin holes. We do this by fitting a simple Gaussian model to the pin hole images (which yields results that are consistent with fitting each source with a modeled, spatially varying PSF). We will refer to these as $x_{\rm obs}$ and $y_{\rm obs}$.

The above steps are straightforward, but deriving the *expected* pin hole positions for comparison is more difficult. It is clear from Figure A.2 that the grid has some rotation with respect to the $x - y$ axes of the NIRC2 detector. Also, the prediction of the hole spacing on the detector rests on the assumption of detector pixel scale, which could be variable (though this is unlikely). Therefore, we determine the 'true' orientation of the pin hole mask by creating a grid of positions, then compute the shift, scale, and rotation which minimizes the residuals with the data in a least-squares sense. The best-fit scale differs from the nominal value of 39.686 mas/pix by only 5×10^{-4} and the best-fit rotation is 0.277° clockwise. For the narrow camera the best-fit scale differs from the nominal value of 9.942 mas/pix by only 9.35×10^{-4}

[2]http://www.astro.ucla.edu/∼metchev/ao.html

and it rotated 0.082° clockwise.

The residuals between the expected pin hole positions and the observed positions are shown in Figures A.6 & A.7 for the wide camera and in Figures A.12 and A.13 for the narrow camera. We see that the gross features are similar to the preship solutions, but there are some noticeable differences. We will quantify this below in § A.5.

We fit a new polynomial solution using the same form as above for the measured and expected positions using the IDL package MPFIT by C. Markwardt [3]. For the wide camera we require a 3rd order solution whereas for the narrow camera a 4th order solution (and possibly higher) is justified. The solution can be found in Table A.2. The 4th order polynomial is

$$\begin{aligned} x' &= a_0 + a_1 x + a_2 y + a_3 x^2 + a_4 xy + a_5 y^2 \\ &\quad + a_6 x^3 + a_7 x^2 y + a_8 x y^2 + a_9 y^3 \\ &\quad + a_{10} x^4 + a_{11} x^3 y + a_{12} x^2 y^2 + a_{13} x y^3 + a_{14} y^4, \end{aligned}$$

$$\begin{aligned} y' &= b_0 + b_1 x + b_2 y + b_3 x^2 + b_4 xy + b_5 y^2 \\ &\quad + b_6 x^3 + b_7 x^2 y + b_8 x y^2 + b_9 y^3 \\ &\quad + b_{10} x^4 + b_{11} x^3 y + b_{12} x^2 y^2 + b_{13} x y^3 + b_{14} y^4. \end{aligned}$$

The post-fit residuals are significantly improved. In the wide camera the RMS values in each axis are $(\sigma_x, \sigma_y) = (0.0922, 0.0870)$, $\lesssim 4$ mas. The residuals are shown graphically in Figure A.8 and are broken down by coordinate in Figure A.9. In the narrow camera we find post-fit residuals $(\sigma_x, \sigma_y) = (0.0599, 0.0639)$, $\sim 600\,\mu$as. The residuals are shown graphically in Figure A.14 and are broken down by coordinate in Figure A.15. Noticeable higher order structure remains in the narrow camera residuals, thus a higher order polynomial may further reduce the residuals.

[3] http://cow.physics.wisc.edu/ craigm/idl/idl.html

A.5 Comparison with Preship Solution

To compare the preship solutions with our newly derived solutions, we look at the predictions of both at a series of grid points over the chip. The residuals for the wide camera between the two solutions are shown in Figures A.16 & A.17 and in Figures A.18 & A.19 for the narrow camera. The most important difference is the appearance of an overall rotation between the new and preship solutions for both the wide and narrow cameras. This likely stems from a small mistake in the preship analysis. Namely, the *observed* pin hole positions were corrected for an overall rotation with respect to the NIRC2 axes (how this angle is measured is ambiguous) instead of the *expected* positions. This will yield a measurement of distortion that is about the right magnitude, but it will be associated with a slightly wrong portion of the chip.

We can remove this effect by computing a simple linear transformation between the two solutions (fitting for just shift, scale and rotation). The residuals after this computation (which is generally just an overall rotation) are shown in Figures A.22 & A.23 for the narrow camera and Figures A.20 & A.21 for the wide camera. The top and lower right-hand corners seem to show the most significant discrepancies when compared to the preship values, ~ 1 pixel.

Table A.1. Preship Distortion Solutions for NIRC2.

Coefficient	Narrow	Wide
a_0	(-2.72 ± 0.94)E-01	(4.06 ± 0.46)E-01
a_1	(1.0009 ± 0.0005)E$+00$	(1.0008 ± 0.0002)E$+00$
a_2	(5.08 ± 0.52)E-03	(-3.24 ± 0.23)E-03
a_3	(-5.52 ± 0.52)E-06	(-1.75 ± 0.33)E-06
a_4	(7.7 ± 6.4)E-07	(-5.6 ± 3.0)E-07
a_5	(5.37 ± 0.80)E-06	(10.00 ± 0.33)E-06
a_6	(-8.6 ± 2.6)E-09	(-6.8 ± 1.3)E-09
a_7	(-8 ± 25)E-10	(8 ± 12)E-10
a_8	(-6.1 ± 2.7)E-09	(-3.6 ± 1.2)E-09
a_9	(-4.4 ± 3.4)E-09	(9 ± 13)E-10
b_0	(1.68 ± 0.94)E-01	(3.4 ± 4.6)E-02
b_1	(1.6 ± 4.7)E-04	(2.1 ± 2.3)E-04
b_2	(1.0008 ± 0.0005)E$+00$	(9.9477 ± 0.0023)E-01
b_3	(2.1 ± 6.5)E-07	(-4.4 ± 3.3)E-07
b_4	(-9.93 ± 0.64)E-06	(-9.2 ± 3.0)E-07
b_5	(1.78 ± 0.80)E-06	(-1.57 ± 0.33)E-06
b_6	(-1.6 ± 2.6)E-09	(2 ± 13)E-10
b_7	(-2.8 ± 2.5)E-09	(2.6 ± 1.2)E-09
b_8	(-4 ± 27)E-10	(5 ± 12)E-10
b_9	(-1.2 ± 0.35)E-08	(5.9 ± 1.3)E-09

Table A.2. New Distortion Solutions for NIRC2.

Coefficient	Narrow	Wide
a_0	1.30660E−02	−6.32775E−01
a_1	1.00116E+00	1.00258E+00
a_2	1.96010E−03	−1.07553E−03
a_3	−3.14182E−06	−8.44603E−07
a_4	−3.08788E−06	−8.66153E−07
a_5	5.59549E−06	1.03161E−05
a_6	−6.04724E−09	−2.80832E−09
a_7	6.53706E−10	2.11712E−12
a_8	−3.99943E−09	−8.90944E−10
a_9	−1.63796E−09	−3.14757E−11
a_{10}	−1.12204E−11	—
a_{11}	1.35291E−11	—
a_{12}	5.73354E−12	—
a_{13}	3.37186E−12	—
a_{14}	−8.50332E−13	—
b_0	2.06853E−01	2.17931E−02
b_1	1.75403E−03	−1.39196E−03
b_2	1.00129E+00	9.96806E−01
b_3	−1.91215E−06	−2.81300E−07
b_4	−1.16438E−05	−5.77556E−07
b_5	−2.51404E−06	−1.44116E−06
b_6	6.03978E−11	5.30766E−10
b_7	−3.24360E−09	4.39543E−09

Table A.2—Continued

Coefficient	Narrow	Wide
b_8	−3.55861E−09	−3.07567E−10
b_9	−8.66718E−09	7.84907E−09
b_{10}	5.17175E−12	—
b_{11}	2.66960E−12	—
b_{12}	5.29880E−12	—
b_{13}	7.83758E−12	—
b_{14}	4.80703E−12	—

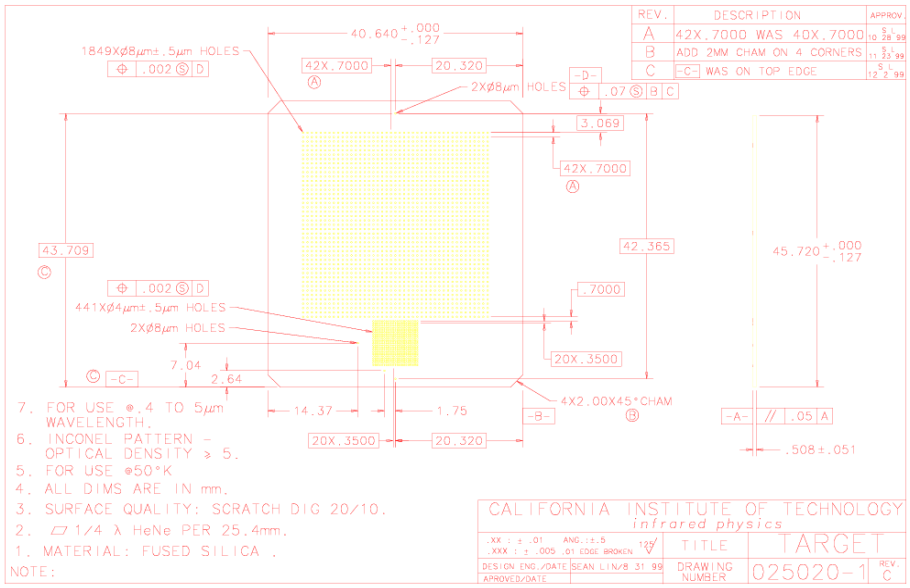

Figure A.1 Schematic of the layout of the pin hole mask. All distances are in millimeters unless denoted otherwise (Courtesy K. Matthews).

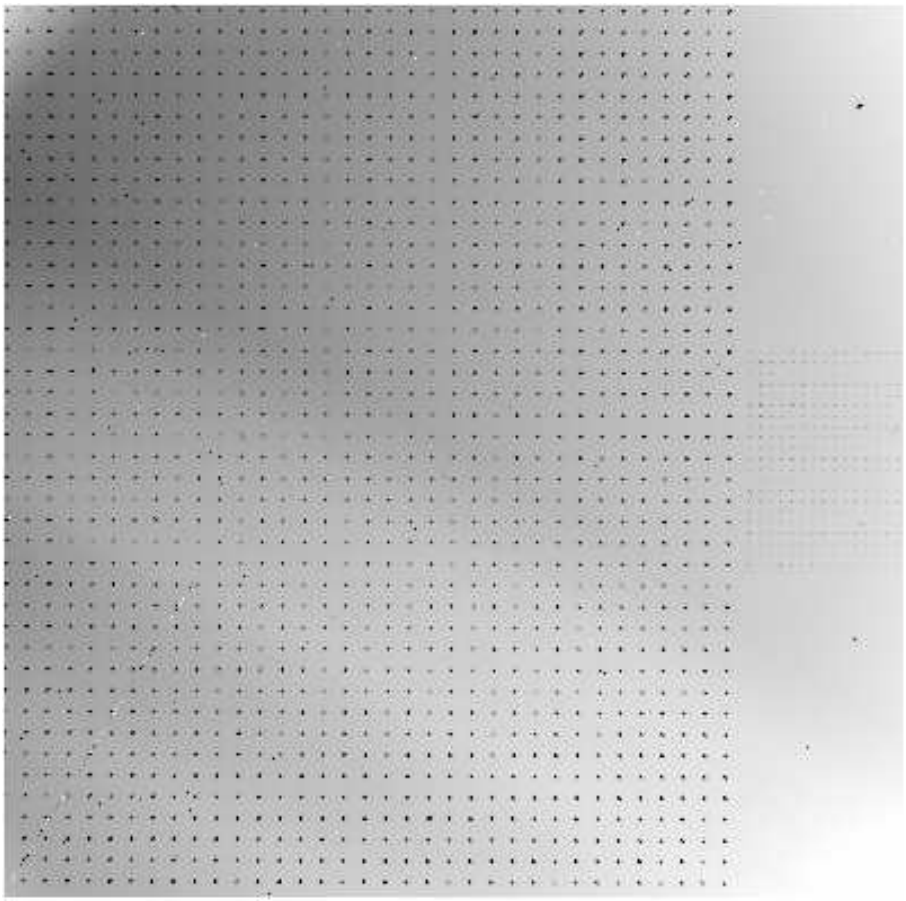

Figure A.2 Image of the coarse pin hole mask with the wide camera. The gradient from poor flat fielding (due to light leakage) and the gap on the right section of the chip is evident (as is the fine mask).

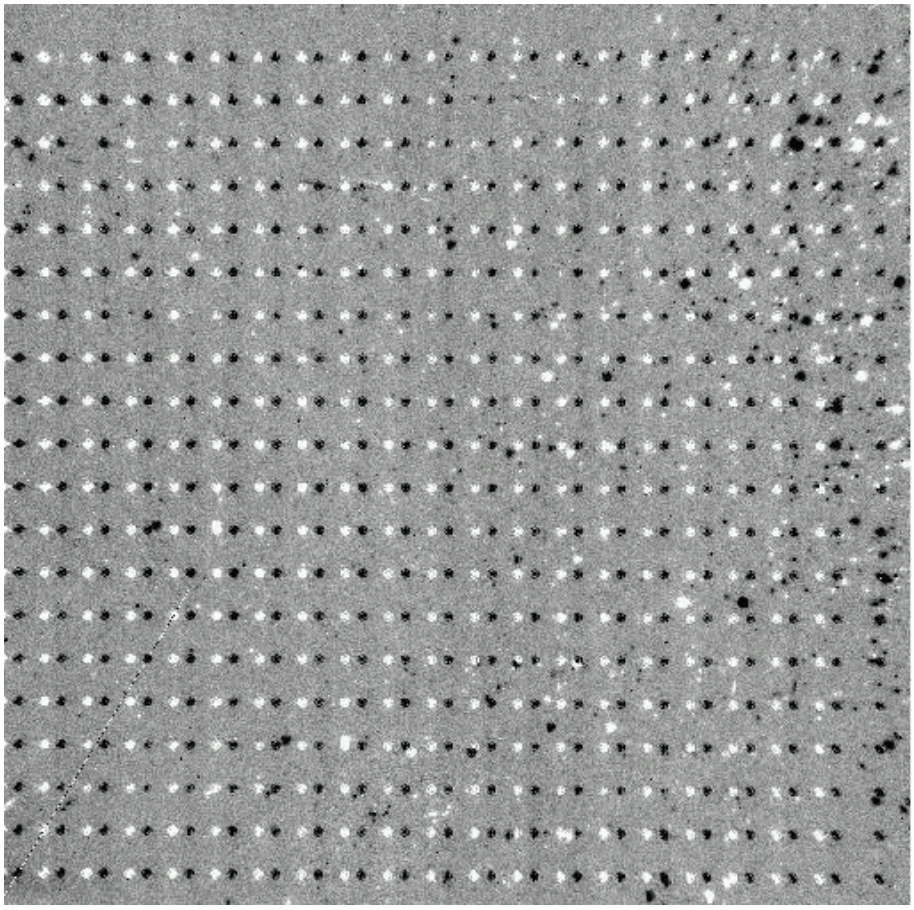

Figure A.3 Difference image of two positions of the fine pin hole mask with the narrow camera. The artifacts on the right portions of the chip are likely due to defects in the mask substrate, but do not seem to significantly effect the determination of the pin hole source centers.

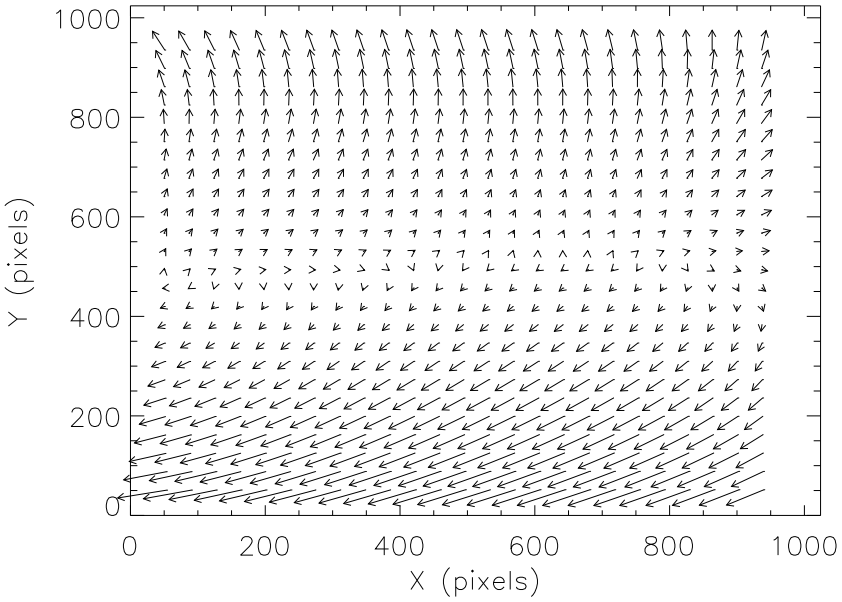

Figure A.4 Distortion measured in the wide camera as reported by Thompson et al. See Figure A.5 for the magnitude of the arrows.

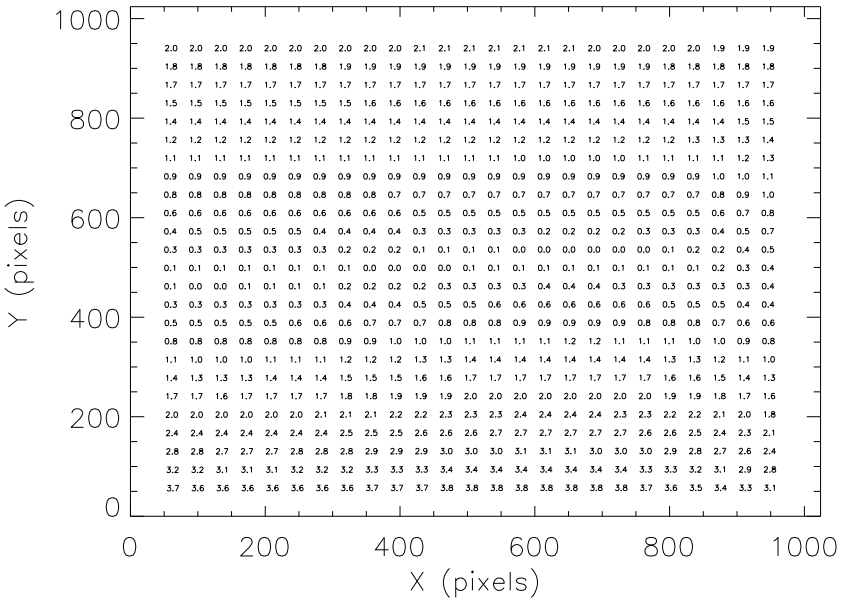

Figure A.5 Amplitude in pixels of the preship distortion in the wide camera.

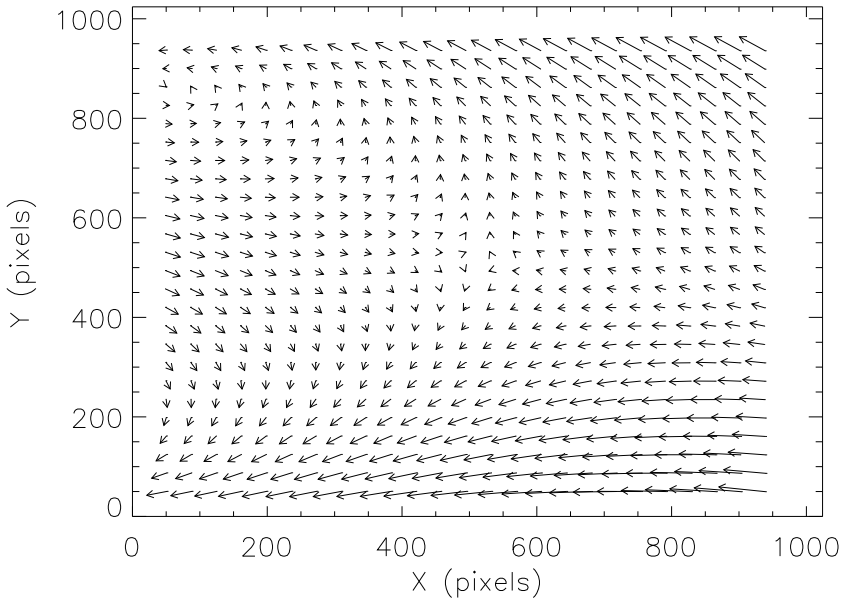

Figure A.6 Distortion measured in the wide camera as measured in this work. See Figure A.7 for the magnitude of the arrows.

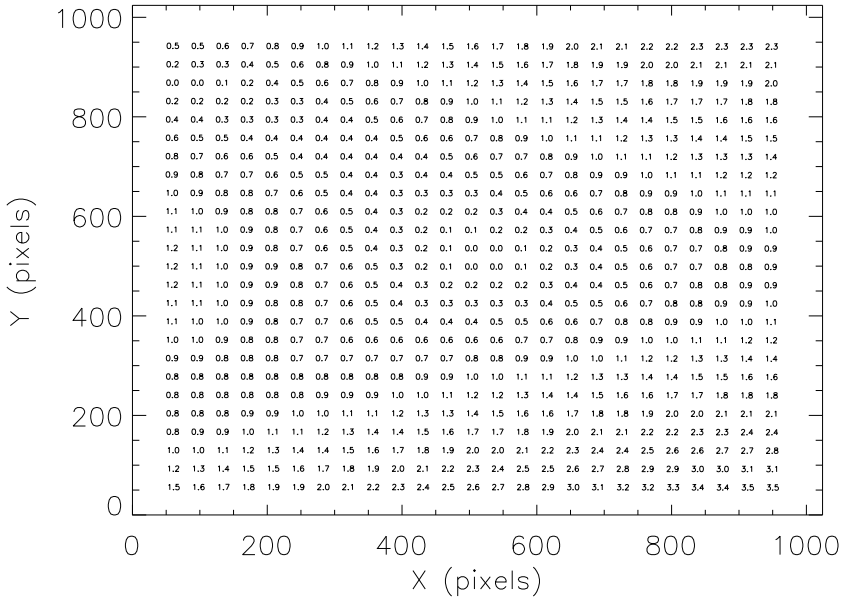

Figure A.7 Amplitude in pixels of the distortion in the wide camera from the current data.

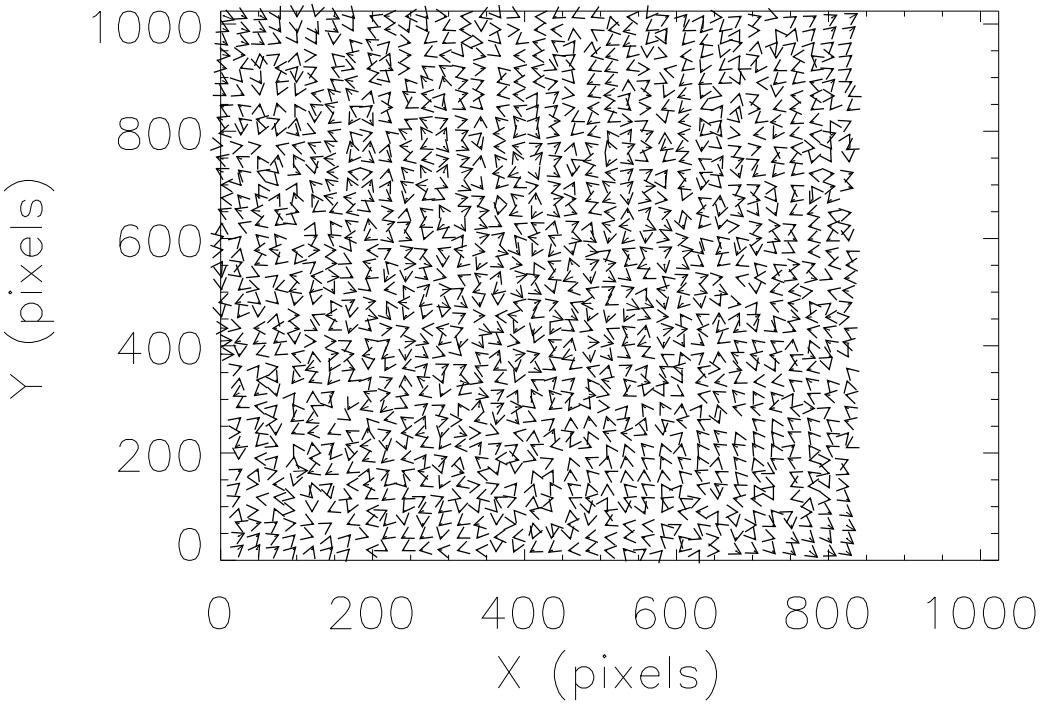

Figure A.8 Measured residuals after application of the new wide camera distortion solution. Residuals are multiplied by a factor of 100. The residuals are < 0.1 pixels and do not show obvious systematic trends. See Figure A.9 for further information.

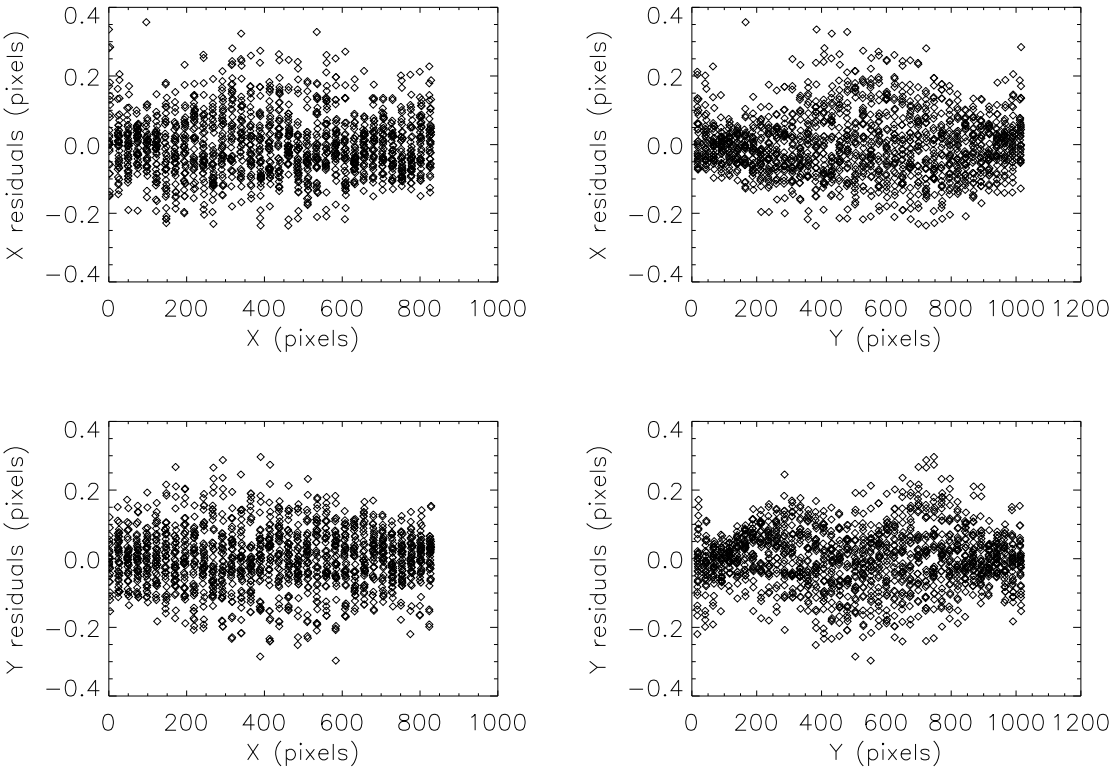

Figure A.9 Wide camera residuals as a function of chip position. The RMS of the remaining residuals is $(\sigma_x, \sigma_y) = (0.0922, 0.0870)$ pixels. Includes all rows and columns.

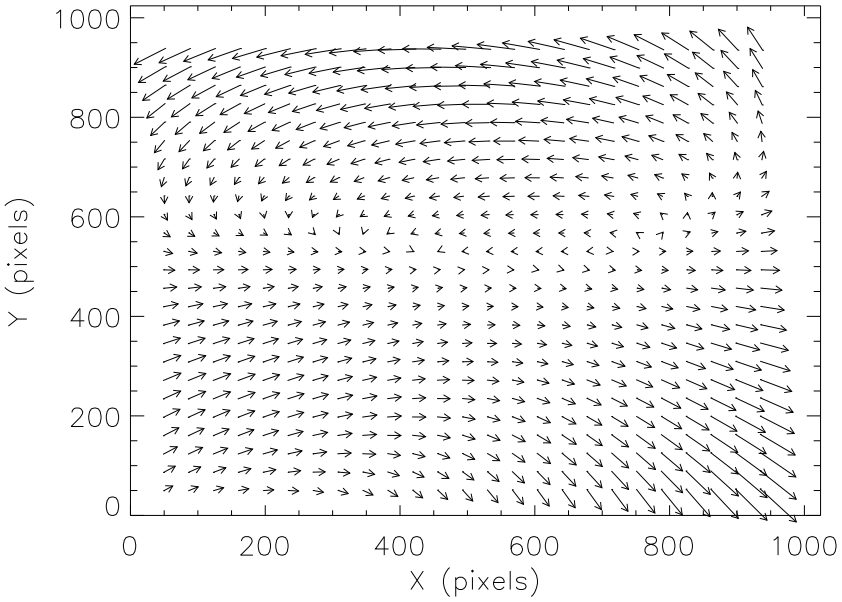

Figure A.10 Distortion measured in the narrow camera as reported by Thompson et al. See Figure A.11 for the magnitude of the arrows.

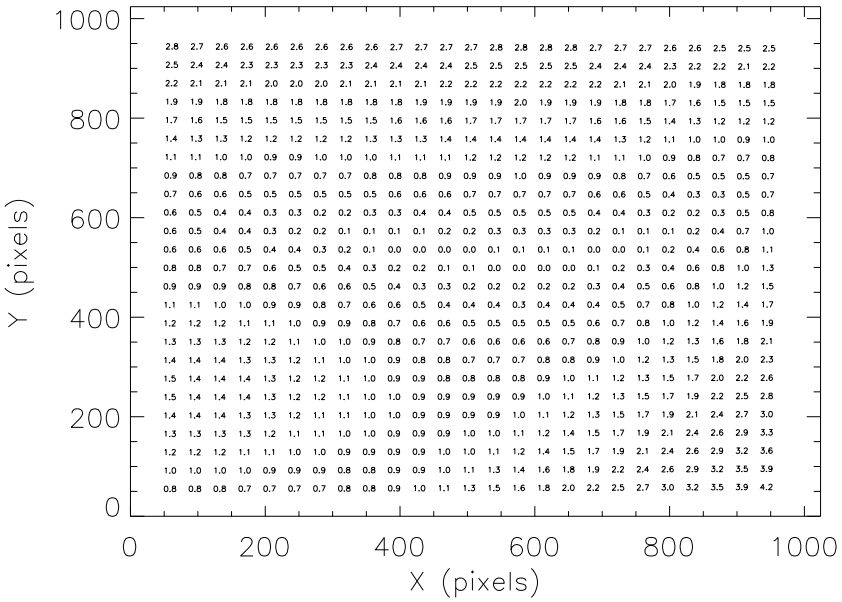

Figure A.11 Amplitude in pixels of the preship distortion in the narrow camera.

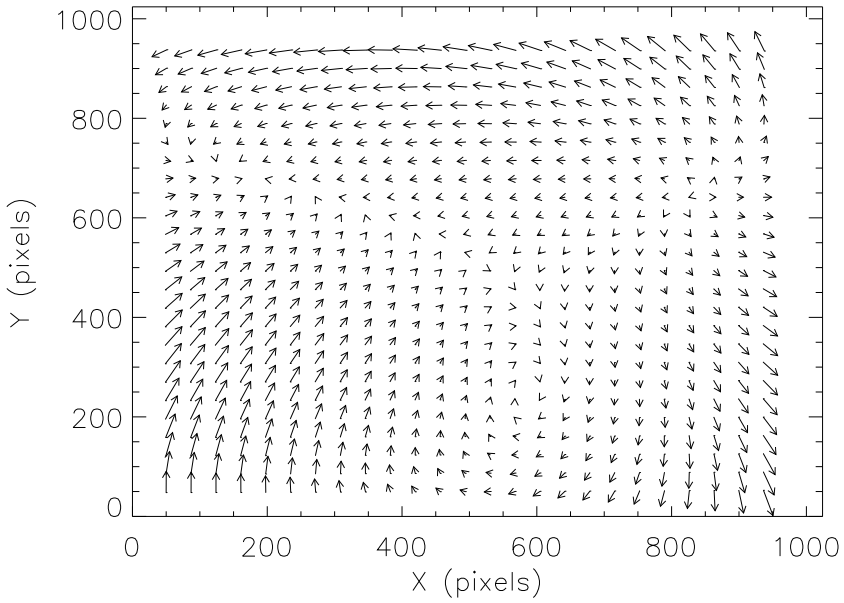

Figure A.12 Distortion measured in the narrow camera as measured in this work. See Figure A.13 for the magnitude of the arrows.

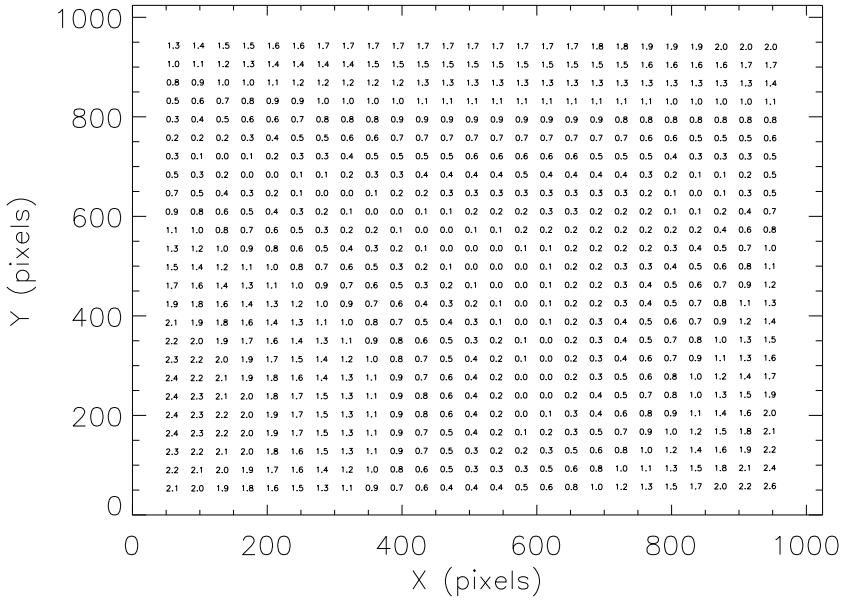

Figure A.13 Amplitude in pixels of the distortion in the narrow camera from the current data.

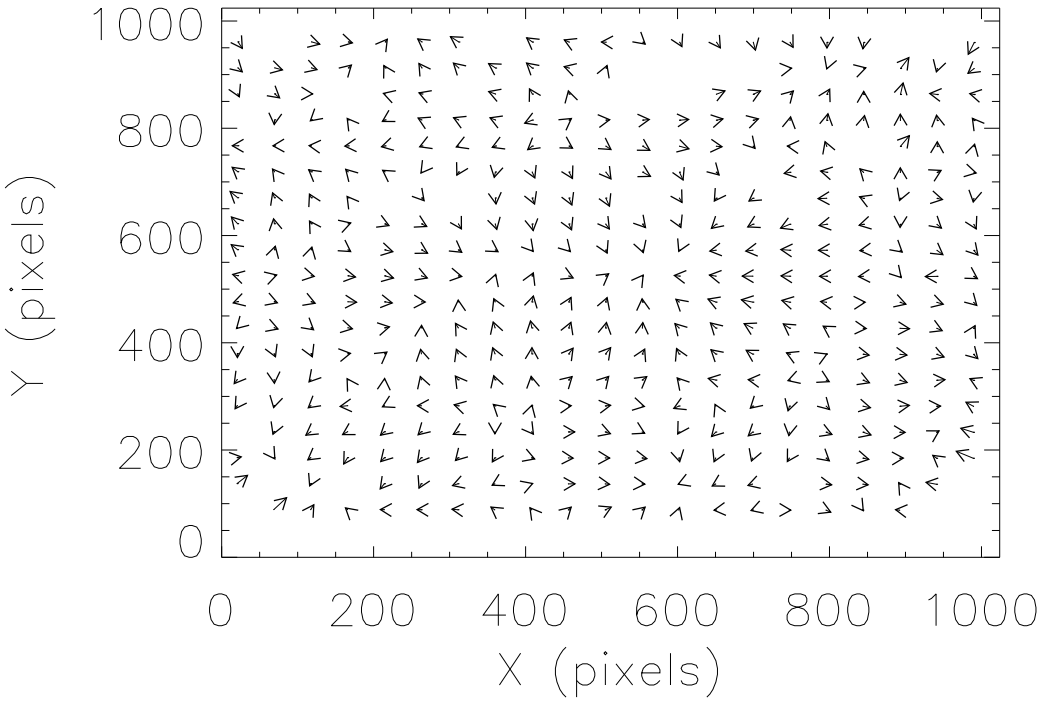

Figure A.14 Measured residuals after application of the new narrow camera distortion solution. Residuals are multiplied by a factor of 100. The residuals are < 0.1 pixels and show some evidence for higher order trends. See Figure A.15 for further information.

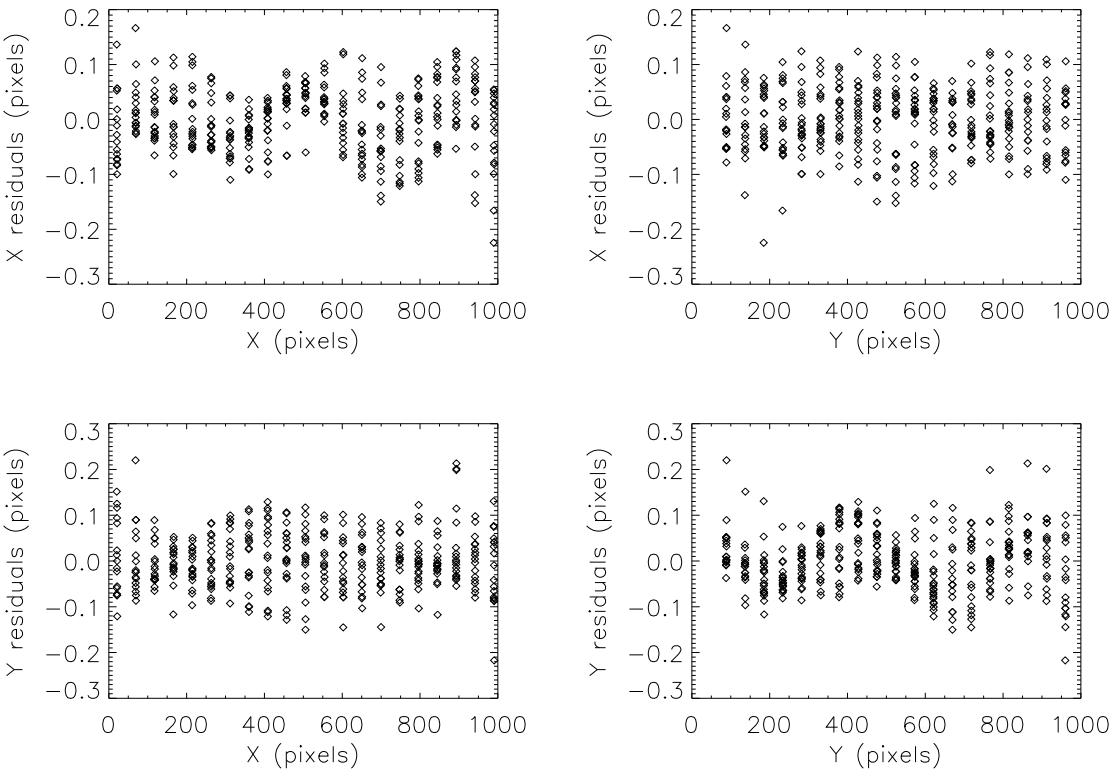

Figure A.15 Narrow camera residuals as a function of chip position. The RMS of the remaining residuals is $(\sigma_x, \sigma_y) = (0.0599, 0.0639)$ pixels. Includes all rows and columns.

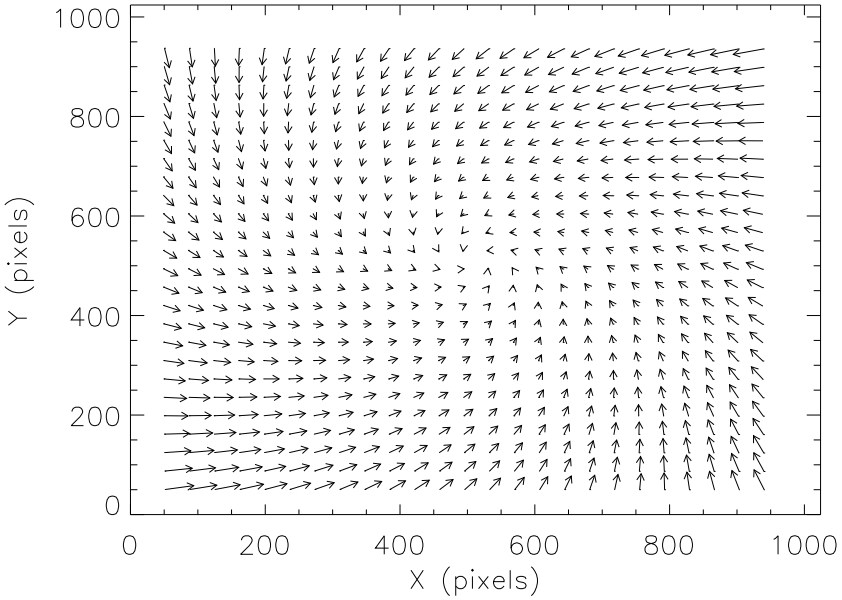

Figure A.16 Comparison of the preship and new wide camera distortion solutions. There appears to be an overall rotation of the two solutions with respect to each other. This is likely due to an incorrect procedure in determining the preship distortion solution (see text for details).

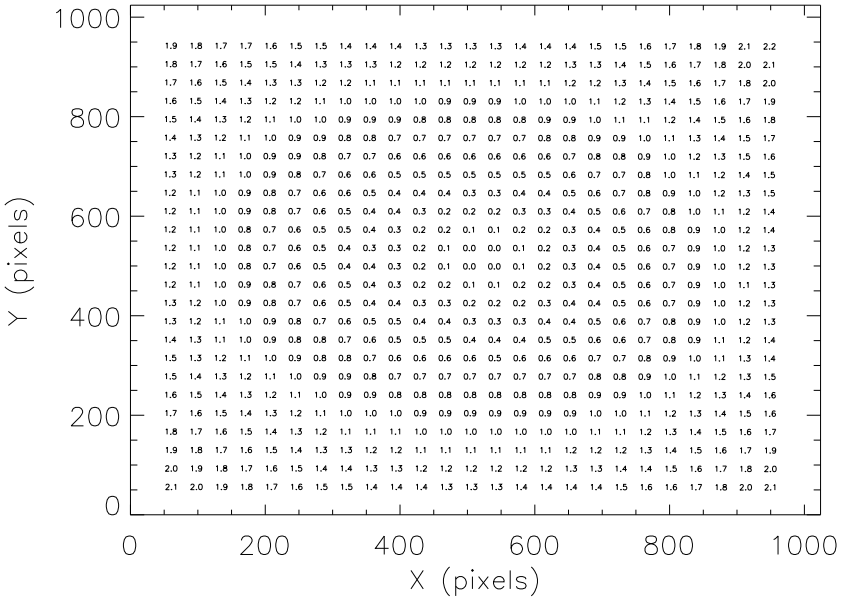

Figure A.17 Amplitude of the arrows in Figure A.16.

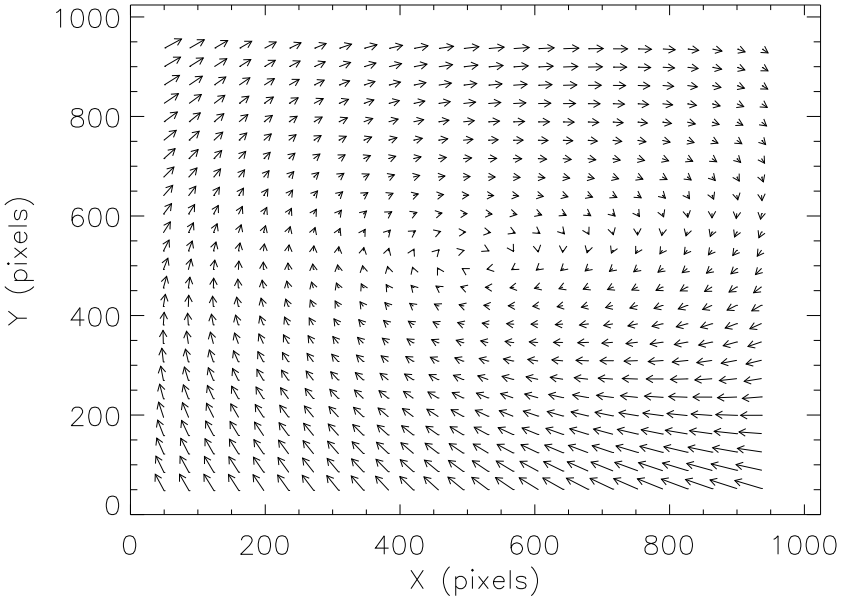

Figure A.18 Comparison of the preship and new narrow camera distortion solutions. There appears to be an overall rotation of the two solutions with respect to each other. This is likely due to an incorrect procedure in determining the preship distortion solution (see text for details).

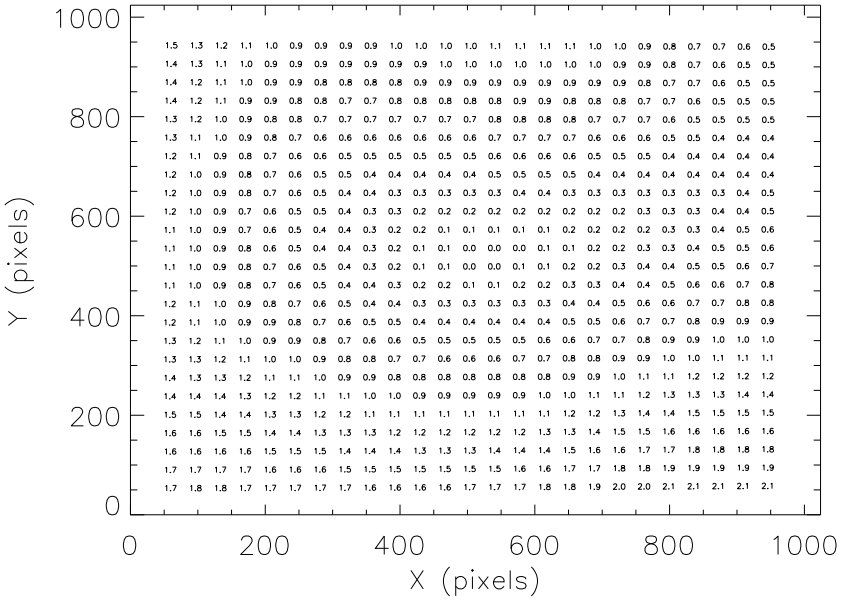

Figure A.19 Amplitude of the arrows in Figure A.18.

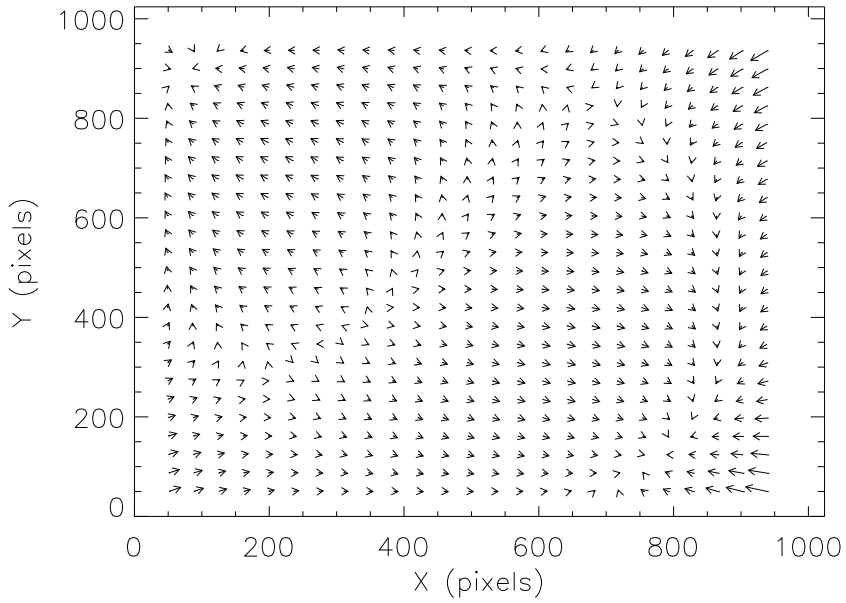

Figure A.20 Comparison of the preship and new wide camera distortion solutions after correcting for an overall shift scale and rotation. There are some small differences between the two solutions.

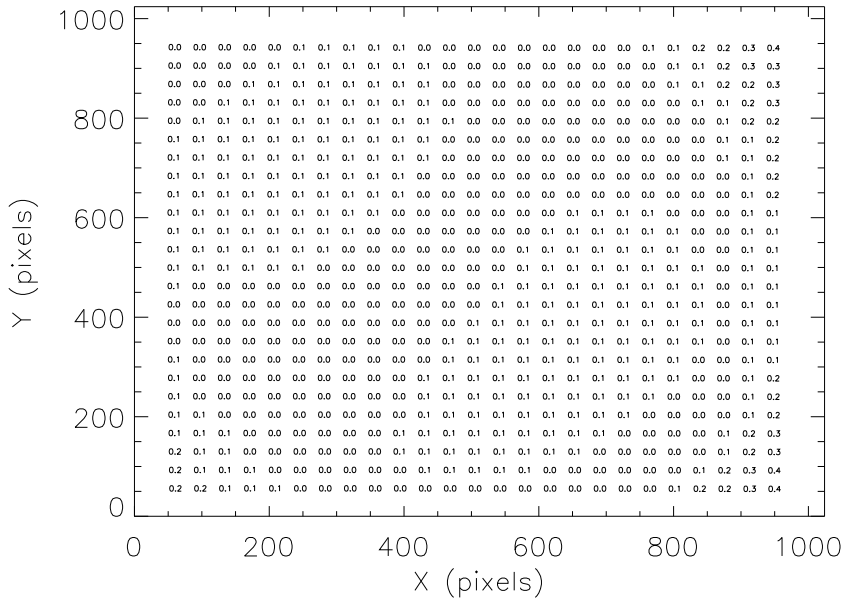

Figure A.21 Amplitude of the arrows in Figure A.20.

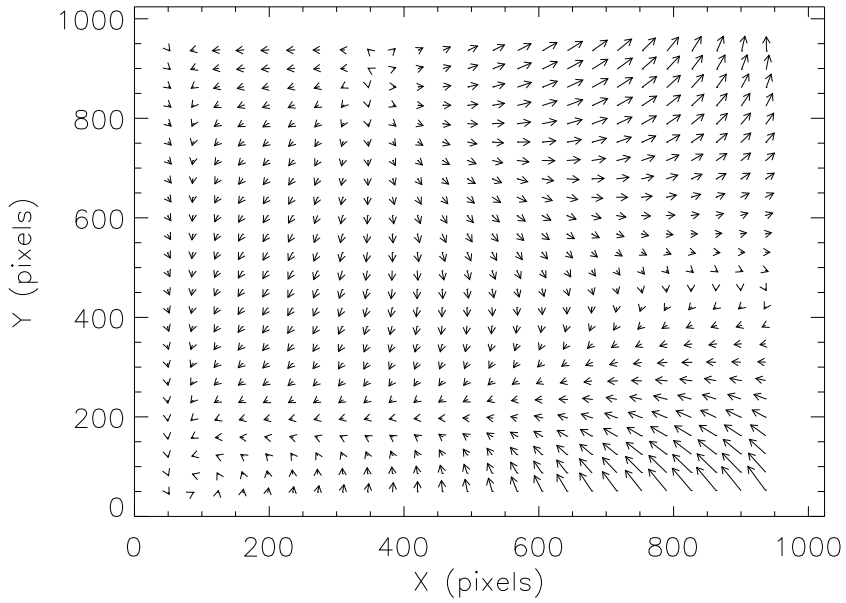

Figure A.22 Comparison of the preship and new narrow camera distortion solutions after correcting for an overall shift scale and rotation. There are some small differences between the two solutions.

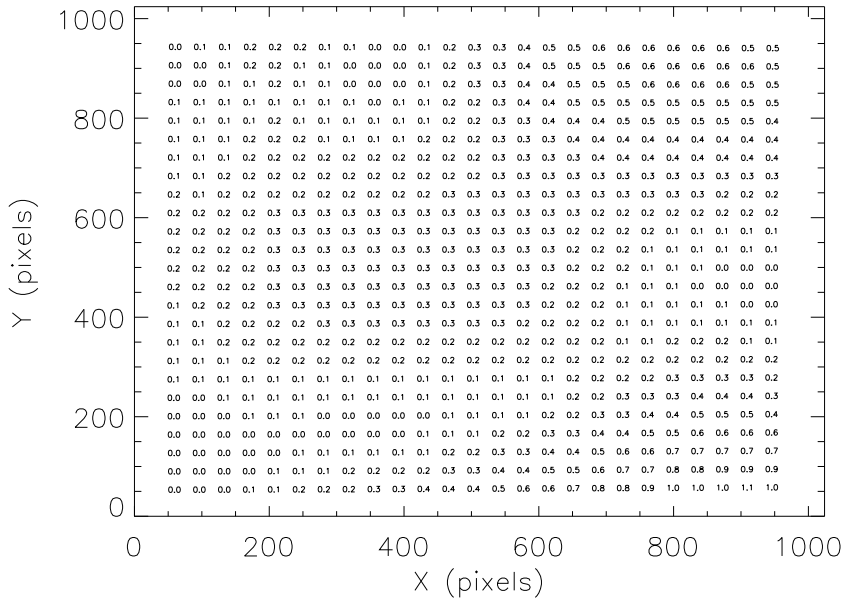

Figure A.23 Amplitude of the arrows in Figure A.22.

Bibliography

Alpar, M. A., Cheng, A. F., Ruderman, M. A., & Shaham, J. 1982, Nature, 300, 728

Anderson, J., Bedin, L. R., Piotto, G., Yadav, R. S., & Bellini, A. 2006, A&A, 454, 1029

Anderson, J. & King, I. R. 2000, PASP, 112, 1360

—. 2003a, PASP, 115, 113

—. 2003b, AJ, 126, 772

Arons, J. 1981, ApJ, 248, 1099

Arzoumanian, Z., Cordes, J., Van Buren, D., Corcoran, M., Safi-Harb, S., & Petre, R. 2004, AAS/High Energy Astrophysics Division, 8,

Bally, J., Pound, M. W., Stark, A. A., Israel, F., Hirano, N., Kameya, O., Sunada, K., Hayashi, M., Thronson, H. J., & Hereld, M. 1989, ApJ, 338, L65

Bassa, C., Pooley, D., Homer, L., Verbunt, F., Gaensler, B. M., Lewin, W. H. G., Anderson, S. F., Margon, B., Kaspi, V. M., & van der Klis, M. 2004, ApJ, 609, 755

Becker, R. H. & Fesen, R. A. 1988, ApJ, 334, L35

Becker, W. & Aschenbach, B. 2002, in Neutron Stars, Pulsars, and Supernova Remnants, ed. W. Becker, H. Lesch, and J. Trmper (MPE Rep. 278; Carching: MPE), 64

Becker, W., Swartz, D. A., Pavlov, G. G., Elsner, R. F., Grindlay, J., Mignani, R., Tennant, A. F., Backer, D., Pulone, L., Testa, V., & Weisskopf, M. C. 2003, ApJ, 594, 798

Becker, W. & Trümper, J. 1999a, A&A, 341, 803

—. 1999b, A&A, 341, 803

Benedict, G. F., McArthur, B. E., Fredrick, L. W., Harrison, T. E., Skrutskie, M. F., Slesnick, C. L., Rhee, J., Patterson, R. J., Nelan, E., Jefferys, W. H., van Altena, W., Montemayor, T., Shelus, P. J., Franz, O. G., Wasserman, L. H., Hemenway, P. D., Duncombe, R. L., Story, D., Whipple, A. L., & Bradley, A. J. 2003, AJ, 126, 2549

Berghoefer, T. W., Schmitt, J. H. M. M., Danner, R., & Cassinelli, J. P. 1997, A&A, 322, 167

Bessell, M. S. & Brett, J. M. 1988, PASP, 100, 1134

Betts, J. T. 1980, ACM Transactions on Mathematical Software (ACM New York, NY —c1980, Vol 6, Issue 3)

Bibby, J. L., Crowther, P. A., Furness, J. P., & Clark, J. S. 2008, MNRAS, 386, L23

Boden, A. F., Torres, G., Sargent, A. I., Akeson, R. L., Carpenter, J. M., Boboltz, D. A., Massi, M., Ghez, A. M., Latham, D. W., Johnston, K. J., Menten, K. M., & Ros, E. 2007, arXiv/0706.2376

Bogdanov, S., Grindlay, J. E., Heinke, C. O., Camilo, F., Freire, P. C. C., & Becker, W. 2006, ApJ, 646, 1104

Bogdanov, S., Grindlay, J. E., & van den Berg, M. 2005, ApJ, 630, 1029

Boggs, S., Hurley, K., Smith, D. M., Lin, R. P., Hurford, G., Hajdas, W., & Wigger, C. 2005, GRB Circular Network, 2936

Borkowski, J., Gotz, D., Mereghetti, S., Mowlavi, N., Shaw, S., & Turler, M. 2004, GRB Circular Network, 2920

Britton, M. C. 2006, PASP, 118, 885

Buccheri, R., Bennett, K., Bignami, G. F., Bloemen, J. B. G. M., Boriakoff, V., Caraveo, P. A., Hermsen, W., Kanbach, G., Manchester, R. N., Masnou, J. L.,

Mayer-Hasselwander, H. A., Ozel, M. E., Paul, J. A., Sacco, B., Scarsi, L., & Strong, A. W. 1983, A&A, 128, 245

Burrows, A., Dessart, L., Ott, C. D., & Livne, E. 2007a, Phys. Rep., 442, 23

Burrows, A., Livne, E., Dessart, L., Ott, C. D., & Murphy, J. 2007b, ApJ, 655, 416

Cameron, P. B., Chandra, P., Ray, A., Kulkarni, S. R., Frail, D. A., Wieringa, M. H., Nakar, E., Phinney, E. S., Miyazaki, A., Tsuboi, M., Okumura, S., Kawai, N., Menten, K. M., & Bertoldi, F. 2005, Nature, 434, 1112

Cameron, P. B. & Kulkarni, S. R. 2005, GRB Circular Network, 2928

Camilo, F., Lorimer, D. R., Freire, P., Lyne, A. G., & Manchester, R. N. 2000, ApJ, 535, 975

Camilo, F., Ransom, S. M., Halpern, J. P., Reynolds, J., Helfand, D. J., Zimmerman, N., & Sarkissian, J. 2006, Nature, 442, 892

Campana, S., Stella, L., Israel, G. L., Moretti, A., Parmar, A. N., & Orlandini, M. 2002, ApJ, 580, 389

Cash, W. 1979, ApJ, 228, 939

Cheng, K. S. & Taam, R. E. 2003, ApJ, 598, 1207

Cheng, K. S. & Wang, X. Y. 2003, ApJ, 593, L85

Colavita, M. M. & Wizinowich, P. L. 2003, in Presented at the Society of Photo-Optical Instrumentation Engineers (SPIE) Conference, Vol. 4838, Interferometry for Optical Astronomy II. Edited by Wesley A. Traub. Proceedings of the SPIE, Volume 4838, pp. 79-88 (2003)., ed. W. A. Traub, 79–88

Corbel, S. & Eikenberry, S. S. 2004, å, 419, 191

Corbel, S., Wallyn, P., Dame, T. M., Durouchoux, P., Mahoney, W. A., Vilhu, O., & Grindlay, J. E. 1997, ApJ, 478, 624

Cordes, J. M. & Lazio, T. J. W. 2002, preprint (astro-ph/0207156)

Cutri, R. M., Skrutskie, M. F., van Dyk, S., Beichman, C. A., Carpenter, J. M., Chester, T., Cambresy, L., Evans, T., Fowler, J., Gizis, J., Howard, E., Huchra, J., Jarrett, T., Kopan, E. L., Kirkpatrick, J. D., Light, R. M., Marsh, K. A., McCallon, H., Schneider, S., Stiening, R., Sykes, M., Weinberg, M., Wheaton, W. A., Wheelock, S., & Zacarias, N. 2003a, 2MASS All Sky Catalog of point sources. (The IRSA 2MASS All-Sky Point Source Catalog, NASA/IPAC Infrared Science Archive. http://irsa.ipac.caltech.edu/applications/Gator/)

—. 2003b, 2MASS All Sky Catalog of point sources. (The IRSA 2MASS All-Sky Point Source Catalog, NASA/IPAC Infrared Science Archive. http://irsa.ipac.caltech.edu/applications/Gator/)

D'Amico, N., Possenti, A., Fici, L., Manchester, R. N., Lyne, A. G., Camilo, F., & Sarkissian, J. 2002, ApJ, 570, L89

D'Amico, N., Possenti, A., Manchester, R. N., Sarkissian, J., Lyne, A. G., & Camilo, F. 2001, ApJ, 561, L89

de Jager, O. C., Raubenheimer, B. C., & Swanepoel, J. W. H. 1989, A&A, 221, 180

de Muizon, M., Strom, R. G., Oort, M. J. A., Claas, J. J., & Braun, R. 1988, A&A, 193, 248

Dehnen, W. & Binney, J. J. 1998, MNRAS, 298, 387

Dessart, L., Burrows, A., Livne, E., & Ott, C. D. 2006, ApJ, 645, 534

Dickey, J. M. & Lockman, F. J. 1990, ARA&A, 28, 215

Diolaiti, E., Bendinelli, O., Bonaccini, D., Close, L. M., Currie, D. G., & Parmeggiani, G. 2000, in Presented at the Society of Photo-Optical Instrumentation Engineers (SPIE) Conference, Vol. 4007, Proc. SPIE Vol. 4007, p. 879-888, Adaptive Optical Systems Technology, Peter L. Wizinowich; Ed., ed. P. L. Wizinowich, 879–888

Duncan, R. C. 2000, in American Institute of Physics Conference Series, Vol. 526, Gamma-ray Bursts, 5th Huntsville Symposium, ed. R. M. Kippen, R. S. Mallozzi, & G. J. Fishman, 830–841

Duncan, R. C. & Thompson, C. 1992, ApJ, 392, L9

Durant, M. 2005, ApJ, 632, 563

Durant, M. & van Kerkwijk, M. H. 2006, ApJ, 650, 1070

Edmonds, P. D., Gilliland, R. L., Camilo, F., Heinke, C. O., & Grindlay, J. E. 2002, ApJ, 579, 741

Eikenberry, S. S., Matthews, K., LaVine, J. L., Garske, M. A., Hu, D., Jackson, M. A., Patel, S. G., Barry, D. J., Colonno, M. R., Houck, J. R., Wilson, J. C., Corbel, S., & Smith, J. D. 2004, ApJ, 616, 506

Fahlman, G. G. & Gregory, P. C. 1981, Nature, 293, 202

Feroci, M., Hurley, K., Duncan, R. C., & Thompson, C. 2001, ApJ, 549, 1021

Ferrario, L. & Wickramasinghe, D. 2006, MNRAS, 367, 1323

Figer, D. F., Najarro, F., & Kudritzki, R. P. 2004, ApJ, 610, L109

Frail, D. A., Kulkarni, S. R., & Bloom, J. S. 1999, Nature, 398, 127

Frail, D. A., Waxman, E., & Kulkarni, S. R. 2000, ApJ, 537, 191

Freire, P. C., Camilo, F., Kramer, M., Lorimer, D. R., Lyne, A. G., Manchester, R. N., & D'Amico, N. 2003, MNRAS, 340, 1359

Freire, P. C., Camilo, F., Lorimer, D. R., Lyne, A. G., Manchester, R. N., & D'Amico, N. 2001, MNRAS, 326, 901

Fuchs, Y., Mirabel, F., Chaty, S., Claret, A., Cesarsky, C. J., & Cesarsky, D. A. 1999, å, 350, 891

Gaensler, B. M., Kouveliotou, C., Gelfand, J. D., Taylor, G. B., Eichler, D., Wijers, R. A. M. J., Granot, J., Ramirez-Ruiz, E., Lyubarsky, Y. E., Hunstead, R. W., Campbell-Wilson, D., van der Horst, A. J., McLaughlin, M. A., Fender, R. P., Garrett, M. A., Newton-McGee, K. J., Palmer, D. M., Gehrels, N., & Woods, P. M. 2005a, Nature, 434, 1104

Gaensler, B. M., Kouveliotou, C., Wijers, R., Garrett, M., Finger, M., Woods, P., Patel, S., McLaughlin, M., Fender, R., & Delaney, T. 2005b, GRB Circular Network, 2933

Gaensler, B. M., McClure-Griffiths, N. M., Oey, M. S., Haverkorn, M., Dickey, J. M., & Green, A. J. 2005c, ApJ, 620, L95

Gaensler, B. M., Slane, P. O., Gotthelf, E. V., & Vasisht, G. 2001, ApJ, 559, 963

Garwood, R. W. & Dickey, J. M. 1989, ApJ, 338, 841

Gavriil, F. P., Dib, R., Kaspi, V. M., & Woods, P. M. 2007, The Astronomer's Telegram, 993, 1

Glindemann, A., Abuter, R., Carbognani, F., Delplancke, F., Derie, F., Gennai, A., Gitton, P. B., Kervella, P., Koehler, B., Leveque, S. A., Menardi, S., Michel, A., Paresce, F., Duc, T. P., Richichi, A., Schoeller, M., Tarenghi, M., Wallander, A., & Wilhelm, R. 2000, in Presented at the Society of Photo-Optical Instrumentation Engineers (SPIE) Conference, Vol. 4006, Proc. SPIE Vol. 4006, p. 2-12, Interferometry in Optical Astronomy, Pierre J. Lena; Andreas Quirrenbach; Eds., ed. P. J. Lena & A. Quirrenbach, 2–12

Goad, M. R., Page, K. L., Godet, O., O'Brien, P. T., Vaughan, S., & Hurley, K. 2006, GRB Coordinates Network, 5438, 1

Gotthelf, E. V. & Vasisht, G. 1997, ApJ, 486, L133+

Gratton, R. G., Bragaglia, A., Carretta, E., Clementini, G., Desidera, S., Grundahl, F., & Lucatello, S. 2003, A&A, 408, 529

Green, D. A. 1986, MNRAS, 219, 39P

—. 1989, MNRAS, 238, 737

Greenwood, D. P. 1977, Journal of the Optical Society of America (1917-1983), 67, 390

Grindlay, J. E., Camilo, F., Heinke, C. O., Edmonds, P. D., Cohn, H., & Lugger, P. 2002, ApJ, 581, 470

Grindlay, J. E., Heinke, C., Edmonds, P. D., & Murray, S. S. 2001, Science, 292, 2290

Grindlay, J. E., Hong, J., Zhao, P., Laycock, S., van den Berg, M., Koenig, X., Schlegel, E. M., Cohn, H. N., Lugger, P. M., & Rogel, A. B. 2005, ApJ, 635, 920

Gubler, J. & Tytler, D. 1998, PASP, 110, 738

Güdel, M. 2004, A&A Rev., 12, 71

Harding, A. K. & Muslimov, A. G. 2001, ApJ, 556, 987

—. 2002, ApJ, 568, 862

Harris, W. E. 1996, AJ, 112, 1487

Hartmann, D. & Burton, W. B. 1997, Atlas of galactic neutral hydrogen (Cambridge; New York: Cambridge University Press)

Hayward, T. L., Brandl, B., Pirger, B., Blacken, C., Gull, G. E., Schoenwald, J., & Houck, J. R. 2001, PASP, 113, 105

Heinke, C. O., Grindlay, J. E., Edmonds, P. D., Cohn, H. N., Lugger, P. M., Camilo, F., Bogdanov, S., & Freire, P. C. 2005, ApJ, 625, 796

Helfand, D. J., Chatterjee, S., Brisken, W. F., Camilo, F., Reynolds, J., van Kerkwijk, M. H., Halpern, J. P., & Ransom, S. M. 2007, ArXiv Astrophysics e-prints

Helfand, D. J. & Long, K. S. 1979, Nature, 282, 589

Hjellming, R. M., Rupen, M. P., Hunstead, R. W., Campbell-Wilson, D., Mioduszewski, A. J., Gaensler, B. M., Smith, D. A., Sault, R. J., Fender, R. P., Spencer, R. E., de la Force, C. J., Richards, A. M. S., Garrington, S. T., Trushkin, S. A., Ghigo, F. D., Waltman, E. B., & McCollough, M. 2000, ApJ, 544, 977

Hobbs, G., Lorimer, D. R., Lyne, A. G., & Kramer, M. 2005, MNRAS, 360, 974

Hong, J., van den Berg, M., Schlegel, E. M., Grindlay, J. E., Koenig, X., Laycock, S., & Zhao, P. 2005, ApJ, 635, 907

Houck, J. C. & Denicola, L. A. 2000, in ASP Conf. Ser. 216: Astronomical Data Analysis Software and Systems IX, ed. N. Manset, C. Veillet, & D. Crabtree, 591

Hulleman, F., Tennant, A. F., van Kerkwijk, M. H., Kulkarni, S. R., Kouveliotou, C., & Patel, S. K. 2001, ApJ, 563, L49

Hulleman, F., van Kerkwijk, M. H., & Kulkarni, S. R. 2000, Nature, 408, 689

Hurley, K., Boggs, S. E., Smith, D. M., Duncan, R. C., Lin, R., Zoglauer, A., Krucker, S., Hurford, G., Hudson, H., Wigger, C., Hajdas, W., Thompson, C., Mitrofanov, I., Sanin, A., Boynton, W., Fellows, C., von Kienlin, A., Lichti, G., Rau, A., & Cline, T. 2005, Nature, 434, 1098

Hurley, K., Cline, T., Mazets, E., Barthelmy, S., Butterworth, P., Marshall, F., Palmer, D., Aptekar, R., Golenetskii, S., Il'Inskii, V., Frederiks, D., McTiernan, J., Gold, R., & Trombka, J. 1999a, Nature, 397, 41

Hurley, K., Li, P., Kouveliotou, C., Murakami, T., Ando, M., Strohmayer, T., van Paradijs, J., Vrba, F., Luginbuhl, C., Yoshida, A., & Smith, I. 1999b, ApJ, 510, L111

Israel, G., Covino, S., Mignani, R., Stella, L., Marconi, G., Testa, V., Mereghetti, S., Campana, S., Rea, N., Götz, D., Perna, R., & Lo Curto, G. 2005, A&A, 438, L1

Israel, G. L., Mereghetti, S., & Stella, L. 1994, ApJ, 433, L25

Israel, G. L., Romano, P., Mangano, V., Dall'Osso, S., Chincarini, G., Stella, L., Campana, S., Belloni, T., Tagliaferri, G., Blustin, A. J., Sakamoto, T., Hurley, K., Zane, S., Moretti, A., Palmer, D., Guidorzi, C., Burrows, D. N., Gehrels, N., & Krimm, H. A. 2008, ArXiv e-prints, 805

Kaplan, D. L., Fox, D. W., Kulkarni, S. R., Gotthelf, E. V., Vasisht, G., & Frail, D. A. 2002a, ApJ, 564, 935

—. 2002b, ApJ, 564, 935

Kaspi, V., Dib, R., & Gavriil, F. 2006, The Astronomer's Telegram, 794, 1

Kaspi, V. M., Gavriil, F. P., Woods, P. M., Jensen, J. B., Roberts, M. S. E., & Chakrabarty, D. 2003, ApJ, 588, L93

Kern, B. & Martin, C. 2002, Nature, 417, 527

Kolpak, M. A., Jackson, J. M., Bania, T. M., & Dickey, J. M. 2002, ApJ, 578, 868

Kornilov, V., Tokovinin, A., Shatsky, N., Voziakova, O., Potanin, S., & Safonov, B. 2007, arXiv/0709.2081

Kothes, R., Uyaniker, B., & Yar, A. 2002, ApJ, 576, 169

Kouveliotou, C., Fishman, G. J., Meegan, C. A., Paciesas, W. S., Wilson, R. B., van Paradijs, J., Preece, R. D., Briggs, M. S., Pendleton, G. N., & Brock, M. N. 1993, Nature, 362, 728

Kulkarni, S. R. & Frail, D. A. 1993, Nature, 365, 33

Kulkarni, S. R., Matthews, K., Neugebauer, G., Reid, I. N., van Kerkwijk, M. H., & Vasisht, G. 1995, ApJ, 440, L61

Kulkarni, S. R., Vogel, S. N., Wang, Z., & Wood, D. O. S. 1992, Nature, 360, 139

Lane, B. F., Colavita, M. M., Boden, A. F., & Lawson, P. R. 2000, in Presented at the Society of Photo-Optical Instrumentation Engineers (SPIE) Conference, Vol. 4006,

Proc. SPIE Vol. 4006, p. 452-458, Interferometry in Optical Astronomy, Pierre J. Lena; Andreas Quirrenbach; Eds., ed. P. J. Lena & A. Quirrenbach, 452–458

Lange, C., Camilo, F., Wex, N., Kramer, M., Backer, D. C., Lyne, A. G., & Doroshenko, O. 2001, MNRAS, 326, 274

Lazorenko, P. F. 2006, A&A, 449, 1271

Lazorenko, P. F., Mayor, M., Dominik, M., Pepe, F., Segransan, D., & Udry, S. 2007, A&A, 471, 1057

Lindegren, L. 1978, in IAU Colloq. 48: Modern Astrometry, ed. F. V. Prochazka & R. H. Tucker, 197–217

Lommen, A. N., Zepka, A., Backer, D. C., McLaughlin, M., Cordes, J. M., Arzoumanian, Z., & Xilouris, K. 2000, ApJ, 545, 1007

Lorimer, D. R. & Xilouris, K. M. 2000, ApJ, 545, 385

Mazets, E. P., Golenetskij, S. V., & Guryan, Y. A. 1979, Soviet Astronomy Letters, 5, 343

McClure-Griffiths, N. M. & Gaensler, B. M. 2005, ApJ, 630, L161

Mereghetti, S. 2008, ArXiv e-prints, 804

Metchev, S. A. 2006, PhD thesis, California Institute of Technology, United States – California

Minkowski, R. 1948, PASP, 60, 386

Monet, D. G., Dahn, C. C., Vrba, F. J., Harris, H. C., Pier, J. R., Luginbuhl, C. B., & Ables, H. D. 1992, AJ, 103, 638

Muno, M. P., Clark, J. S., Crowther, P. A., Dougherty, S. M., de Grijs, R., Law, C., McMillan, S. L. W., Morris, M. R., Negueruela, I., Pooley, D., Portegies Zwart, S., & Yusef-Zadeh, F. 2006, ApJ, 636, L41

Murakami, T., Tanaka, Y., Kulkarni, S. R., Ogasaka, Y., Sonobe, T., Ogawara, Y., Aoki, T., & Yoshida, A. 1994, Nature, 368, 127

Murray, S. S., Chappell, J. H., Kenter, A. T., Kraft, R. P., Meehan, G. R., & Zombeck, M. V. 1998, in Proc. SPIE Vol. 3356, Space Telescopes and Instruments V, Pierre Y. Bely; James B. Breckinridge; Eds., 974

Muterspaugh, M. W., Lane, B. F., Konacki, M., Burke, B. F., Colavita, M. M., Kulkarni, S. R., & Shao, M. 2006, A&A, 446, 723

Nakajima, T., Iwamuro, F., Maihara, T., Motohara, K., Terada, H., Goto, M., Iwai, J., Tanabe, H., Taguchi, T., Hata, R., Yanagisawa, K., Iye, M., Kashikawa, N., & Tamura, M. 2000, AJ, 120, 2488

Nakar, E., Piran, T., & Sari, R. 2005, astro-ph/0502052

Navarro, J., de Bruyn, A. G., Frail, D. A., Kulkarni, S. R., & Lyne, A. G. 1995, ApJ, 455, L55+

Nicastro, L., Cusumano, G., Löhmer, O., Kramer, M., Kuiper, L., Hermsen, W., Mineo, T., & Becker, W. 2004, A&A, 413, 1065

Nice, D. J., Splaver, E. M., Stairs, I. H., Löhmer, O., Jessner, A., Kramer, M., & Cordes, J. M. 2005, ApJ, 634, 1242

Onello, J. S., Depree, C. G., Phillips, J. A., & Goss, W. M. 1995, ApJ, 449, L127+

Pacholczyk, A. G. 1970, Radio astrophysics. Nonthermal processes in galactic and extragalactic sources (Series of Books in Astronomy and Astrophysics, San Francisco: Freeman, 1970)

Paczynski, B. 1992, Acta Astronomica, 42, 145

Perryman, M. A. C., de Boer, K. S., Gilmore, G., Høg, E., Lattanzi, M. G., Lindegren, L., Luri, X., Mignard, F., Pace, O., & de Zeeuw, P. T. 2001, A&A, 369, 339

Perryman, M. A. C., Lindegren, L., Kovalevsky, J., Hoeg, E., Bastian, U., Bernacca, P. L., Crézé, M., Donati, F., Grenon, M., van Leeuwen, F., van der Marel, H., Mignard, F., Murray, C. A., Le Poole, R. S., Schrijver, H., Turon, C., Arenou, F., Froeschlé, M., & Petersen, C. S. 1997, A&A, 323, L49

Phillips, J. A., Onello, J. S., & Kulkarni, S. R. 1993, ApJ, 415, L143+

Pravdo, S. H. & Shaklan, S. B. 1996, ApJ, 465, 264

Pravdo, S. H., Shaklan, S. B., Henry, T., & Benedict, G. F. 2004, ApJ, 617, 1323

Predehl, P. & Schmitt, J. H. M. M. 1995, A&A, 293, 889

Press, W. H., Teukolsky, S. A., Vetterling, W. T., & Flannery, B. P. 1992, Numerical recipes in C. The art of scientific computing (Cambridge: University Press, —c1992, 2nd ed.)

Pryor, C. & Meylan, G. 1993, in Astronomical Society of the Pacific Conference Series, Vol. 50, Structure and Dynamics of Globular Clusters, ed. S. G. Djorgovski & G. Meylan, 357–+

Ransom, S. M., Stairs, I. H., Backer, D. C., Greenhill, L. J., Bassa, C. G., Hessels, J. W. T., & Kaspi, V. M. 2004, ApJ, 604, 328

Rea, N., Tiengo, A., Mereghetti, S., Israel, G. L., Zane, S., Turolla, R., & Stella, L. 2005, ApJ, 627, L133

Reich, W., Fürst, E., Altenhoff, W. J., Reich, P., & Junkes, N. 1985, A&A, 151, L10

Rho, J. & Petre, R. 1997, ApJ, 484, 828

Rutledge, R. E., Bildsten, L., Brown, E. F., Chakrabarty, D., Pavlov, G. G., & Zavlin, V. E. 2007, ApJ, 658, 514

Rutledge, R. E., Fox, D. W., Kulkarni, S. R., Jacoby, B. A., Cognard, I., Backer, D. C., & Murray, S. S. 2004, ApJ, 613, 522

Sanbonmatsu, K. Y. & Helfand, D. J. 1992, AJ, 104, 2189

Sandquist, E. L. & Bolte, M. 2004, ApJ, 611, 323

Sasiela, R. J. 1994, Electromagnetic wave propagation in turbulence. Evaluation and application of Mellin transforms (Springer Series on Wave Phenomena, Berlin: Springer, —c1994)

Scargle, J. D. 1998, ApJ, 504, 405

Scott, M. A. & Readhead, A. C. S. 1977, MNRAS, 180, 539

Stetson, P. B. 1987, PASP, 99, 191

Swanepoel, J. W. H., de Beer, C. F., & Loots, H. 1996, ApJ, 467, 261

Tam, C. R., Kaspi, V. M., van Kerkwijk, M. H., & Durant, M. 2004, ApJ, 617, L53

Tennant, A. F., Becker, W., Juda, M., Elsner, R. F., Kolodziejczak, J. J., Murray, S. S., O'Dell, S. L., Paerels, F., Swartz, D. A., Shibazaki, N., & Weisskopf, M. C. 2001, ApJ, 554, L173

Testa, V., Rea, N., Mignani, R. P., Israel, G. L., Perna, R., Chaty, S., Stella, L., Covino, S., Turolla, R., Zane, S., Lo Curto, G., Campana, S., Marconi, G., & Mereghetti, S. 2008, A&A, 482, 607

Thompson, C. & Duncan, R. C. 1993, ApJ, 408, 194

Thomsen, M., Britton, M., & Pickles, A. 2007, in American Astronomical Society Meeting Abstracts, Vol. 210, American Astronomical Society Meeting Abstracts, 117.01–+

Thorsett, S. E., Arzoumanian, Z., Camilo, F., & Lyne, A. G. 1999, ApJ, 523, 763

Toscano, M., Sandhu, J. S., Bailes, M., Manchester, R. N., Britton, M. C., Kulkarni, S. R., Anderson, S. B., & Stappers, B. W. 1999, MNRAS, 307, 925

Troy, M., Dekany, R. G., Brack, G., Oppenheimer, B. R., Bloemhof, E. E., Trinh, T., Dekens, F. G., Shi, F., Hayward, T. L., & Brandl, B. 2000, in Presented at the Society of Photo-Optical Instrumentation Engineers (SPIE) Conference, Vol. 4007, Proc. SPIE Vol. 4007, p. 31-40, Adaptive Optical Systems Technology, Peter L. Wizinowich; Ed., ed. P. L. Wizinowich, 31–40

Unwin, S. C., Shao, M., Tanner, A. M., Allen, R. J., Beichman, C. A., Boboltz, D., Catanzarite, J. H., Chaboyer, B. C., Ciardi, D. R., Edberg, S. J., Fey, A. L., Fischer, D. A., Gelino, C. R., Gould, A. P., Grillmair, C., Henry, T. J., Johnston, K. V., Johnston, K. J., Jones, D. L., Kulkarni, S. R., Law, N. M., Majewski, S. R., Makarov, V. V., Marcy, G. W., Meier, D. L., Olling, R. P., Pan, X., Patterson, R. J., Pitesky, J. E., Quirrenbach, A., Shaklan, S. B., Shaya, E. J., Strigari, L. E., Tomsick, J. A., Wehrle, A. E., & Worthey, G. 2007, arXiv:0708.3953

van Dam, M. A., Bouchez, A. H., Le Mignant, D., Johansson, E. M., Wizinowich, P. L., Campbell, R. D., Chin, J. C. Y., Hartman, S. K., Lafon, R. E., Stomski, Jr., P. J., & Summers, D. M. 2006, PASP, 118, 310

van Kerkwijk, M. H., Kulkarni, S. R., Matthews, K., & Neugebauer, G. 1995, ApJ, 444, L33

Vasisht, G. & Gotthelf, E. V. 1997, ApJ, 486, L129+

Vasisht, G., Kulkarni, S. R., Frail, D. A., & Greiner, J. 1994, ApJ, 431, L35

Vrba, F. J., Henden, A. A., Luginbuhl, C. B., Guetter, H. H., Hartmann, D. H., & Klose, S. 2000, ApJ, 533, L17

Wachter, S., Patel, S. K., Kouveliotou, C., Bouchet, P., Özel, F., Tennant, A. F., Woods, P. M., Hurley, K., Becker, W., & Slane, P. 2004, ApJ, 615, 887

Wang, X. Y., Wu, X. F., Fan, Y. Z., Dai, Z. G., & Zhang, B. 2005, astro-ph/0502085

Wang, Z., Chakrabarty, D., & Kaplan, D. L. 2006, Nature, 440, 772

Webb, N. A., Olive, J.-F., & Barret, D. 2004a, A&A, 417, 181

Webb, N. A., Olive, J.-F., Barret, D., Kramer, M., Cognard, I., & Löhmer, O. 2004b, A&A, 419, 269

Wizinowich, P. L., Le Mignant, D., Bouchez, A. H., Campbell, R. D., Chin, J. C. Y., Contos, A. R., van Dam, M. A., Hartman, S. K., Johansson, E. M., Lafon, R. E., Lewis, H., Stomski, P. J., Summers, D. M., Brown, C. G., Danforth, P. M., Max, C. E., & Pennington, D. M. 2006a, PASP, 118, 297

—. 2006b, PASP, 118, 297

Woods, P. M. & Thompson, C. 2004, to appear in 'Compact Stellar X-ray Sources', eds. W.H.G. Lewin and M. van der Klis; astro-ph/0406133

Woods, P. M. & Thompson, C. 2006, Soft gamma repeaters and anomalous X-ray pulsars: magnetar candidates (Compact stellar X-ray sources), 547–586

Zavlin, V. E. 2006, ApJ, 638, 951

Zavlin, V. E., Pavlov, G. G., Sanwal, D., Manchester, R. N., Trümper, J., Halpern, J. P., & Becker, W. 2002, ApJ, 569, 894

Zombeck, M. V., Chappell, J. H., Kenter, A. T., Moore, R. W., Murray, S. S., Fraser, G. W., & Serio, S. 1995, in Proc. SPIE Vol. 2518, EUV, X-Ray, and Gamma-Ray Instrumentation for Astronomy VI, Oswald H. Siegmund; John V. Vallerga; Eds., 96